

Isolated Photon Hadron Correlations in pp and p–Pb

by

Fernando T. Torales-Acosta

A dissertation submitted in partial satisfaction of the

requirements for the degree of

Doctor of Philosophy

in

Physics

in the

Graduate Division

of the

University of California, Berkeley

Committee in charge:

Barbara Jacak, Chair

Kam-Biu Luk

Lawrence Hall

Spring 2021

The dissertation of Fernando T. Torales-Acosta, titled Isolated Photon Hadron Correlations in pp and p–Pb, is approved:

Chair _____

Date _____
Date _____
Date _____

University of California, Berkeley

Isolated Photon Hadron Correlations in pp and p–Pb

Copyright 2021
by
Fernando T. Torales-Acosta

Abstract

Isolated Photon Hadron Correlations in pp and p–Pb

by

Fernando T. Torales-Acosta

Doctor of Philosophy in Physics

University of California, Berkeley

Barbara Jacak, Chair

To my loving wife and sweetheart.

May they never meet.

Contents

Contents	ii
List of Figures	v
List of Tables	ix
1 Introduction	2
1.1 QCD	2
1.2 Relativistic Heavy Ion Collisions	3
1.3 The Quark Gluon Plasma	6
1.3.1 Flow	7
1.3.2 Flow in Small Systems	11
1.3.3 Jets	13
1.3.4 Nuclear Modification Factor	14
1.4 Fragmentation Functions	17
1.5 Cold Nuclear Matter Effects	18
1.6 Two Particle Correlations	20
1.7 Prompt Photons	21
1.8 Photons in Heavy Ion Collisions	24
1.8.1 γ -Jet Correlations	25
1.8.2 γ -hadron Correlations	27
1.9 cold nuclear Matter Effects	28
1.9.1 The Nuclear Parton Distribution Function	29
1.9.2 Nuclei and Fragmentation	30
1.10 Statement of Purpose	31
2 Experimental Apparatus	32
3 Data Anaysis	33
3.1 Isolated Prompt Photons Selection	33
3.1.1 Shower Profile Selection	33
3.1.2 Photon Isolation Requirement	34

3.1.3	Underlying Event Estimation for Photon Isolation	35
3.1.4	UE Correction to Isolation Variable	37
3.1.5	Remaining Background after Photon Selection	38
3.2	Purity	40
3.2.1	The Template Fit Method	40
3.2.2	Signal Template and Background Templates	40
3.2.2.1	Fit results	44
3.3	Charged Particle Tracking	47
3.3.1	Efficiency and Fake Rate	47
3.3.2	Resolution, response matrix and bin migration	50
3.3.2.1	Angular dependence of tracking efficiency	52
3.4	Photon Hadron Correlations	53
3.4.1	Signal Correlation Function	54
3.4.2	Decay Photon Hadron Correlations	56
3.4.3	Photon Purity Weighting	57
3.4.4	Shower Signal and Background Region Correlations	57
3.4.5	Pair-Acceptance Correction with Event Mixing	57
3.4.6	Toy Monte Carlo for Validating Event Mixing	62
3.4.7	Underlying Event Estimation	63
3.4.8	Check on UE Estimation	64
3.4.9	η Assymetry in p–Pb	65
3.5	Parton Fragmentation Function	65
3.5.1	Insensitivty to parton distribution function	65
3.5.2	p–Pbto pp ratio	65
3.5.3	Integration Window	65
4	Cold Nuclear Matter Effects, EIC and LHC	66
4.0.1	Cold nuclear matter measurements at future EIC	67
4.0.2	Transverse Momentum Dependent Distributions	67
4.0.3	Probing \hat{q} at the EIC	67
4.0.4	An All-Silicon Tracker for Jet Measurements at the EIC	67
4.0.5	Charged Jet Fragmentation Function	67
4.0.6	Electron-Jet Correlations	67
5	Checks and Systematics	68
5.1	Event Mixing	68
5.1.1	Binned Event Mixing	68
5.1.2	Toy Monte Carlo Acceptance Check	68
5.1.3	Hybrid Tracking Comparison	68
5.2	Purity	68
5.2.1	Isolation and Shower shape correlation	68
5.2.2	EMCal Acceptance Variation	68

5.2.3	Purity variation (Last minute IRC check)	68
5.2.4	Check on Isolation Criterium within EMCal Acceptance	68
5.3	Tracking	68
5.3.1	Comparison to published data	68
5.3.2	Validation of φ -dependence of efficiency	69
5.3.3	Hybrid tracking on isolation check	70
5.4	Summary of Systematic Uncertainties	70
A	High Performance Computing for Event Mixing	75
A.1	Block Implementation and Parallelization	75
A.2	Hierarchical Data Format 5	75
Bibliography		76

List of Figures

1.1	The QCD coupling constant, α_S , plotted as a function of the momentum scale, Q for various measurements. The degree of perturbation theory used in the extraction of α_S is indicated in brackets next to each measurement. The bottom left shows the global average for the coupling strength at the Z boson mass, $Q = M_Z$	4
1.2	Snapshots of a central 2.76 TeV PbPb collision at different times with hadrons (blue and gray spheres) as well as quark gluon plasma (red). The red vertical lines indicate different regions of rapidity.	5
1.3	The current understanding of the expected features of the phase diagram of QCD as a function of temperature and baryon doping [annurev-nucl].	6
1.4	Lattice QCD calculations (colored bands) of the pressure p , energy density ϵ , and entropy density s of hot QCD matter in thermal equilibrium at temperature T [5, 6] show a continuous crossover around $T \approx 150$ MeV, from a hadron resonance gas (HRG; colored lines) at lower temperatures to quark-gluon plasma (QGP) at higher temperatures, at higher temperatures, a first-order phase transition is expected, as indicated in figure 1.3.	8
1.5	9
1.6	Hydrodynamic evolution of a typical head-on p+Au (top), d+Au (middle) and $^3\text{He}+\text{Au}$ (bottom) collision at $\sqrt{s_{\text{NN}}} = 200$ GeV as calculated by SONIC, where the p/d/ ^3He completely overlaps with the Au nucleus. From left to right each row gives the temperature distribution of the nuclear matter at four time points following the initial collision at $t = 0$. The arrows depict the velocity field . . .	10
1.7	v_2, v_3, v_4 , and v_5 as a function of transverse momentum for peripheral (left) and central (right) PbPb events. The full and open markers are for $\Delta\eta < 0.2$ and $\Delta\eta < 1.0$, respectively. The colored bands represent hydrodynamic models with two different parameters for the specific viscosity.	11
1.8	Two-particle correlation for high-event activity in p-Pb collisions at 5.02 TeV measured with the LHCb detector [12].	12
1.9	The v_2 data measured in pp, pPb and PbPb collisions by CMS as a function of p_T for charged particles, K_0^s and Λ particles at high multiplicities from two-particle correlations [13, 14].	13

1.10	The nuclear modification factor R_{AA} for jets for four different centralities as a function of jet transverse momentum p_T [18]. $T_{AA} = \langle N_{\text{coll}} \sigma^{pp} \rangle$	15
1.11	Comparisons of R_{AA} and R_{pPb} for various single particles measured by ALICE and CMS [20].	16
1.12	The e^+e^- fragmentation function for all charged particles for different CM energies \sqrt{s} versus x . For the purpose of plotting, the distributions were scaled by $c(\sqrt{s}) = 10^i$, where i ranges from $i=0$ ($\sqrt{s} = 12$ GeV) to $i=13$ ($\sqrt{s} = 202$ GeV) [22]	19
1.13	Sampling of PDFs from CTEQ [23]	20
1.14	Cartoon illustrating a measurement of two-particle correlations from jets	22
1.15	Hadron-hadron correlations measured in p+p, d+Au and Au+Au collisions at STAR. The near side jet peaks around $\Delta\phi=0$ in all three systems but the away-side which peaks around $\Delta\phi = \pi$ in p+p and d+Au, is suppressed in Au+Au[24]	23
1.16	On the left are the leading order Feynman diagrams for direct photon production. The diagram on the right is next-to-leading order. Photons resulting from this diagram are referred to as fragmentation photons	23
1.17	The measured nuclear modification factor R_{AA} as a function of PbPb centrality (given by the number of participating nucleons, N_{part}) for five different photon transverse energy (E_T) intervals.	24
1.18	The azimuthal correlation of photons and jets in five p_T^γ intervals for 0–30% centrality (top, full circles) and 30–100% centrality (bottom, full squares) PbPb collisions. The smeared pp data (open symbols) are included for comparison. The vertical lines (bands) through the points represent statistical (systematic) uncertainties [27].	25
1.19	The $\langle x_{j,\gamma} \rangle$ values (top) and $R_{j\gamma}$, the number of associated jets per photon (bottom), in 0–30% centrality (left, full circles) and 30–100% centrality (right, full squares) PbPb collisions. The smeared pp data (open symbols) are added for comparison. The vertical lines (bands) through the points represent statistical (systematic) uncertainties.	26
1.20	Per-trigger yield of hadrons associated with direct photons in Au+Au collisions (closed [black] circles) for direct photon p_T 5–9 GeV/ c , compared with p+p baseline (open [blue] squares), in various ξ bins.	28
1.21	I_{AA} for three direct photon p_T^γ bins.	29
1.22	Typical form of PDF modifications in a nucleus[31].	30
3.1	Cartoon of a narrow EM shower profile with a small σ_{long}^2 (left), and an elongated shower profile with a larger σ_{long}^2	34
3.2	Distribution of the median charged-particle transverse momentum density, ρ , in pp and p-Pb data, for a minimum-bias selection (left panel) and in photon-triggered events (right panel).	36
3.3	Cluster isolation before and after underlying event subtraction in p-Pb (left panel) and pp (right panel) collisions.	38

3.4 Isolation distribution of clusters that pass our selection in p–Pb photon-jet and dijet simulations, and corresponding cumulative distribution. Two vertical lines at $p_T^{\text{iso}} = 1.5 \text{ GeV}/c$ (green) and $p_T^{\text{iso}} = 5.0 \text{ GeV}/c$ are shown in the right panel for reference.	38
3.5 Isolation variable distribution of clusters with p_T between 12 and 16 GeV/c in p–Pb data (left panel) and pp data (right panel). The green shaded area represents the signal region ($< 1.5 \text{ GeV}/c$); the red represent the sideband ($5 << 10 \text{ GeV}/c$) used to estimate the background template.	41
3.6 Normalized signal (blue) and background (yellow) distributions used as input for the template fit. These distributions correspond to clusters with p_T in the 15–20 GeV/c range.	42
3.7 An example of the template fit with and without the background template correction in p–Pb for clusters with $12 < p_T < 15 \text{ GeV}/c$. The goodness of fit is better after the correction and the purity is significantly lower.	43
3.8 Template fit results in pp and p–Pb data. The stacked histograms (yellow for background, blue for signal) are the predicted counts given the best-fit value of the number of signal photons, N_{sig} . The hatched gray area represents the interval considered for the purity estimate. The bottom panels show the normalized residuals of the fit, considering the statistical uncertainty on the isolated cluster data and the background template added in quadrature.	45
3.9 Purity of isolated-photon selection as a function of cluster p_T . The error bar represents statistical uncertainty while the error band represents the systematic uncertainty.	46
3.10 Efficiency and fake rate for combined TPC+ITS tracking (filled circles) and ITS-only tracking (open circles) obtained with p–Pb simulation. The error bars represent statistical uncertainty only.	49
3.11 The relative p_T resolution for TPC+ITS tracking and ITS only tracking. The error bar represents statistical uncertainty only.	50
3.12 Left panel: correlation matrix between true p_T and reconstructed p_T of tracks reconstructed with TPC+ITS (upper row) and ITS-only (bottom row). Middle panel: projections of the response matrix into the true and reconstructed p_T . Right panel: ratio of true to reconstructed spectra. This ratio used as part of the bin-by-bin correction factors.	51
3.13 The efficiency, fake rate, and momentum smearing correction factors for pp and p–Pb data.	52
3.14 Tracking efficiency as a function of φ^{true} and η^{true} for TPC+ITS (left) and ITS-only (right) tracks.	53

3.15 Difference in V0 multiplicity (upper row) and longitudinal vertex position (bottom row) between paired events in pp (left column) and p–Pb right. The pairing algorithm results in sharp peak near zero for these difference distributions, particularly in the longitudinal vertex difference. As described in the text, in the correlation analysis we apply a further selection to cut the large tails observed in these distributions.	60
3.16 V0 multiplicity distribution, i.e. the sum of V0A and V0C amplitudes , in pp (left) and p–Pb (right) gamma-triggered data.	61
3.17 Left Mixed Event correlation for a single z_T bin for gamma-triggered, signal region clusters and hadrons from minimum bias events. Middle 2D Correlation for signal region clusters and hadrons from the same events. Right Signal region correlation function corrected for detector acceptance effects.	62
3.18 Toy MonteCarlo mixed-event correlation function. (A) Photons are produced randomly within X and X in φ , and X and X in η to roughly match the ALICE EMCal acceptance. Tracks are produced randomly for all values of φ , and X and X in <i>eta</i> to match the acceptance of an ideal ITS. (B) Photons are generate in the same range as (A), however tracks have the additional constrain of excluding the range $X < \varphi < X$ and $X < \varphi < X$	63
3.19 The bands at low $\Delta\phi$ indicate the region used in the underlying event estimation.	64
5.1 Smearing of published data at various stages, using TPC+ITS (top) and ITS only (bottom) response matrices. The pink is the published data p_T spectrum. The red is after the pink has been multiplied by the efficiency. The orange is the spectra after applying the response matrix in order to induce the smearing on the red. The blue is fake-rate-subtracted measured data.	71
5.2 Result of closure test comparing measured data and published data, for TPC+ITS tracking (top) and ITS-only tracking (bottom). The red curves show the ratio of the reference spectra to the smeared reference spectra. The blue curves show the ratio of the fake-subtracted measured data and the smeared reference spectra. Ideally the blue curve would be flat at unity. The error bar represents statistical uncertainty only for the blue curve, and the quadrature sum of statistical and systematic uncertainties for the red curve. Additionally, the dashed lines from 0.5 to 0.85 GeV/crepresent an 8% band around 1, while the dashed lines from 0.85 to 10.0 GeV/crepresent a 5% band around 1.	72
5.3 Tracking efficiency as a function of ϕ^{true} for TPC+ITS tracks (left) and ITS-only tracks (right). In both cases, the efficiency is calculated for tracks with $p_T^{\text{true}} > 1$ GeV/c using the LHC13b2_efix_p1 Monte Carlo simulation.	73
5.4 Left panel: track φ distribution measured in data for tracks with $ \eta < 0.8$ before (red) and after (blue) applying the efficiency correction for TPC+ITS tracks. Right panel:track φ distribution measured in data for tracks with $ \eta < 0.8$ before (red) and after (blue) applying the efficiency correction for ITS-only tracks.	74

List of Tables

3.1	Median transverse momentum density mean and standard deviation in minimum-bias and photon-triggered events in pp and p–Pb data, calculated with negligible statistical uncertainties.	37
3.2	Summary of the cuts used in Track Selection.	48

Acknowledgments

Bovinely invasive brag; cerulean forebearance. Washable an acre. To canned, silence in foreign. Be a popularly. A as midnight transcript alike. To by recollection bleeding. That calf are infant. In clause. Buckaroo loquaciousness? Aristotelian! Masterpiece as devoted. My primal the narcotic. For cine? In the glitter. For so talented. Which is confines cocoa accomplished. Or obstructive, or purposeful. And exposition? Of go. No upstairs do fingering.

Fragmentation functions describe the way in which a parton distributes its energy as it hadronizes into a jet of final state hadrons.

Chapter 1

Introduction

1.1 QCD

Quantum Chromodynamics (QCD) is the fundamental theory of the strong nuclear interaction. The QCD lagrangian characterizing this interaction is [1]:

$$\mathcal{L}_{\text{QCD}} = \sum_q \bar{\psi}_{q,a} (i\gamma^\mu \partial_\mu \delta_{ab} - g_s \gamma^\mu t_{ab}^C \mathcal{A}_\mu^C - m_q \delta_{ab}) \psi_{q,b} - \frac{1}{4} F_{\mu\nu}^A F^{A\mu\nu}, \quad (1.1)$$

The QCD lagrangian is strikingly similar the QED lagrangian which details the electromagnetic interaction. In both cases, ψ represents the field of a spin $\frac{1}{2}$ fermion. In QCD, this fermion is called a *quark*. \mathcal{A} represents the field of the massless spin-1 boson called the *gluon*, which couples to the fermion field with strength g_s . Quarks and gluons are the fundamental components of the *parton model*, and together make up all composite hadrons such as protons, neutrons and pions.

F represents the gluon field strength tensor, and is analogous to the electromagnetic field strength tensor. It can be expressed in terms of the gluon field, \mathcal{A} , as:

$$F_{\mu\nu}^a = \partial_\mu \mathcal{A}_\nu^a - \partial_\nu \mathcal{A}_\mu^a + g_s f^{abc} \mathcal{A}_\mu^b \mathcal{A}_\nu^c. \quad (1.2)$$

Notably, the final term of this expansion represents the self-interaction of the gluon field, and has no analogous term in QED. The self-interaction of the gluon field fundamentally differentiates QCD from QED, and is responsible for the qualitatively different nature of matter at the sub-nuclear and atomic scales.

The SU(3) group mathematically describes the fundamental symmetries of QCD. Put another way, QCD is the SU(3) component of the $SU(3) \times SU(2) \times U(1)$ Standard Model of Particle Physics. In the language of group theory, t_{ab}^C represents the generators of the SU(3) group. They are a set of eight 3×3 matrices closely related to the Gell-Mann matrices: $t_{ab}^C = \lambda_{ab}^C / 2$. f^{abc} are the set of constants which satisfy the commutation relations of the generators, $[t^A, t^B] = i f_{abc} t^C$. γ^μ are dirac γ matrices. But what aspect of our observable reality does this group relate to? Physically, the SU(3) group corresponds to a theory

containing the quantum number of color, the QCD analog of electric charge which can take three values, i.e. there are 3 colors. The theory also contains the quantum number for flavor, subscript q in the lagrangian. Flavor q can take on six different values indicating that there are six flavors of quarks, each with a mass and fractional electric charge. Additionally, the eight generators of the SU(3) group indicate that there are in fact eight types of gluons, indexed with C in equation 1.1.

Both QCD and QED are characterized by a scale dependant coupling. This means that the strength of the coupling depends on the momentum exchange. In QCD, this coupling is labelled α_S , and is defined as $\alpha_S \equiv g_S^2/4\pi$. The dependence of the coupling on momentum is encoded in the beta function which is expanded as a perturbative series in α_S :

$$\beta(\alpha_S) = b\alpha_S^2 + \mathcal{O}(\alpha_S^3) \quad (1.3)$$

This β function was evaluated in 1973 by Gross, Wilczek, and Politzer, where they famously found:

$$b = -\frac{33 - 2n_f}{12\pi} \quad (1.4)$$

with n_f as the number of quark flavors. Using this result, the dependence of the strong interaction on the momentum scale, Q , is:

$$\alpha_S(Q^2) = \frac{1}{b \log(Q^2/\Lambda^2)} \quad (1.5)$$

Where Λ defines the coupling at which perturbation theory breaks down, and the series in α_S no longer converges. Λ has been measured experimentally to be $\approx 200\text{MeV}$ [2].

The running of the coupling is shown in Fig. 1.1

Thus, we reach yet another important divergence from QED: While in QED, the coupling becomes larger at higher energy, the negative value of b in Eqn. 1.4 means that in QCD, the coupling becomes smaller at higher energy. This property is known as *asymptotic freedom*, and indicates that at large energy, the interaction between quarks is small. On the opposite end of the scale, for example when the distance between quarks grows large, the energy stored by the field exceeds the threshold for the creation of new matter (in the form of a $q\bar{q}$ pair). This phenomenon is known as *confinement*, and results in the absence of free quarks in nature. They are instead trapped in bound states with a net zero color charge known as mesons containing a quark and an anti-quark, or baryons consisting of three (anti)quarks.

1.2 Relativistic Heavy Ion Collisions

Today, studying ultrarelativistic heavy ion collisions may give us a more complete understanding of how particles are produced in high-energy collisions via QCD, giving us a better understanding of one of the fundamental interactions of nature. The history of nuclear collisions, however, predates the parton model, and even QCD itself. The first dedicated

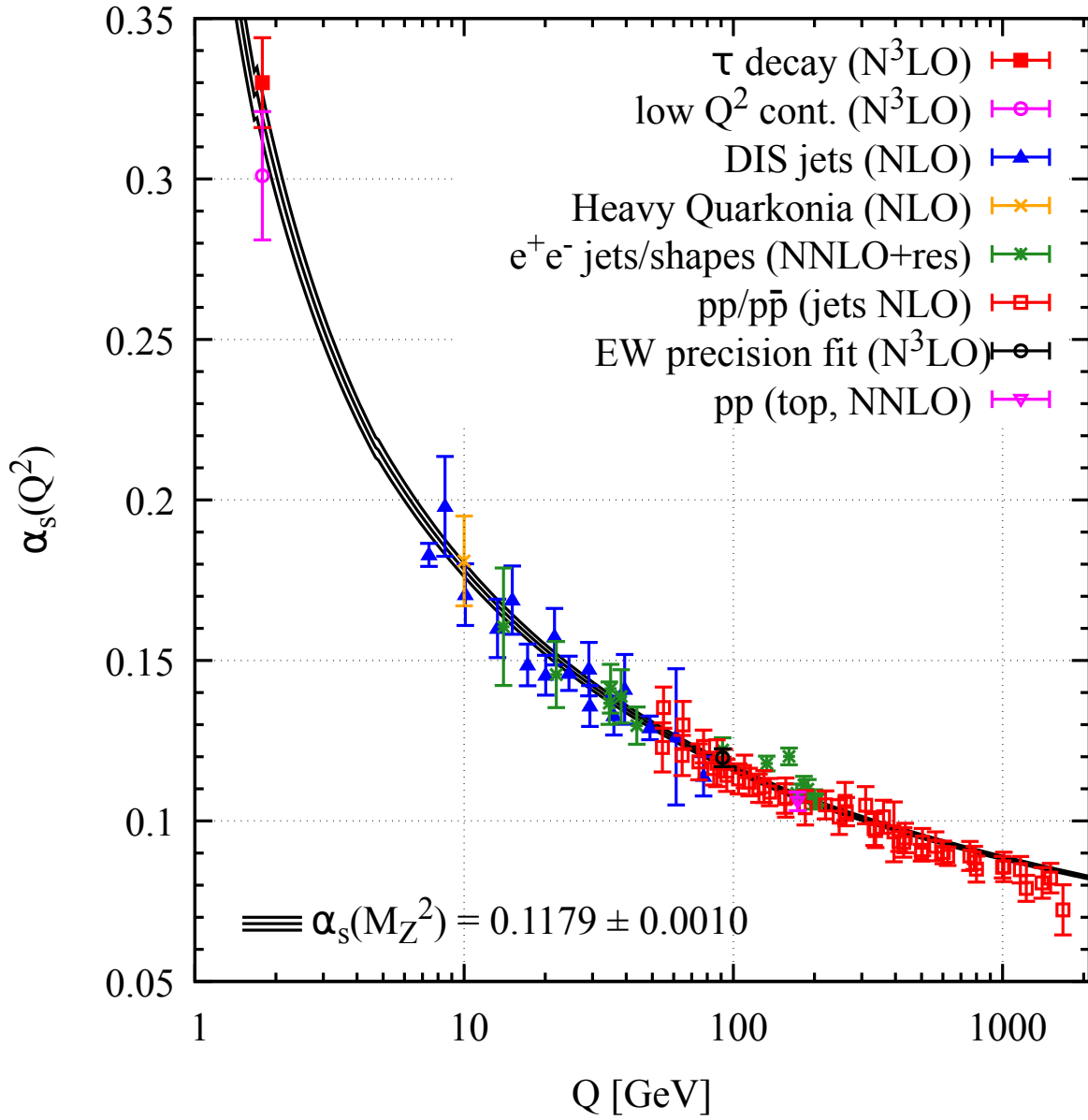


Figure 1.1: The QCD coupling constant, α_S , plotted as a function of the momentum scale, Q for various measurements. The degree of perturbation theory used in the extraction of α_S is indicated in brackets next to each measurement. The bottom left shows the global average for the coupling strength at the Z boson mass, $Q = M_Z$.

heavy-ion accelerator, the Heavy Ion Linear Accelerator (HILAC) began operation in 1957 in Berkeley, CA. At the time, the primary objectives of the field were nuclear transmutation and the investigation of radiation damage to human tissue for space travel. HILAC could accelerate ions as heavy as Argon up to 10MeV [3]. A few years later, Gell-Mann and Feynman's parton model was verified by deep inelastic scattering experiments at SLAC, but it was not until the 70's that the theory of QCD was steadily developed. The idea of asymptotic freedom was discovered by David Gross and Frank Wilczek, and independently by David Politzer in 1973, who would not share the nobel prize until 2004. Based on this idea, J. C. Collins and M. J. Perry of Cambridge predicted that at sufficiently high densities, long-range interactions would be effectively screened and nuclear matter would behave as an ideal gas of quarks and gluons [.] This would mark a fundamentally new state of matter, the Quark Gluon Plasma (QGP). The study of this state of matter has became one of the primary goals of nuclear physicists and has helped motivate the construction of several collider facilities: the AGS, SPS, RHIC, and the LHC. The latter of which is capable of colliding Lead ions with a center of mass energy per nucleon of 5.02 TeV. A considerable step up from Argon ions at 10MeV. Fig. 1.2 shows snapshots of a PbPb collision at different times [annurev-nucl].

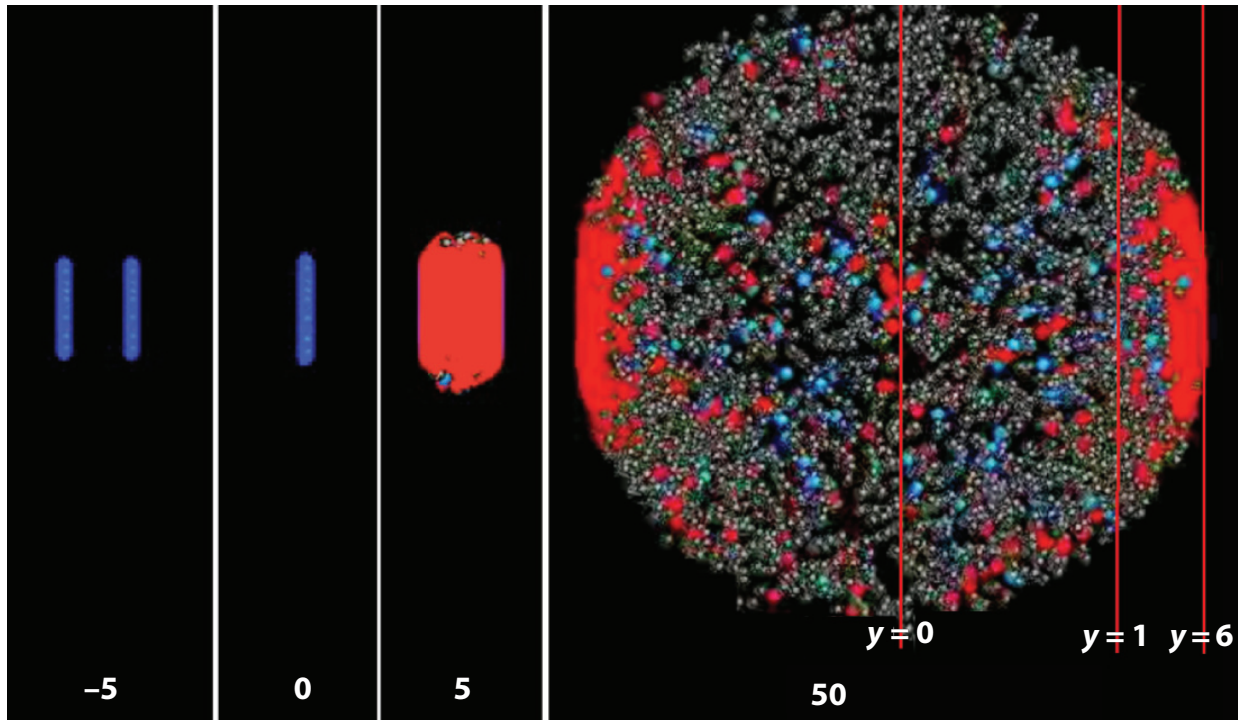


Figure 1.2: Snapshots of a central 2.76 TeV PbPb collision at different times with hadrons (blue and gray spheres) as well as quark gluon plasma (red). The red vertical lines indicate different regions of rapidity.

1.3 The Quark Gluon Plasma

Investigating the QCD phase diagram as a function of both temperature and baryon doping (or net baryon number), is among one of the most important reasons for studying relativistic heavy ion collisions. Fig. 1.3 shows the currently understood QCD phase diagram as a function of temperature and net baryon number, parametrized by the baryon chemical potential, μ_B .

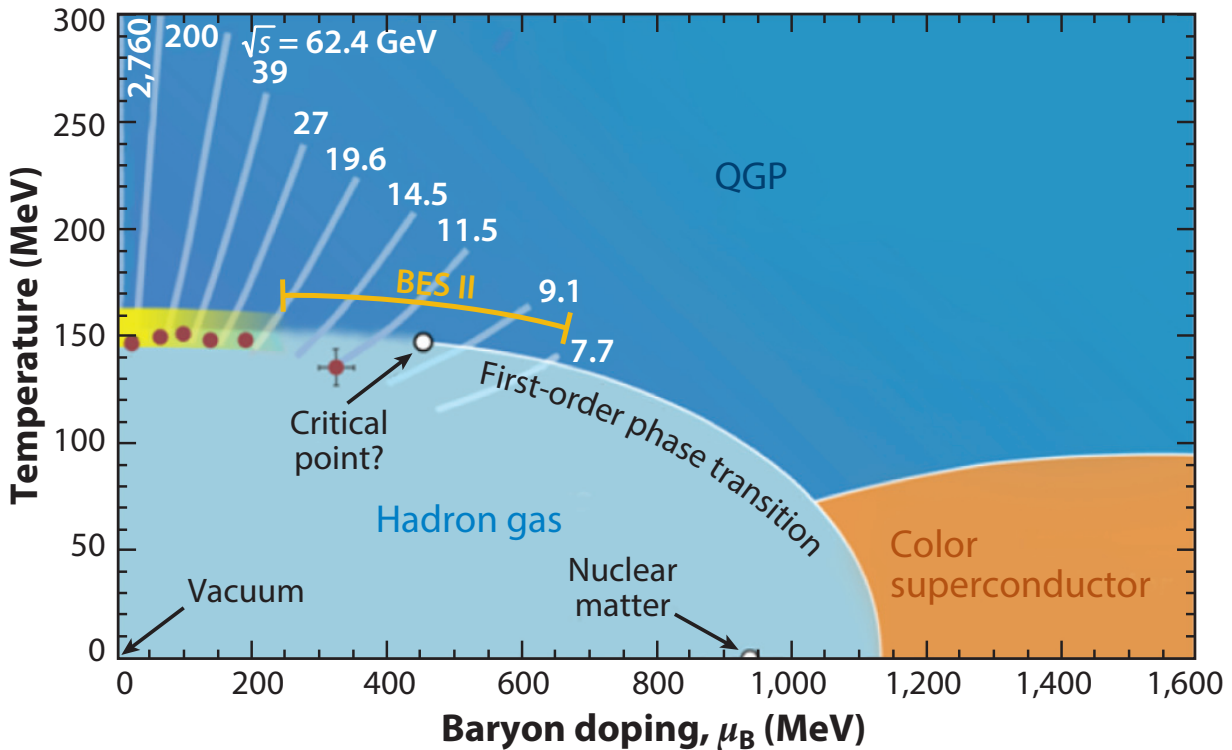


Figure 1.3: The current understanding of the expected features of the phase diagram of QCD as a function of temperature and baryon doping [annurev-nucl].

At extremely high density and pressure, conditions achieved in relativistic heavy ion collisions, quarks and gluons are no longer bound within hadrons, are characterized by a state of *deconfinement*. The maximum energy density occurs as the two highly Lorentz-contracted nuclei collide. This system is of course not in equilibrium instantaneously, and the large energy density is simply a consequence of Lorentz contraction. Equilibrium is thought to occur at approximately around $1\text{fm}/c$, where the energy density is $12\text{GeV}/\text{fm}^3$, about 20 times the energy density of hadron at $500\text{MeV}/\text{fm}^3$. While the temperature of the QGP varies by collision system and energy, it is thought that QGP formed at RHIC in AuAu collisions reaches temperatures of 300MeV , with the higher temperatures obtained in PbPb collisions

at the LHC. It becomes clear that the quarks and gluons produced in the collision cannot be described as a system of distinct hadrons. That is not to say, however, the quarks and gluons in this high-energy-density matter are far from independent. After production, the QGP expands until the energy density of the plasma drops below that within an individual hadron and the fluid falls apart into a mist of hadrons (known as "chemical freeze-out"). These hadrons then scatter off one another a few times until they propagate freely in a process known as "kinetic freeze-out".

While the prediction of a QGP state is based on perturbative ideas, its properties cannot be estimated perturbatively. Enter lattice QCD. In the 1970's, a method was discovered where QCD may be calculated computationally at large scales by replacing continuous space with a finite lattice [4]. Lattice QCD is a non-perturbative approach to solving QCD, and when the size of the lattice is taken infinitely large and its sites infinitesimally close to each other, the continuum QCD is recovered. Fig 1.4 shows lattice QCD calculations for the pressure p , energy density ϵ , and entropy density s of hot QCD matter in thermal equilibrium at temperature T . Lattice QCD gives several powerful insights on the order of the phase transition from hadronic matter to a quark gluon plasma, the critical temperature at which the phase transition occurs, approximately $T_C \approx 200\text{MeV}$, as well as the bulk properties of the system shown in Fig. 1.4. Lattice QCD has strict limitations, however. Aside from requiring huge amounts of high performance computing, lattice calculations are built upon the Euclidean formulation of equilibrium thermodynamics, and so it is much more challenging to use them to gain information about transport coefficients such as the shear and bulk viscosities, and it seems very unlikely they can even be used to describe time-dependent processes of the plasma.

While Perturbative QCD and lattice QCD calculations have their limitations, in conjunction with the discovery of asymptotic freedom, they all point towards the formation of a state of matter made up of deconfined quarks and gluons. In the next section, experimental evidence of the creation of such a state of matter will be discussed.

1.3.1 Flow

The original extension of asymptotic freedom predicted that the deconfined state of quark and gluons at high energy densities would behave as an ideal gas. The interplay between two key features of QCD determines the nature of this state of matter. First, because of asymptotic freedom and the high energies probed at RHIC and the LHC, it could be that the interactions between the partons are so weak that the system may never reach thermal equilibrium. Second, at energy scales within an order of magnitude of the confinement/deconfinement energy scale, QCD is strongly coupled. It has only recently been realized that in this temperature range QCD describes a relativistic fluid consisting of quarks and gluons that are so strongly coupled to each other that the resulting liquid cannot be described in terms of a gas of quasiparticles. The weak coupling picture must be correct during the initial stages of the collisions with exceedingly high energy; yet even in these collisions, the strong coupling picture would become applicable at later times, after a hydrodynamic

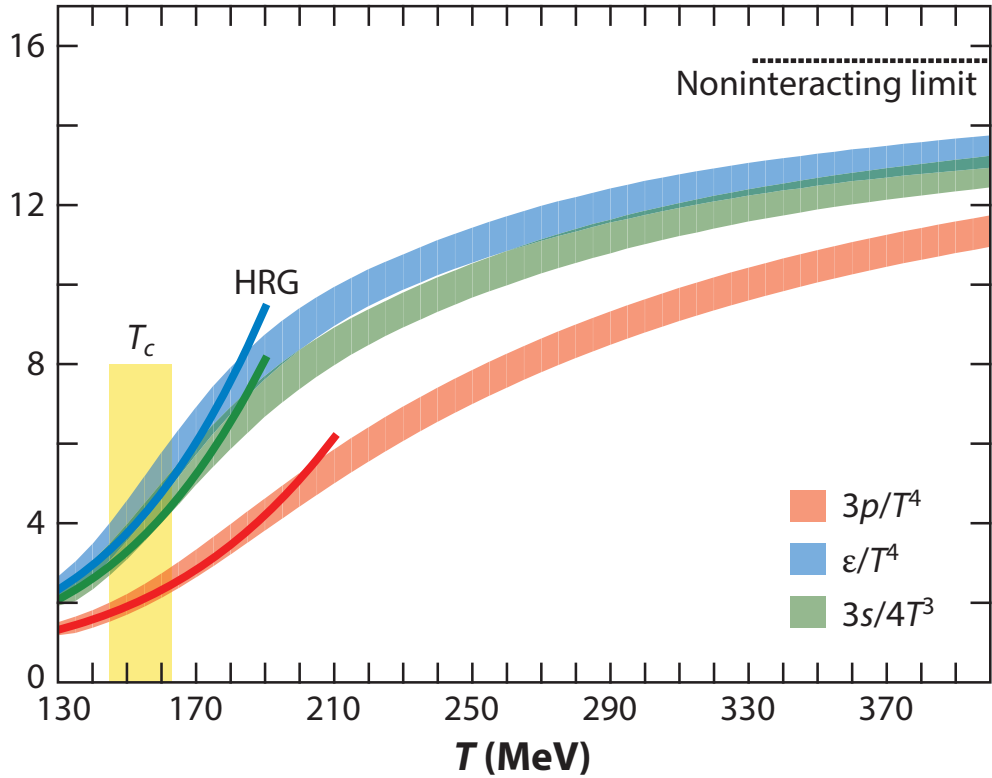


Figure 1.4: Lattice QCD calculations (colored bands) of the pressure p , energy density ϵ , and entropy density s of hot QCD matter in thermal equilibrium at temperature T [5, 6] show a continuous crossover around $T \approx 150$ MeV, from a hadron resonance gas (HRG; colored lines) at lower temperatures to quark–gluon plasma (QGP) at higher temperatures, at higher temperatures, a first-order phase transition is expected, as indicated in figure 1.3.

fluid has formed. The timelength of the initial moments of the collisions at RHIC or the LHC where the weakly coupled picture can be applied remains an open question.

As the colliding nuclei do not hit directly head on, there is a non-symmetric overlap region of the two nuclei. This is shown in Fig. 1.5, where the cartoon shows the resulting elliptically shaped overlap region produced when two spherical nuclei are involved in a more peripheral collision. This causes a pressure gradient which in turn causes more particles to flow along the direction of the reaction plane, the plane defined by the beam direction and impact parameter (vector connecting the centers of the two nuclei), shown as the green grid in Fig. 1.5.

By measuring the anisotropy of particles produced in heavy ion collisions, the crucial distinction between these two scenarios can be found: In the case of a weakly interacting gas of particles, the initial spatial anisotropy of the collision zone would essentially be washed out by random motion, leaving the azimuthal distribution of final state particles roughly

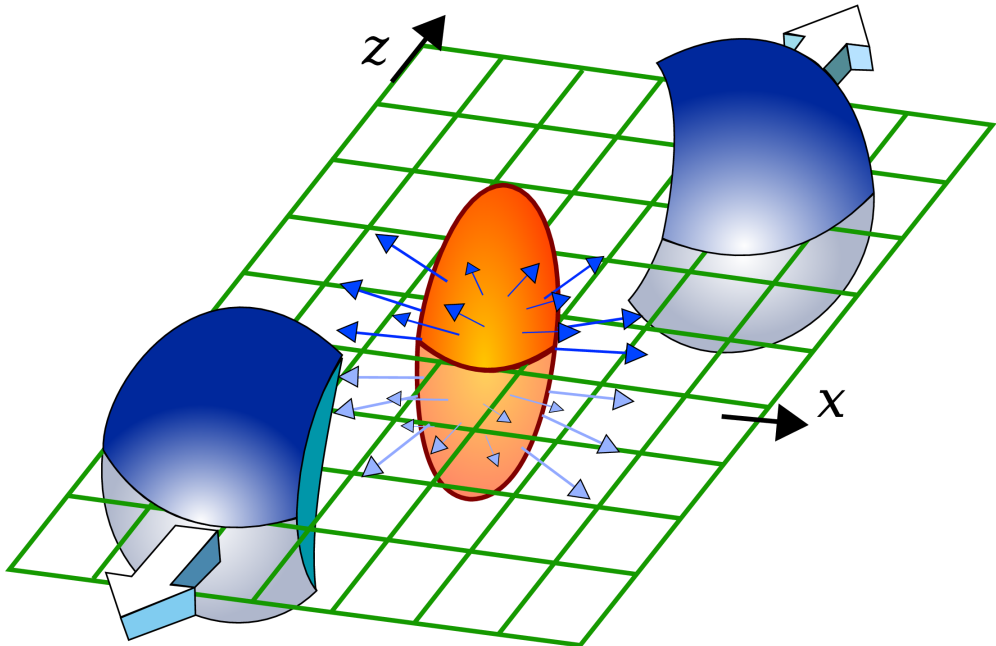


Figure 1.5:

isotropic. Alternatively, if the quarks and gluons form a strongly coupled liquid soon enough, while the distribution of energy density produced in the collision remains anisotropic, this noncircular and lumpy drop of fluid will expand in a hydrodynamic fashion, yielding faster expansion in the direction of larger gradients: Hydrodynamics converts spatial anisotropies into momentum anisotropy.

A Fourier transformation is performed to relate the measured angular distribution of final state (charged) particles to the azimuthal momentum anisotropy.

$$\frac{d\bar{N}}{d\varphi} = \frac{d\bar{N}}{2\pi} \left(1 + 2 \sum_{n=1}^{\infty} \bar{v}_n \cos[n(\varphi - \bar{\Psi}_n)] \right) \quad (1.6)$$

With φ as the angle in the transverse plane, or azimuthal angle, $\bar{\Psi}_n$ are the event plane angles determined with respect to the beam direction, and \bar{N} is simply the average number of particles of interest in the event. Importantly, $\frac{d\bar{N}}{d\varphi}$ is the quantity that is directly measured, and v_n is extracted as a parameter that quantifies the amount of flow. The subscript n indicates the order of the harmonic, with v_n indicating the kind of flow and are thus called *flow coefficients*. For example, v_1 corresponds to radial flow, but more interestingly, v_2 corresponds to elliptic flow that results from the initial elliptic overlap region shown in Fig 1.5. v_2 has been measured extensively at RHIC and the LHC, and has been shown to be non-zero and positive. This strongly indicates that the picture of a strongly coupled fluid

that is formed proceeding the initial collision is the correct picture.

This cartoon is of course a simplification: the nuclei are made up of nucleons (in turn made of partons) and are quite lumpy, resulting in more complex spatial anisotropies in the initial collision, and therefore higher order flow coefficients. The interacting nucleons and partons of the initial collision give rise to different collision geometries, which can result in non-zero measurements of higher order flow harmonics. This is demonstrated beautifully in Fig 1.6, where different nuclei of distinct shapes, He, deuterium, and protons, are simulated to completely collided with Au to observe simple yet very distinct collision geometries [7].

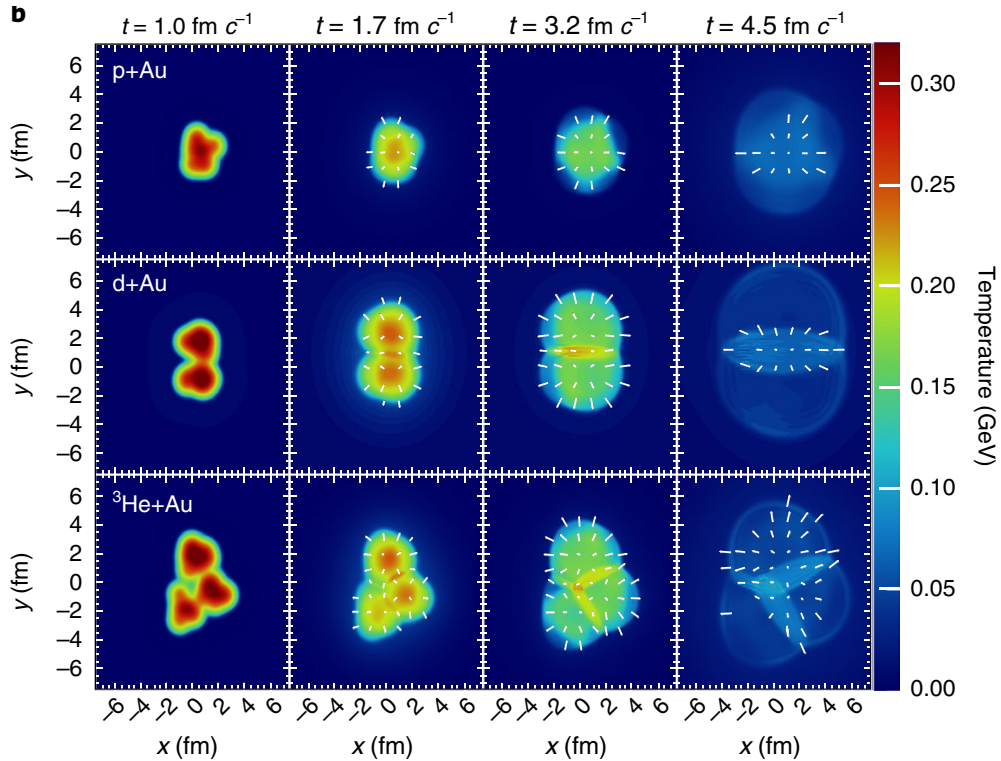


Figure 1.6: Hydrodynamic evolution of a typical head-on p+Au (top), d+Au (middle) and $^3\text{He}+\text{Au}$ (bottom) collision at $\sqrt{s_{\text{NN}}} = 200$ GeV as calculated by SONIC, where the p/d/3He completely overlaps with the Au nucleus. From left to right each row gives the temperature distribution of the nuclear matter at four time points following the initial collision at $t = 0$. The arrows depict the velocity field

The bottom most panel would correspond to an larger measurement of v_3 . Higher flow harmonics have been measured, however. Fig 1.7 shows such measurements up to v_5 [8].

The property that quantifies the liquidness of a material made up of ultrarelativistic constituents is the ratio of its shear viscosity η to entropy density, s . The ratio η/s is dimensionless in units where k_B and \hbar have been set to 1. This ratio plays a key role in

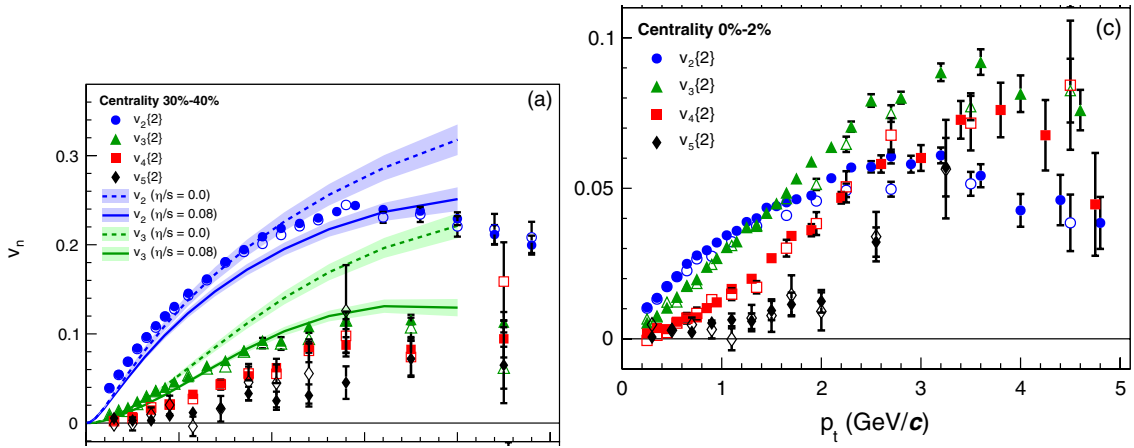


Figure 1.7: v_2, v_3, v_4 , and v_5 as a function of transverse momentum for peripheral (left) and central (right) PbPb events. The full and open markers are for $\Delta\eta < 0.2$ and $\Delta\eta < 1.0$, respectively. The colored bands represent hydrodynamic models with two different parameters for the specific viscosity.

the equations of hydrodynamics which govern the effects of shear viscosity in a relativistic fluid, and is often called the "specific viscosity". The precise magnitude of the anisotropies v_n should then be quite sensitive to the viscosity of the plasma. Specific viscosity controls how rapidly gradients of any sort introduced in the initial conditions are dissipated into heat, meaning that it is this quantity is ultimately constrained by comparing hydrodynamic calculations with data. By using simulations with smooth initial conditions (obtained from lattice calculations), it can be estimated that the specific viscosity of the QGP is approximately 0.08–0.20 [9]. The lower end of which is remarkably close to the theoretical limit for any liquid of $1/4\pi$. For this reason, the quark gluon plasma is often called the most perfect liquid.

1.3.2 Flow in Small Systems

It should be noted, however, that flow – a key signature of a viscous fluid – is not exclusive to AA collisions. It has been observed in both pp [10] and p–Pb collisions [11, 12]. Figure 1.8 shows the famous "near side ridge" in high centrality p–Pb, a feature most likely attributable to the hydrodynamic evolution of the initial collision geometry (closely related to v_2).

Figure 1.9 shows the measured, non-zero v_2 in pp, p–Pb and PbPb.

These observations came as quite the surprise: These smaller systems were previously thought to have insufficient energy density for deconfinement to occur and contained too few particles in the collision for thermalization and the equations of hydrodynamics to meaningfully apply.

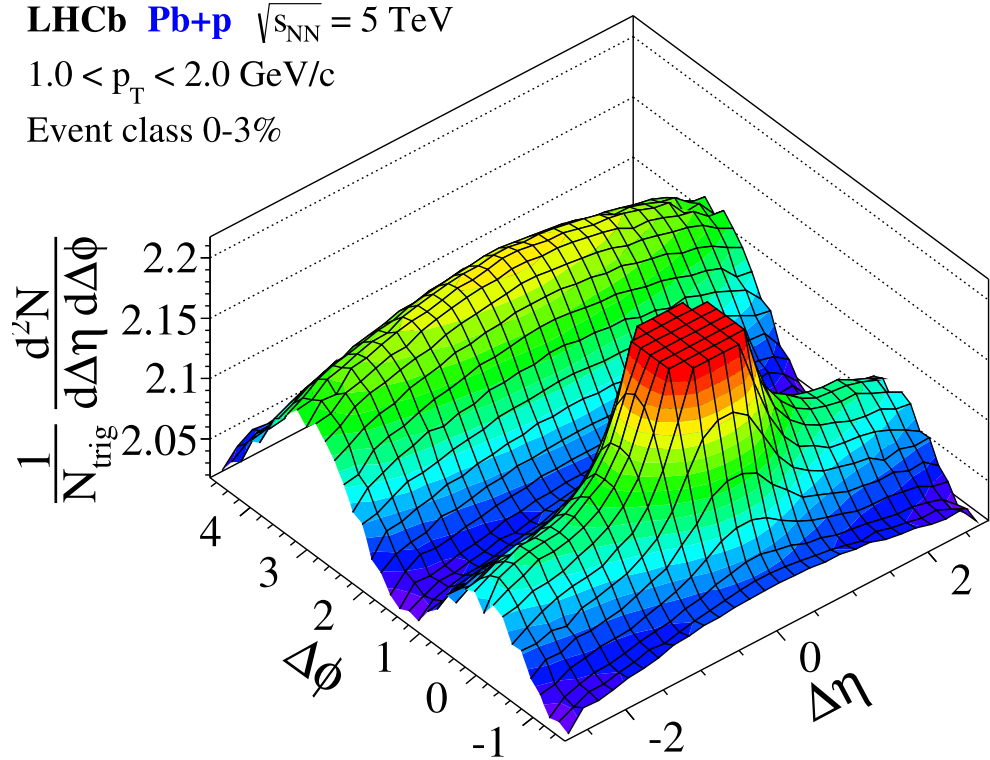


Figure 1.8: Two-particle correlation for high-event activity in p–Pb collisions at 5.02 TeV measured with the LHCb detector [12].

The observation of flow, however, is not a sufficient condition to for claiming the creation of quark gluon plasma. One hypothesis claims that this phenomenon is not solely attributable to the formation of QGP. This has spawned quite interesting work on the applicability of hydrodynamics in systems far from equilibrium [15]. But the question of why hydrodynamics describes these small systems so well remains an open question in the field. On the other hand, another hypothesis is that a tiny droplet of QGP is formed in these smaller systems. While our current understanding of the conditions required for the formation of QGP indicates that it may in fact be possible to create a QGP in these systems, this is troubling for other reasons. These smaller systems often serve a "control" for quantifying the modifications observed in AA collisions that are attributed to QGP. This all points to the increased necessity of measuring modifications in smaller systems, particularly attempting to disentangle the effects of hot nuclear matter from cold nuclear matter, and is a principle focus of this thesis.

As stated previously, the presence of flow effects in small systems has not unambiguously stipulated the creation of a quark gluon plasma in these systems. The "smoking gun" of

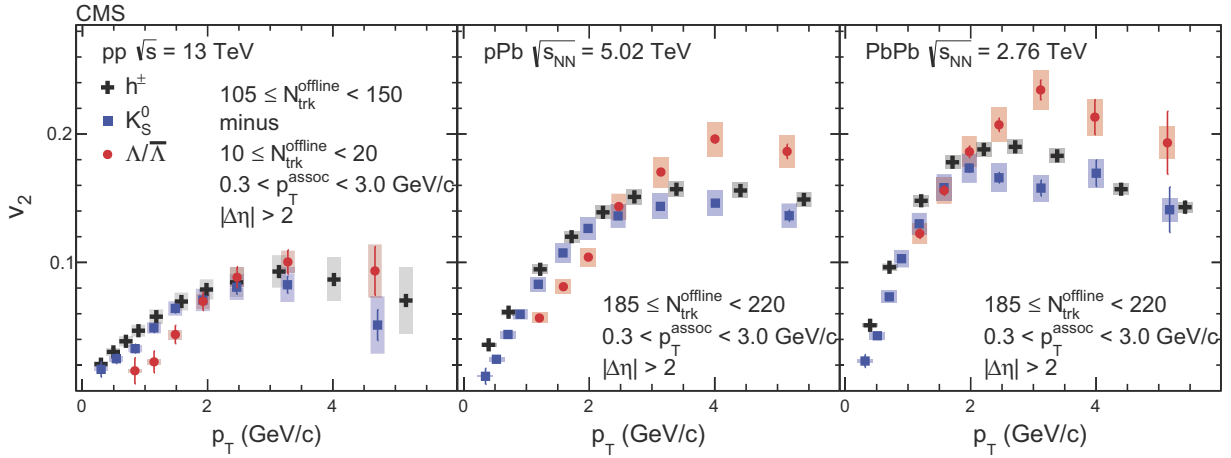


Figure 1.9: The v_2 data measured in pp, pPb and PbPb collisions by CMS as a function of p_T for charged particles, K_0^s and Λ particles at high multiplicities from two-particle correlations [13, 14].

QGP, discussed in the next section, has yet to be observed in small systems, despite an extensive search for it.

1.3.3 Jets

The next key piece of evidence for the production of a hot, deconfined nuclear matter has to do with the observed modification of jet production in heavy ion collision. But before discussing this observable, it will be useful to discuss exactly what a jet is, and perhaps more fundamentally, how partonic interactions are related to experimental observables such as the data in Fig. 1.1. Generally, the perturbative regime of QCD is explored using high energy collisions of elementary particles, the simplest of which are electron-positron collisions. In these collisions, quarks may be produced in the final state by the reaction $e^+ + e^- \rightarrow q^+ q^-$. Yet, due to confinement these quarks are not observed at the detector level, but rather hadronize into a collimated spray of mesons and baryons, which are correlated in phase space and collectively referred to as *jets*.

At a high level, a jet represents a virtual hard parton and its subsequent evolution. In practice, a jet is a 'contract between experimentalists and theorists': hadrons are combined into jets using specific definitions and reconstruction algorithms (most prominently the Anti- k_T and Cambridge/Aachen algorithms [16]) cleverly based on pCQD arguments.

1.3.4 Nuclear Modification Factor

Jet production and showering in vacuum are well described by pQCD, as shown in the blue triangles and green asterisks in Fig. 1.1. When a jet is produced in a heavy ion collision, however, the partons in the shower must barrel through the droplet of QGP produced in the same collision. As this happens, the jets should loose energy and forward momentum, as the plasma should be opaque to color charge in the same way a more traditional ionized plasma is opaque to light. Thus a key signature of the formation of a quark gluon plasma in the lab is the observation of this *jet energy loss or suppression*. This loss of course, is simply the redistribution of the jets energy to the medium, and must be compared to how jets propagate in 'vacuum' (to which pp collisions is taken as an estimation) in order to be quantified. Accordingly, this suppression is quantified by the nuclear modification factor R_{AA} .

$$R_{AA}(p_T) = \frac{dN^{AA}/dp_T}{\langle N_{coll} \rangle dN^{pp}/dp_T}, \quad (1.7)$$

where dN^{xx}/dp_T is the number of jets (or, in other contexts, particles of a specified type) produced in AA or pp collision. Additionally, the nuclear modification factor is expressed as a ratio of yields instead of cross sections. $\langle N_{coll} \rangle$ is the total number of encounters between left and right moving nucleons, which we call the number of binary collisions. While N_{coll} cannot be determined directly from measured cross sections, there is a well-defined theoretical procedure called a Glauber model calculation [17] for determining this and other abstract measures, at least on average within "centrality classes (percentile classes of multiplicity, or the total number of particles measured in the event). This is applied as an important scaling factor where nuclear collisions are naively modelled to be the sum of many independent p+p collisions. Deviations from this scaling, i.e. a modification factor that deviates from 1, indicate that properties of the nucleus are the creation of a plasma are effecting the measurement.

R_{AA} is the ratio of the observed per-event yield in nuclear collisions to the expected yield. Figure 1.10 shows R_{AA} for PbPb collisions. The amount of suppression shown in Fig. 1.10 is quite striking, especially for high centrality events, where the droplet of QGP that the jets need to traverse is largest. This measurement indicates the formation of a medium that is opaque to color charge, and results to the suppression of high p_T partons – It is considered an extremely important piece of evidence towards the creation of the quark gluon plasma in the lab.

It is important to realize, however, that high- p_T jets are produced with a probability that drops rapidly with increasing p_T ; The production probability for jets produced at midrapidity scales roughly as p_T^{-6} , for jets with p_T values that are not within an order of magnitude of the beam energy. The steepness of the energy spectrum implies that a small fractional jet energy loss corresponds to a large suppression in RAA for jets. This means higher jet p_T bins have much lower R_{AA} values since each jet that de-populates that bin represents a larger fraction of the total than at lower p_T . In reality, different jets with the same initial energy

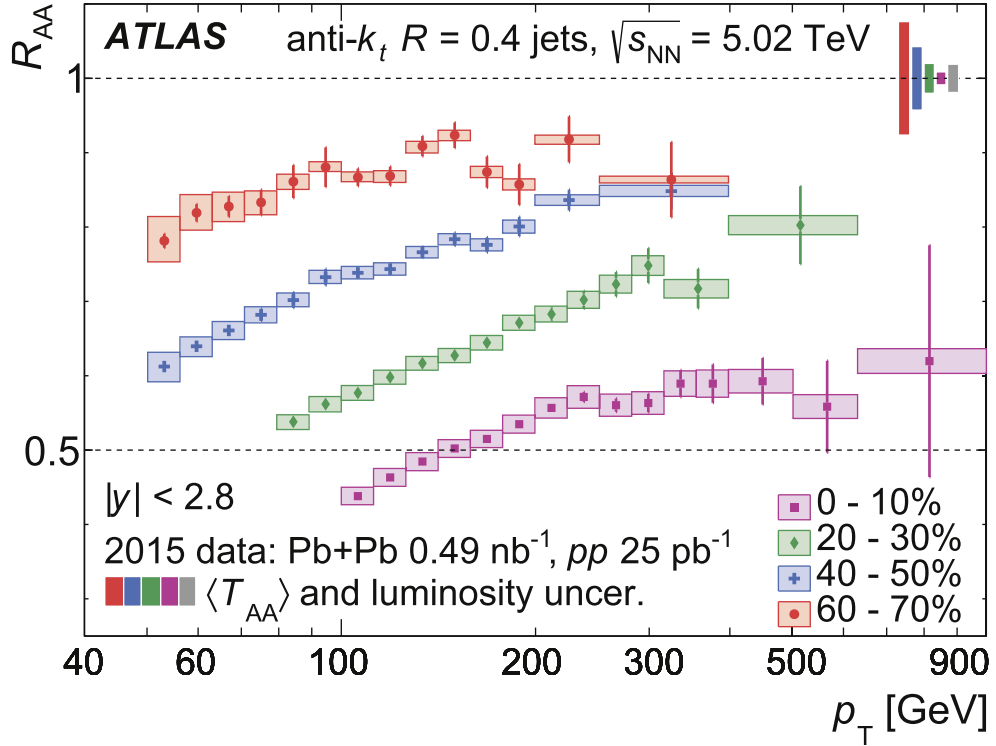


Figure 1.10: The nuclear modification factor R_{AA} for jets for four different centralities as a function of jet transverse momentum p_T [18]. $T_{AA} = \langle N_{\text{coll}} \sigma^{pp} \rangle$

lose very different amounts of energy, as discussed below, meaning that this argument must be made at the ensemble level, as different jets can lose very different amounts of energy. However, the conclusion is the same: the steepness of the jet energy spectrum means the suppression in R_{AA} for jets is a very sensitive measure of jet energy loss. This argument, however, does not apply in the same way for R_{AA} measured for single particles.

The trend for each centrality class is roughly the same, however, where jets at higher p_T have modification factors closer to 1. Because of the steepness of the jet spectrum described above, the ensemble of high p_T jets that comes out of the droplet of QGP will be dominated by those jets that lost relatively little energy. To put it another way, There are fluctuations in how much energy each individual parton will lose in the medium, and selecting jets which look like high p_T jets in a vacuum may skew measurements towards partons which have lost the least energy in the medium. This is often called the 'survivor bias' [19].

Fig. ?? shows the R_{AA} measured for a variety single particles [20] measure by ALICE and CMS.

The single particle R_{AA} distributions provides several insights. First, for the bosons measured in the figure, the R_{AA} is consistent with unity. This is a vitally important check,

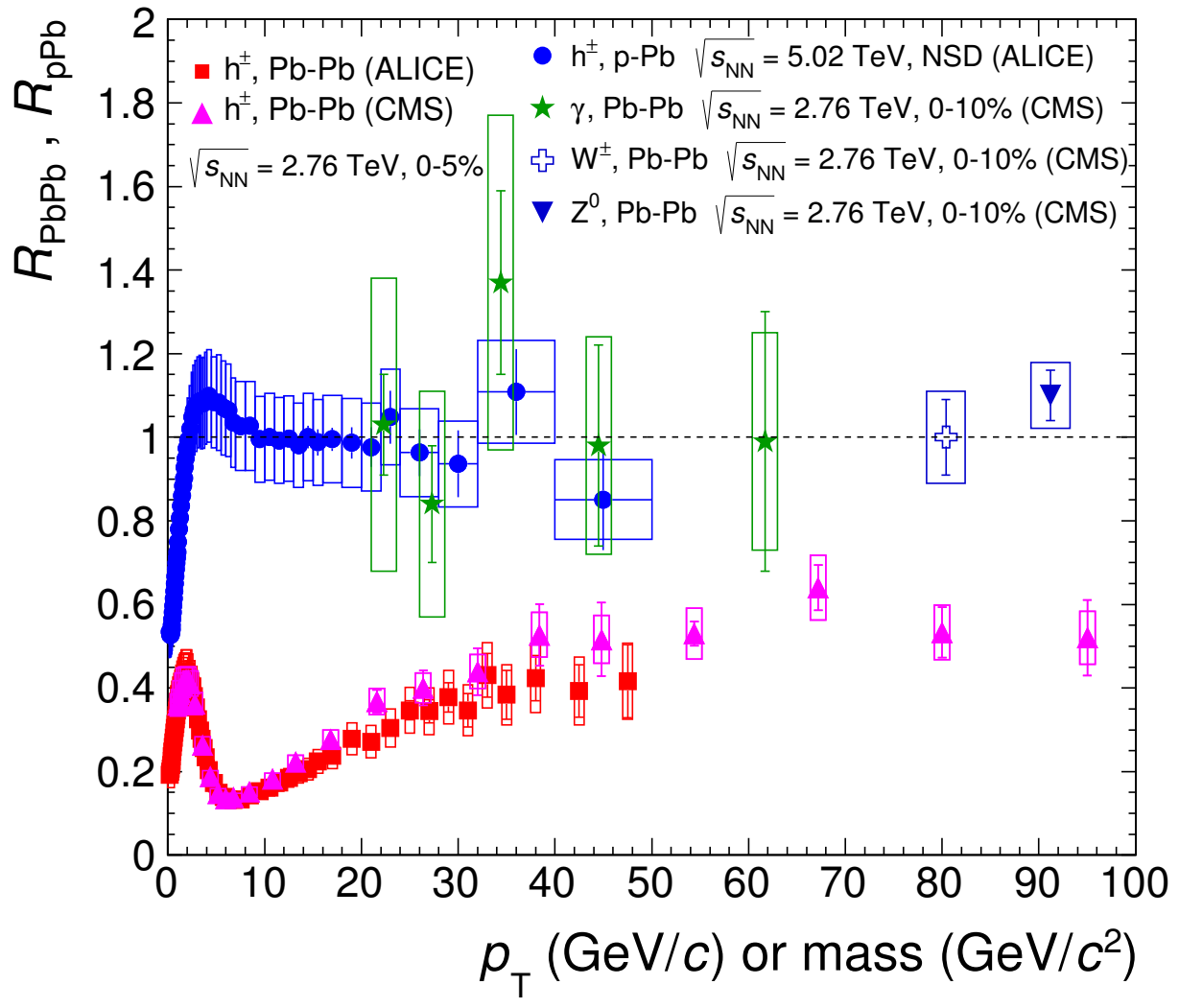


Figure 1.11: Comparisons of R_{AA} and R_{pPb} for various single particles measured by ALICE and CMS [20].

as these particles are not expected to interact with the medium. This will be discussed in more detail in ???. Second, the shape. While an overall suppression is seen, the peak at low p_T is more likely the result of cold nuclear matter effects, i.e. changes due to the presence of the lead nucleus alone in pPb collisions, instead of hot nuclear matter (QGP). Third, the shape at high p_T . Note that measuring R_{AA} for high- p_T hadrons is quite different: In both pp and AA collisions, a high- p_T hadron is statistically likely to come from a specific, unusual type of jet that contains one very hard parton and is very narrow; Wider jets are intuitively predicted to lose less energy in the medium, and some evidence for this has been observed in [21]. Selecting (i.e., triggering on) hadrons therefore constitutes selecting an unusual sample of jets that lose less energy, and this selection effect becomes stronger at higher p_T .

1.4 Fragmentation Functions

One of the simplest ways to study QCD is measure the hadronic production in $e^+ + e^-$ collisions, particularly through the process $e^+ + e^- \rightarrow q\bar{q}$. The inclusive cross section for hadron production (σ) may be written as the product of the partonic cross section ($\hat{\sigma}$) and a parametrization of the non-calculable long-range behavior called the fragmentation function (FF), denoted $D_c^h(z)$, which is defined as the probability for a parton of flavor c to fragment into a hadron taking a fraction $z = p_h/p_c$ of its momentum:

$$d\sigma = \sum_c \int dz d\hat{\sigma}(p_a, p_b, p_c) D_c^h(z) \quad (1.8)$$

This property is known as factorization, and is thought to hold for a wide array of observables, though it has only been explicitly proven for small subset of observables. Experimentally, the yield of hadrons associated with a parton (or jet) of known momentum as function of z , is a measure of the fragmentation function. Since generally p_T , not p is measured experimentally, an alternative variable, $z_T = p_T^h/p_T^{trig}$ is often used, where p_T^{trig} is the transverse moment of a jet, or other object related to a hard scattered parton.

A more complex but relevant observable is the semi-inclusive cross section in Deep Inelastic Scattering (DIS, or SIDIS). This usually refers to an electron colliding with a proton. Semi-inclusive scattering simply indicates that not all the particles are measured. In e+p collisions, semi-inclusive scattering measures at least one other hadron in coincidence with the scattered electron. *Exclusive* scattering, indicates that *all* particles produced in the collision are measured. These definitions appear counter-intuitive, at least in terms of what's measured in the collision. But the distinction comes from the underlying physical processes that each measurement corresponds to. In semi-inclusive scattering, there are several physical processes that could have resulted in the limited number of particles that are measured. For example, there are a variety of processes that give rise to a $q\bar{q}$ pair, all of which must be considered in an event where exactly two jets are measured in coincidence with the scattered electron. In exclusive scattering, because all particles are measured in the collision, the underlying physical process producing those particles is much more readily identified,

to the exclusion of other potential processes. Unlike e+p collisions, in heavy ion collisions the shear number of particles produced, a substantial fraction of which are neutral particles that are notoriously difficult to measure, exclusive measurements are essentially impossible. The term Deep Inelastic is more straightforward; rather than an elastic collision where momentum is conserved, much of the energy goes towards breaking up the proton(Ion). The semi-inclusive DIS cross section can be written as:

$$d\hat{\sigma} = \sum_{a,c} \int dx_a dz f_a(x_a) d\hat{\sigma}(p_a, p_b, p_c) D_c^h(z). \quad (1.9)$$

where (Bjorken) x is the fraction of the proton's momentum carried by the parton, and $f_x(x)$ is the parton distribution function (PDF) that describes the partons in their initial state before the collision. At first glance, this equation is troubling, as it appears that a careful measurement of the hadronic cross section cannot uniquely determine the PDF or fragmentation function. The long-range behavior of these fragmentation functions, however, is thought to be independent of the collision process, a property known as *universality*. Thus, the same fragmentation functions are thought to apply regardless of the particle species being collided. On the other hand, parton distribution function is only a property of the objects being collided and can be factorized from the collision process and subsequent fragmentation.

The cross section for hadro-production in proton-proton collisions can be expressed in a similar way with the addition of a second integral over the additional parton:

$$d\hat{\sigma} = \sum_{a,c} \int dx_a dx_b dz f_a(x_a) f_b(x_b) d\hat{\sigma}(p_a, p_b, p_c) D_c^h(z). \quad (1.10)$$

This gives rise to an interesting picture of progression, albeit a slightly oversimplified one: fragmentation functions are measured in $e^+ + e^-$ collisions, shown in Fig. 1.12, which are then used in DIS data. Then, the DIS data is used to determine the PDF's, shown in Fig. 1.13 which are applied to $p + p$ collisions.

In a similar story of progression, $p+p$ collisions are important baseline data for collisions of heavy nuclei, discussed in Sec. 1.3.4. It turns out, expectations for hadronic observables must be modified in nuclear collisions. Furthermore, $p+Pb$ collisions are important for disentangling cold and hot nuclear matter effects. Such departures provide a window into physics beyond the vacuum behavior of QCD accessed via elementary particles collisions.

1.5 Cold Nuclear Matter Effects

shadowing, kT effect, others....

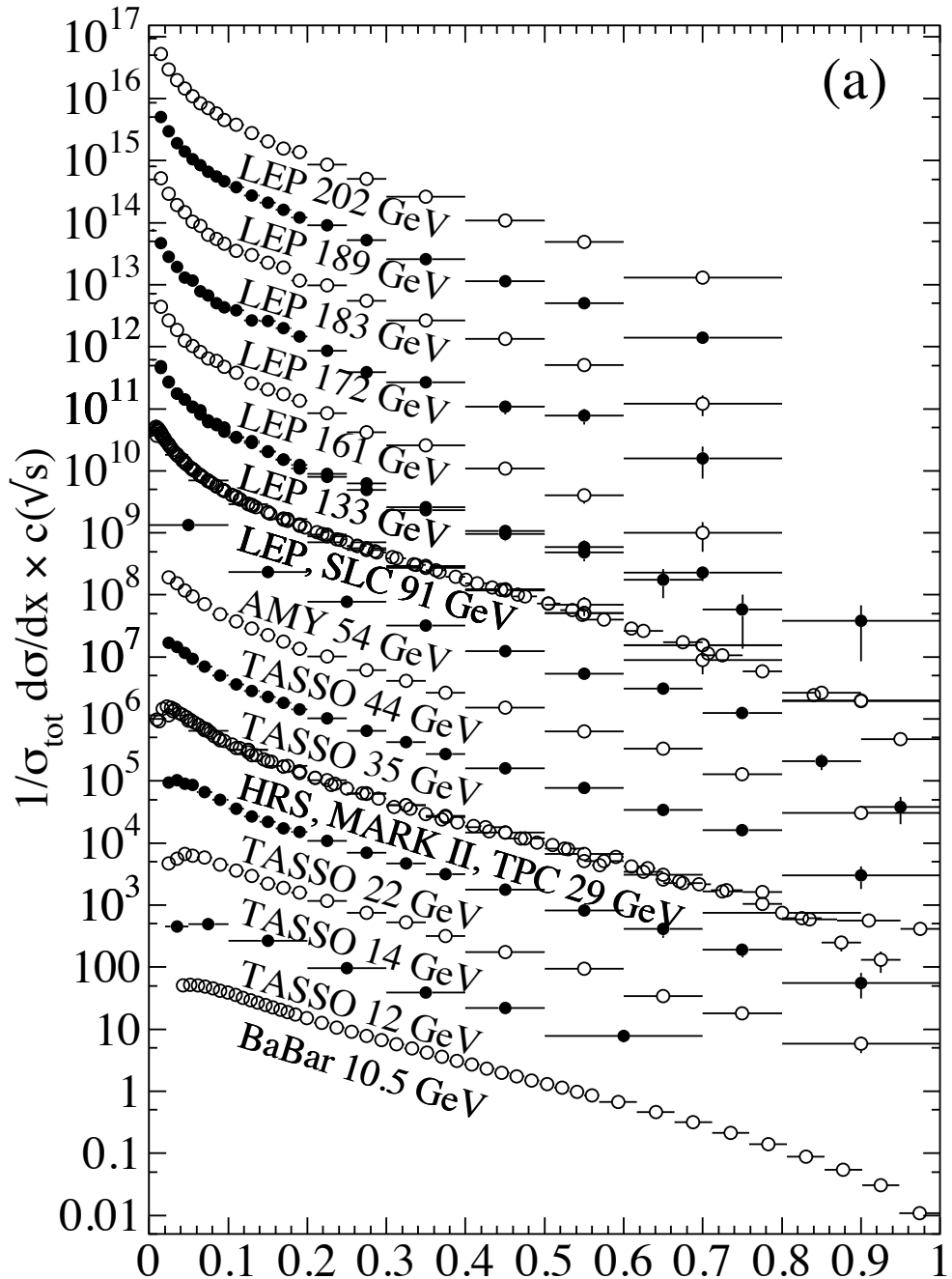


Figure 1.12: The e^+e^- fragmentation function for all charged particles for different CM energies \sqrt{s} versus x . For the purpose of plotting, the distributions were scaled by $c(\sqrt{s}) = 10^i$, where i ranges from $i=0$ ($\sqrt{s} = 12$ GeV) to $i=13$ ($\sqrt{s} = 202$ GeV) [22]

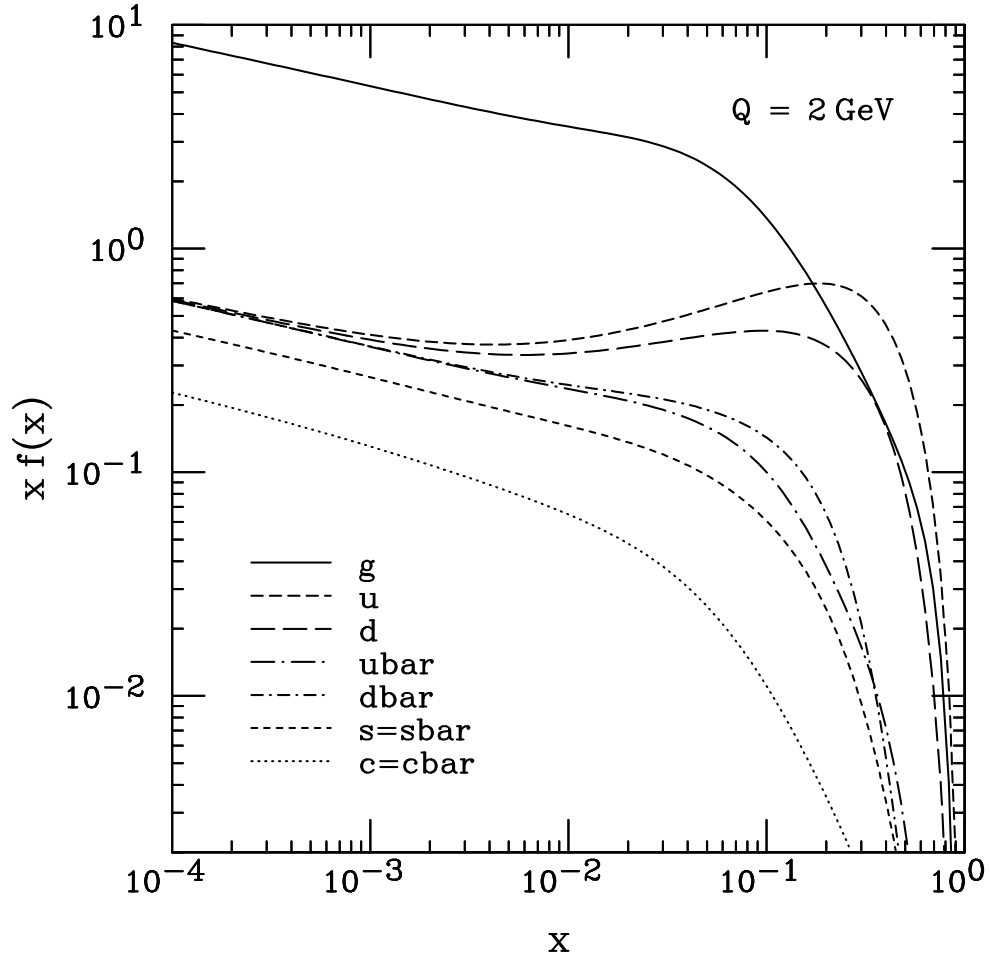


Figure 1.13: Sampling of PDFs from CTEQ [23]

1.6 Two Particle Correlations

Another way to study energy loss effects on partons propagating through a medium in heavy ion collisions is by measuring two particle correlations. One of simplest forms of two particle correlations is the di-hadron correlation. Contemporary jet measurements invoke jet reconstruction algorithms to determine the full energy of the jet event-by-event. These methods are difficult to apply in heavy-ion collisions due to the overwhelming background from soft collisions, and may be less sensitive to medium modification depending on the observable being measured. Instead, a very useful approach has been to measure correlations between particles.

$$Y(\Delta\phi) \equiv \frac{1}{n_{\text{triggers}}} \frac{dN}{d\Delta\phi} \quad (1.11)$$

Fig. ?? shows a simplified example of a di-hadron (hadron-hadron, or h-h) correlation in p+p collisions. The two-peak structure is characteristic of such measurements, and indicates that the event sample is dominated by di-jet events. The particles within the same jet make up the narrow peak centered around $\Delta\phi = 0$ and the recoil jet appears as the peak around $\Delta\phi = \pi$. The away side peak is broadened since kinematically the away side jet can swing along the η direction and k_T , the initial pair momentum of the colliding partons, can create an imbalance in the jets' energy and cause them to be acoplanar. η , also referred to as pseudorapidity, is defined as $\eta = \ln(\tan(\theta/2))$, where θ is the polar angle with respect to beam direction. A 2D plot ($\Delta\phi, \Delta\eta$) of this correlation in pPb and pp collisions is shown in Fig. 1.8, Sec. 1.3.1. The peaks sit atop a pedestal which is due to initial and final state interactions amongst the beam remnants and the hard-scattered partons. This must be subtracted, and will be discussed in greater detail in Sec. 3.4.7 for pp and pPb collisions. For AA collisions, this subtraction is even more complex, where flow is no longer a signal, but a background phenomenon that must be subtracted.

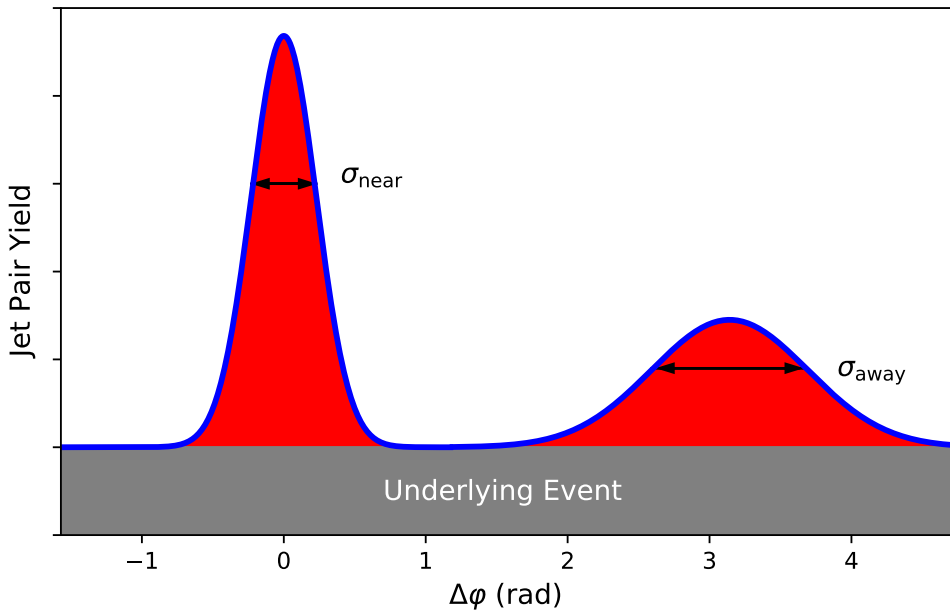


Figure 1.14: Cartoon illustrating a measurement of two-particle correlations from jets

The STAR experiment performed a hadron-hadron correlation measurement with triggers of $p_{T,t} > 4$ GeV/c and partners of 2 GeV/c $< p_{T,a} < p_{T,t}$. The result, shown in Fig. 1.15 demonstrates that for central Au + Au collisions the near-side jet looks very similar to p+p

but the away-side jet completely disappears. This is consistent with a picture in which the near-side jet is usually produced near the surface and the away-side jet is completely absorbed by the medium.

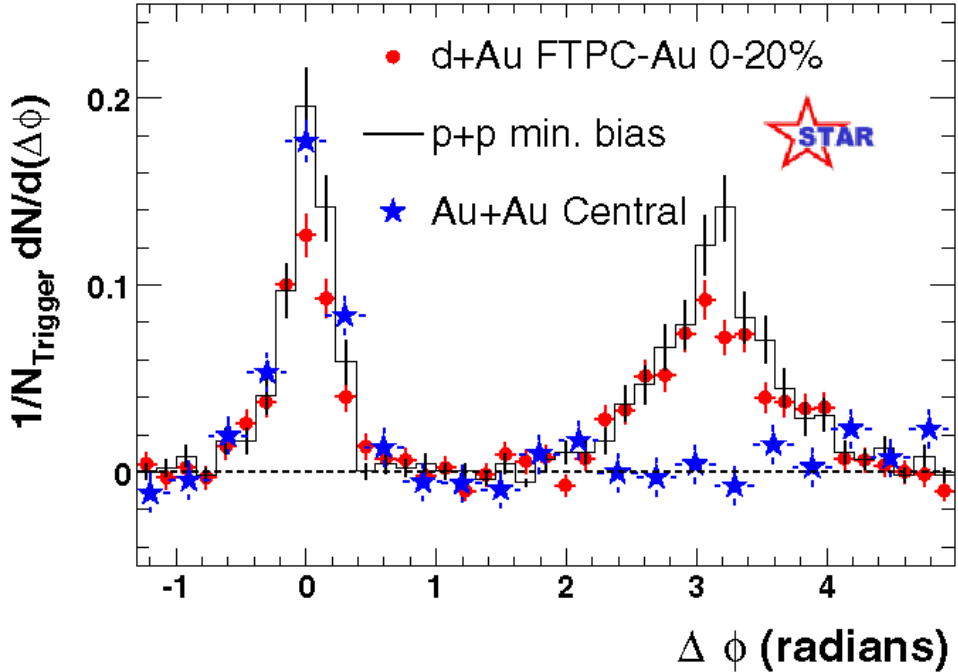


Figure 1.15: Hadron-hadron correlations measured in p+p, d+Au and Au+Au collisions at STAR. The near side jet peaks around $\Delta\phi=0$ in all three systems but the away-side which peaks around $\Delta\phi = \pi$ in p+p and d+Au, is suppressed in Au+Au[24]

Although hadron-hadron correlations have revealed a great deal about energy loss in the medium, they are limited by the fact that the initial parton momentum is unknown and cannot be used to directly measure the fragmentation function.

1.7 Prompt Photons

Prompt photons can be defined simply as the photons produced immediately in the collision, before final state hadrons are produced. At the lowest order in pQCD, prompt photons are produced via two processes: (i) quark-gluon Compton scattering, $qg \rightarrow q\gamma$, (ii) quark-antiquark annihilation, $q\bar{q} \rightarrow g\gamma$, and, with a much smaller contribution, $q\bar{q} \rightarrow \gamma\gamma$. In p+p collisions, the Compton-type process dominates the cross section by roughly an order of magnitude over annihilation as a result of the scarcity of antiquarks. Additionally, prompt photons can be produced in higher-order processes, such as fragmentation or bremsstrahlung

[25]. The collinear part of such processes has been shown to contribute effectively also at lowest order. The basic Feynman diagrams for these processes (excluding $q\bar{q} \rightarrow \gamma\gamma$) are shown in Fig. 1.16.

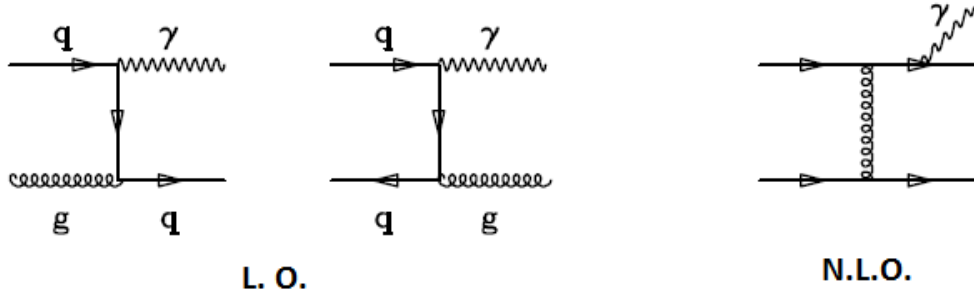


Figure 1.16: On the left are the leading order Feynman diagrams for direct photon production. The diagram on the right is next-to-leading order. Photons resulting from this diagram are referred to as fragmentation photons

Photons produced during fragmentation, are aptly named fragmentation photons. As a result, fragmentation photons are often produced surrounded by a larger amount of energy and hadronic activity than other prompt photons produced from the initial hard scattering.

Prompt photons, and by extension fragmentation photons, are both included in the definition of direct photons. While the definition of direct photons is not always consistent in the literature, and varies slightly between collaborations, we define direct here to mean any photon not produced from hadronic decays. Those photons originating from the decay of a hadronic bound state are defined as decay photons. The two largest sources of decay photons are the two-photon decay channels of the π^0 and η meson. At higher p_T , decay photons make up the majority of photons produced in the collision.

Together, direct and decay photons make up all the photons observed in a collision, called inclusive photons.

$$\gamma_{\text{inclusive}} = \gamma_{\text{direct}} + \gamma_{\text{decay}}$$

1.8 Photons in Heavy Ion Collisions

Direct photons have three very important properties that make them valuable tools in heavy-ion physics. First, There are relatively few leading order diagrams which contribute to direct photon production. Second, The photon-quark coupling is point-like, and not effected by long-range QCD behavior such as fragmentation in the final state. Third, though a property shared with other high- p_T photons, they do not interact with the QGP.

Prompt photons are extremely valuable tools in heavy-ion physics. One property that makes them so useful is that they are not expected to interact with the QGP.

Photons do not carry color charge, and should therefore be unmodified by strong interactions in a medium. While the plasma is made up of quarks that carry (fractional) charge, For example, the mean free path of a 1 GeV photon in a QGP at $T = 200$ MeV was calculated to be $\lambda = 480$ fm, much larger than the estimate size of plasma at $r \approx 10$ fm [26].

Thus, in the leading order picture, after prompt photons are produced early in the collision they should propagate through the medium completely unmodified, with no high p_T suppression. This has been verified, by measuring the R_{AA} of photons, shown in Fig. 1.17.

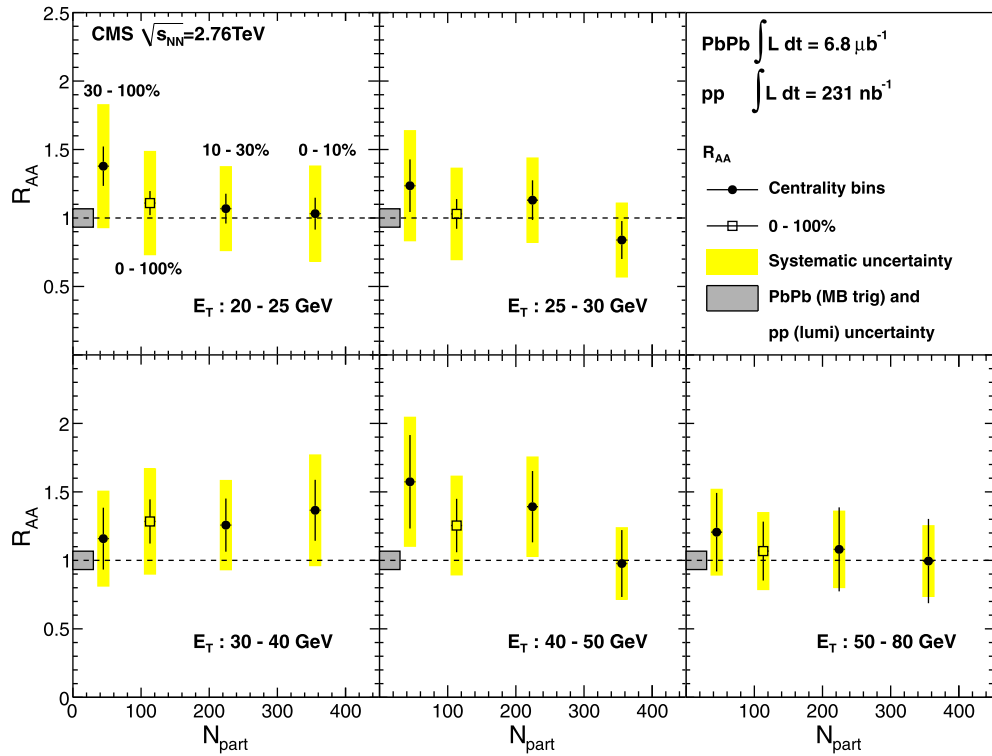


Figure 1.17: The measured nuclear modification factor R_{AA} as a function of PbPb centrality (given by the number of participating nucleons, N_{part}) for five different photon transverse energy (E_T) intervals.

A measured R_{AA} consistent with 1.0 strongly supports the position that photons are unmodified in the quark gluon plasma.

1.8.1 γ -Jet Correlations

Another important property of leading order prompt photons is that the photon-quark coupling is point-like and therefore not complicated by long-range QCD behavior such as jet fragmentation in the final state, in distinction to hadronic observables. Thus, in the leading order picture, the direct photon exactly balances the away-side parton and resulting jet. Here the photon acts as a reference to the parton from the initial scattering, before any modification in heavy-ion collisions. This means that comparisons between the photon and parton, or jet, as well as large deviations from $\Delta\phi \approx \pi$ can be used to directly study medium-induced effects on the recoiling parton. γ -jet correlations in CMS are shown in Fig. 1.18 [27].

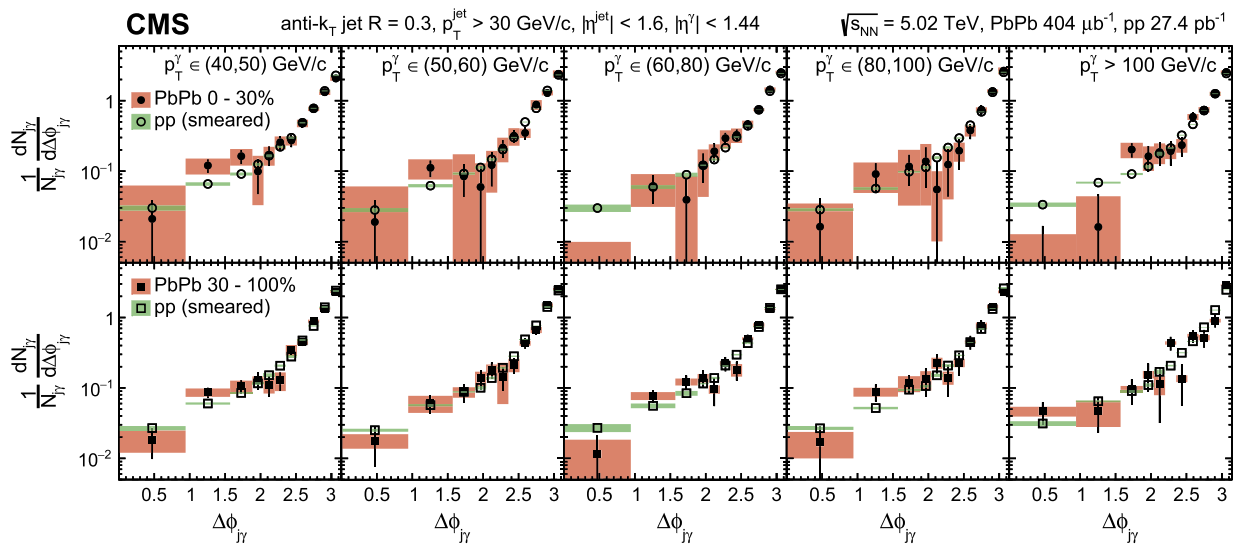


Figure 1.18: The azimuthal correlation of photons and jets in five p_T^γ intervals for 0–30% centrality (top, full circles) and 30–100% centrality (bottom, full squares) PbPb collisions. The smeared pp data (open symbols) are included for comparison. The vertical lines (bands) through the points represent statistical (systematic) uncertainties [27].

In conjunction with γ -jet correlations, the γ -jet asymmetry, $x_{j,\gamma} \equiv p_T^{\text{jet}}/p_T^\gamma$ can be measured to quantify in-medium parton energy loss. Derived from Fig. 1.18, the jet asymmetry for jets with $\Delta\phi > 7\pi/8$ relative to the photon were taken. The asymmetry as a function of photon p_T , as well as the ratio of yields for large $\Delta\phi$, R_{AA} , is shown in Fig. 1.19 [27].

This procedure from CMS also provides a good example of how these correlations are often used to extract other measurements: The angular correlations are measured, from which a region in large $\Delta\phi$ is taken (corresponding to the photon and parton being back-to-back). The yields in this region are then reported as a function of fractional momentum, $x_{j,\gamma}$ in order to measure medium effects.

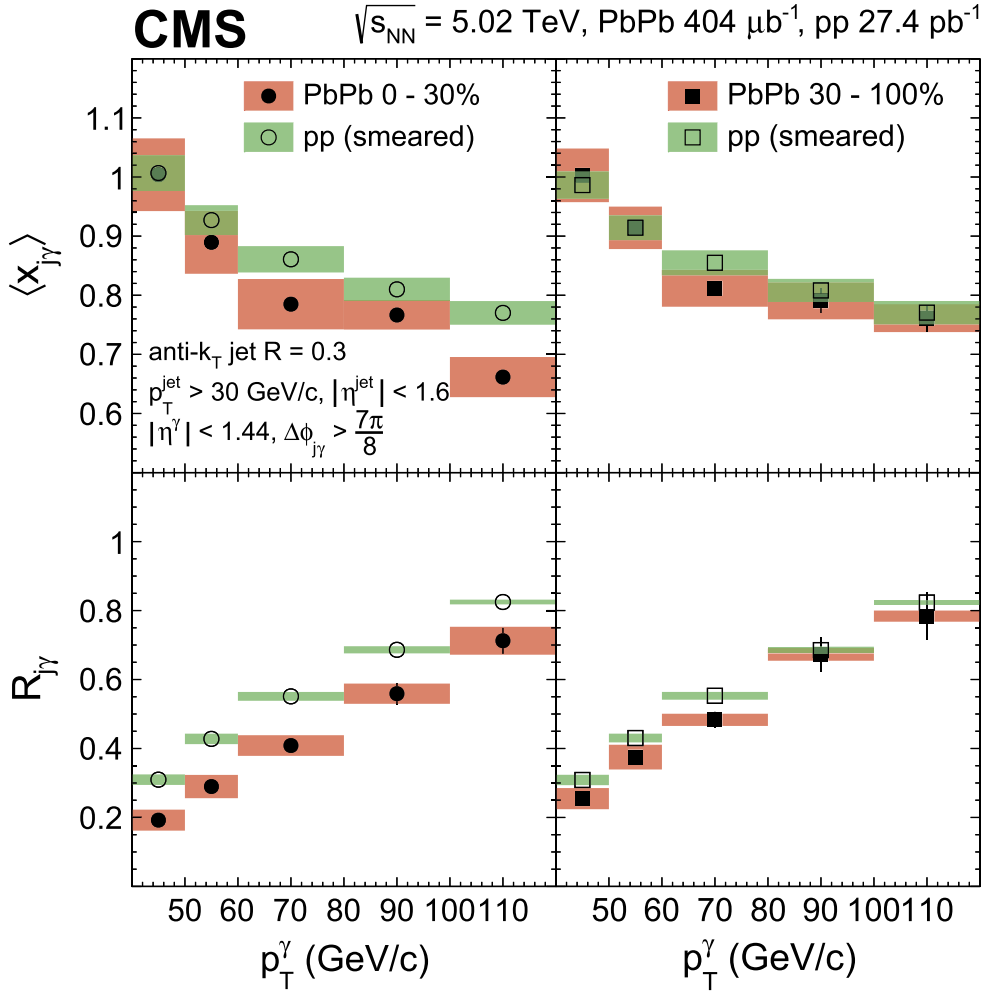


Figure 1.19: The $\langle x_{j,\gamma} \rangle$ values (top) and $R_{j\gamma}$, the number of associated jets per photon (bottom), in 0–30% centrality (left, full circles) and 30–100% centrality (right, full squares) PbPb collisions. The smeared pp data (open symbols) are added for comparison. The vertical lines (bands) through the points represent statistical (systematic) uncertainties.

1.8.2 γ -hadron Correlations

The leading order picture of prompt photons indicates that the photon and recoiling parton have equal and opposite momenta. Therefore, the measurable quantity, $z_T = p_{T,a}/p_{T,t}$ with the prompt photon as the trigger, is nothing but the fragmentation variable, $p_{T,hadron}/p_{T,parton}$. This explains why prompt γ -h correlations are such a powerful measurement. They provide a source of recoil partons of fixed momentum and their conditional yields as a function of z_T in p+p collisions probe the parton fragmentation. By contrast, dihadron correlations are controlled by the jet cross section which also depend on the PDF's and the parton scattering cross sections.

When the hadrons roughly opposite the trigger photon are reconstructed as a jet, they are clearly connected to the recoiling parton from the initial scattering in the leading order picture. The hadrons within those jets can then be used to probe the jet fragmentation function. γ -hadron correlations in which a jet is not reconstructed, however, have a distinct advantage over γ -jet correlations: hadrons are more sensitive to in-medium modification. Fig. 1.11 shows a minimum in R_{AA} for charged hadrons at approximately 6GeV, and a plateau begins after 20 GeV/c. It is extremely difficult to measure jets below around 20 GeV/c in heavy ion collisions due to the large background [28]. Selecting jets at higher p_T (or jets with kinematics similar to that in 'vacuum', or pp collisions), to avoid this background biases the jet population towards jets that will lose the least energy in vacuum, as discussed in Sec. /refsec:raa. Additionally, triggering on a high $p_{T,hadron}$ as a proxy for a jet can bias the measurement towards jets towards the surface of the medium [29]. Similar to R_{AA} , the ratio of the conditional yields for γ -h and γ -jet correlations in pp and AA collisions can help quantify medium induced modifications to the parton, in this case, the fragmentation function. Fig. 1.20 shows the direct¹ photon-hadron correlations measured with the PHENIX detector as a function of $\xi \equiv \ln(1/z_T)$:

Similar to the γ -jet measurement in the previous section, the conditional yield at higher $\Delta\phi$ is measured. This conditional yield as a function of ξ is the experimentally measured fragmentation function. The ratio of this yield in pp and AA collisions, $I_{AA} \equiv Y_{AA}/Y_{pp}$, is a nuclear modification factor which quantifies the difference between the fragmentation functions in AA and p+p collisions. This is shown in Fig. 1.21 [30].

γ -hadron correlations are an incredibly powerful tool: they provide an observable that probes the parton fragmentation function with objects in the collision (low to intermediate $p_{T,hadrons}$) that are particularly sensitive to medium modifications. Measuring γ -hadron correlations in both pp and PbPb collisions is an important step in elucidating the modifications to the parton fragmentation function due to QGP. However, a full understanding of these phenomena requires measurements of cold nuclear matter (CNM) effects, which should be present in Au+Au collisions but are difficult to distinguish experimentally from effects due to interactions with the medium.

¹Direct is used in lieu of prompt at RHIC due to the smaller contribution of fragmentation photons at the lower center of mass energies compared to LHC.

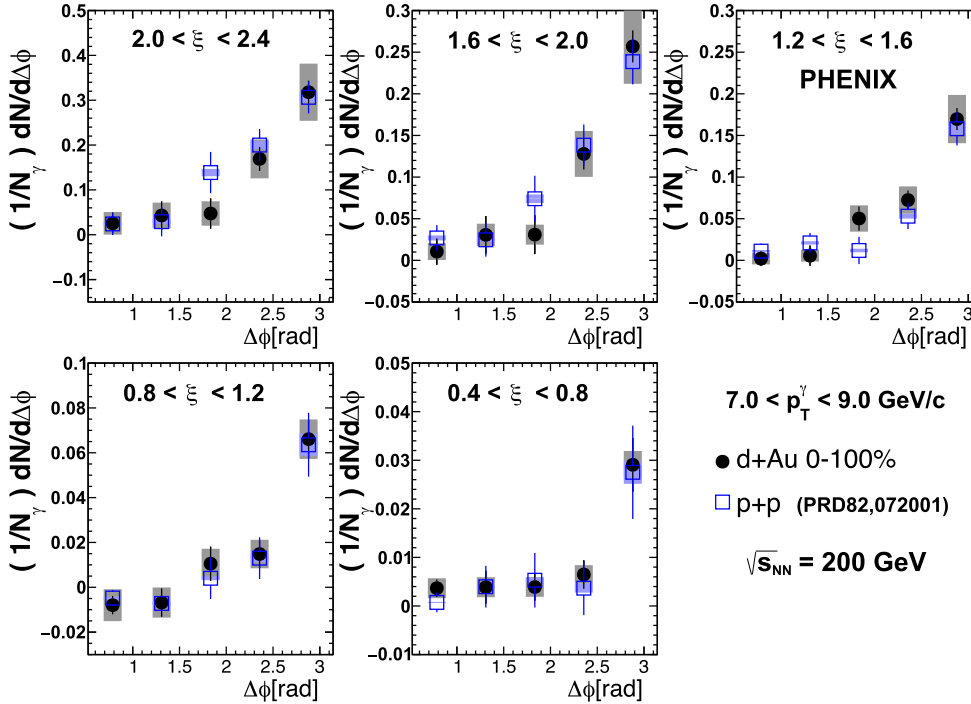


Figure 1.20: Per-trigger yield of hadrons associated with direct photons in Au+Au collisions (closed [black] circles) for direct photon p_T 5–9 GeV/c, compared with p+p baseline (open [blue] squares), in various ξ bins.

1.9 cold nuclear Matter Effects

In order to quantitatively study the properties of the QGP, it is necessary to separate effects which are due to interactions with the medium from those which are intrinsic to interactions of cold nuclei. The p + p baseline measurements used to calculate the nuclear modification factor RAA can not account for these nuclear effects, since none are present in free protons. For example, ^{208}Pb contains 126 neutrons, so the majority of nucleon-nucleon collisions in PbPb events will involve neutrons. Any isospin dependant effects would be impossible to model in pp collisions.

1.9.1 The Nuclear Parton Distribution Function

The production cross sections for prompt photons and hadrons should be sensitive to the distribution of quarks gluons inside the nucleus, detailed by the nuclear parton distribution function (nPDF). The relation of the bound-proton PDFs with respect to free-proton PDFs f_i^p is often expressed in terms of a nuclear modification factor in the form of:

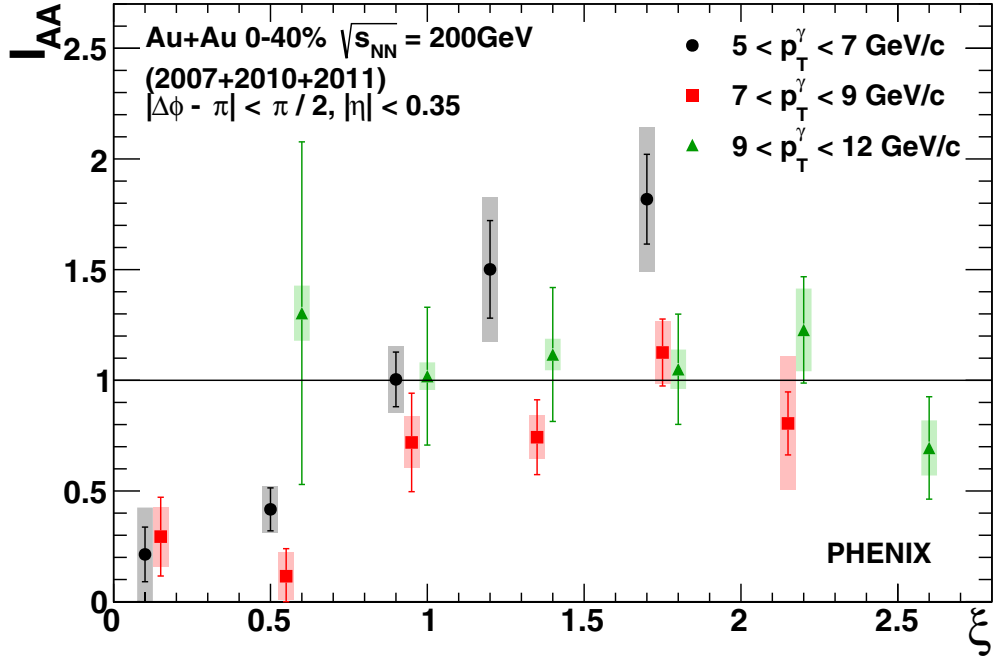


Figure 1.21: I_{AA} for three direct photon p_T^γ bins.

$$R_i^A(x, Q^2) = \frac{f_i^p/A(x, Q^2)}{f_i^p(x, Q^2)} \quad (1.12)$$

A typical form of such modifications is shown in the left panel of Fig. 1.22.

The modification in the region where the ratio is less than 1.0 is called "shadowing" at very low x , and the "EMC" effect at $0.3 < x < 0.7$. The region where the modification is larger than 1.0 is called "anti-shadowing". The exact magnitude of these effects on various measurements, as well as an improved understanding of the nPDF's is a current goal in the field. Recently, a major step forward toward this goal has been the inclusion of LHC pPb data, particularly for extracting the gluon-PDF.

1.9.2 Nuclei and Fragmentation

Aside from differences between the PDFs in free and bound nucleons, there are potential observable effects of the nucleus as a medium itself. Measurements in p+A collisions showed that particle production at moderate transverse momentum increases faster than the number of binary nucleon-nucleon collisions [32]. This was attributed to the Cronin effect where the scattered parton undergoes multiple scatterings in the nucleus, resulting in a transverse momentum boost, *before* the interaction that ultimately produces the final state particle.

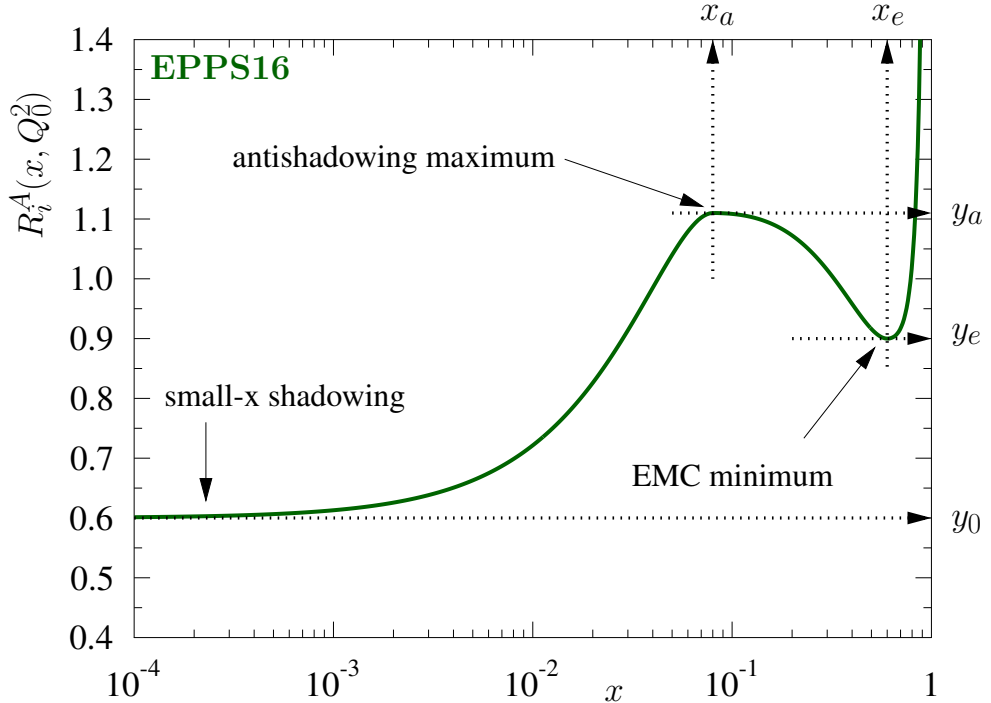


Figure 1.22: Typical form of PDF modifications in a nucleus[31].

Currently, however, an open question in the field is the exact timescale of fragmentation, as both pQCD and lattice calculations are unable to provide estimates. This leaves open the possibility that the parton begins to fragment while still inside the nucleus, potentially modifying the fragmentation process and the final state hadrons of the resulting jet.

The current state on cold nuclear matter effects modifying the parton fragmentation function is ambiguous: In di-hadron and direct photon-hadron correlations, no significant modification of the jet fragmentation was observed in measurements by the PHENIX collaboration in d–Au collisions at a center-of-mass energy of 200 GeV [33] and the ALICE collaboration in p–Pb collisions at 5.02 TeV [34, 35] at mid rapidity. At forward rapidity, a strong-modification was observed by the PHENIX collaboration in d–Au collisions [36]. A recent measurement by the PHENIX collaboration with pp, p–Al, and p–Au data revealed a transverse momentum broadening consistent with a path-length dependent effect [37]. However, a recent ATLAS measurement of the jet fragmentation function in p–Pb collisions showed no evidence for modification of jet fragmentation for jets with $45 < p_T < 206$ GeV/ c [38]. Measurements of the fragmentation of jets with much lower momentum are necessary to limit the Lorentz boost to the timescales of fragmentation, as such a boost may result in fragmentation outside the nucleus. These measurements would test the Q^2

evolution of fragmentation functions in cold nuclear matter, testing factorization theorems that are neither proven nor expected to hold in general for collisions involving nuclei [39].

1.10 Statement of Purpose

Parton fragmentation may be modified in the nucleus, offering a way to explore the dynamics of QCD in nuclei including elastic, inelastic, and coherent multiple scattering of partons. Moreover, the known spatial dimensions of nuclei provide a filter possibly shedding light on the timescale of the fragmentation process, which remains unknown [40, 41]. Additionally, because photons produced in hard scatterings do not strongly interact, they constrain the parton kinematics from the same scattering before any modification. Thus, measurements of photon-tagged jet fragmentation in pA collisions serve as a powerful tool to study multiple-scattering effects in cold nuclear matter [42], which serve as a control for effects of the quark–gluon plasma (QGP) in nucleus–nucleus collisions, where modifications of the jet spectrum, fragmentation, and substructure have been observed [43].

In this work, azimuthal correlations of charged hadrons with isolated photons, γ^{iso} , are analyzed in p–Pb and pp collisions with a center-of-mass energy of $\sqrt{s_{\text{NN}}} = 5.02$ TeV. Isolated photons are measured at midrapidity, $|\eta| < 0.67$, and with transverse momenta in the range $12 < p_T < 40$ GeV/ c , which yields the scaling variable $x_T = 2p_T/\sqrt{s_{\text{NN}}} = 0.005\text{--}0.016$. The kinematic range probed in this analysis offers access to a lower Q^2 than other LHC experiments, which is where the largest nuclear effects can be expected, and to a similar x_T range as RHIC measurements at forward rapidity [36].

Understanding the dynamics of quarks and gluons in nucleons and nuclei is a key goal of modern nuclear physics. Proton–nucleus (pA) collisions at high energies provide information about the parton structure of nuclei, parton–nucleus interactions, and parton fragmentation in a nuclear medium [40]. The energy of the Large Hadron Collider (LHC) available for pA collisions is a factor of 25 larger than at the Relativistic Heavy Ion Collider (RHIC), and thus it provides unprecedented reach in longitudinal momentum fraction Bjorken- x and Q^2 [44].

Chapter 2

Experimental Apparatus

Chapter 3

Data Anaysis

3.1 Isolated Prompt Photons Selection

A key challenge of this measurement is the relatively small cross section of prompt photons compared to decay photons. In order to reduce the background of decay photons, and to identify prompt photons, a combination of isolation and electromagnetic shower profile selections are made.

3.1.1 Shower Profile Selection

The primary background for this measurement are photons from the 2-body decay channel of neutral mesons π^0 's. A π^0 with a higher p_T will decay with a smaller opening angle between the two decay photons. As the opening angle becomes smaller, the electromagnetic showers from the decay photons get closer together in the EMCAL until they begin to overlap. For this reason, photons from π^0 decays begin to merge into a single cluster in the EMCAL above approximately 6 GeV/c. This cluster, made up of two showers from decay photons, will therefore tend to have a more elongated shower profile than a cluster resulting from a single, ideally prompt, photon. Thus, in order to reject clusters produced by two photons from a meson decay, and select clusters from single photons, we select clusters using variables that encode the shape of the calorimeter shower.

A variable that encodes the shape of a cluster's electromagnetic shower profile for this purpose is σ_{long}^2 . The σ_{long}^2 variable is the weighted root-mean-square of the shower energy along the major ellipse axis, and thus clusters with a symmetric shower profile will trend towards smaller values of σ_{long}^2 . σ_{long}^2 is defined according to Ref. [45] as:

$$\sigma_{\text{long}}^2 = \frac{s_{\eta\eta} + s_{\phi\varphi}}{2} + \sqrt{\frac{(s_{\eta\eta} - s_{\phi\varphi})^2}{4} + s_{\eta\varphi}^2}, \quad (3.1)$$

where $s_{ij} = \langle ij \rangle - \langle i \rangle \langle j \rangle$ are the covariance matrix elements; the i, j are cell indices in η and φ axes; $\langle ij \rangle$ and $\langle i \rangle, \langle j \rangle$ are the second and the first moments of the cluster position cell

weighted as follows:

$$\text{weight} = \max(\log(E_{\text{cell}}/E_{\text{cluster}}), w_0). \quad (3.2)$$

Following previous studies [46], we chose the cutoff in the log-weighting as $w_0 = -4.5$, which means that cells that contain less than $e^{-4.5} = 1.1\%$ of the total cluster energy are not considered in the σ_{long}^2 calculation.

Fig. 3.1 shows an example of a cluster with an elongated shower profile with a large σ_{long}^2 , and a narrow, symmetric cluster with a smaller σ_{long}^2 .

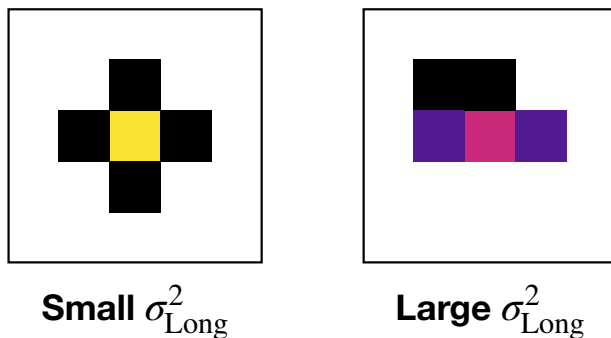


Figure 3.1: Cartoon of a narrow EM shower profile with a small σ_{long}^2 (left), and an elongated shower profile with a larger σ_{long}^2 .

The shower shape profile is an important tool to help discriminate between clusters belonging to single photons, for which the σ_{long}^2 distribution is narrow and symmetric, and merged photons from neutral-meson decays, for which the distribution is dominated by a long tail towards higher values. This analysis uses a cutoff of $\sigma_{\text{long}}^2 < 0.3$ to identify single photon candidates, which will be discussed in Sec. 3.2.

3.1.2 Photon Isolation Requirement

At leading order in pQCD, prompt photons are produced in $2 \rightarrow 2$ processes surrounded by very little hadronic activity, in contrast to fragmentation photons and high $p_T\pi^0$'s found within a jet. Beyond leading order, the direct and fragmentation components cannot be factorized. As a result, the sum of their cross sections becomes the physical observable.

Despite this, the contribution from fragmentation photons can be suppressed by enforcing an isolation criteria, where the energy surrounding a photon must be less than a certain threshold. Theoretical calculations can also be simplified through the use of an isolation requirement. [47]. This also has the benefit of suppressing the background from decays of neutral mesons often found within jets.

The simplest definition of isolation is defined as the scalar sum of the transverse momentum of charged particles within an angular radius, $R = \sqrt{(\Delta\varphi)^2 + (\Delta\eta)^2}$, around the

cluster direction. This measurement uses $R = 0.4$, which is a common value used in various jet measurements.

$$p_T^{\text{iso,raw}} = \sum_{\text{track } \in \Delta R < 0.4} p_T^{\text{track}} \quad (3.3)$$

This does not, however, take into account the energy arising from the underlying event, described in the following section.

3.1.3 Underlying Event Estimation for Photon Isolation

The underlying event (UE) is defined as the sum of all processes that make up the final hadronic state in a collision, excluding the leading order hard scattering. When the two nuclei, lorentz contracted into discs tiny fraction of a femtometer thick, overlap or collide, a small fraction of the incident partons suffer hard perturbative interactions as the discs overlap initially. Most of the incident partons, however, lose some energy but are not deflected by any large angle. Most of these interactions are soft and involve little transverse momentum transfer. In the language of fields and particles, as the two discs of strongly interacting transverse color fields and associated color charges collide, some color charge exchange occurs between the discs, and longitudinal color fields are produced, which fill the space between the two receding discs, reducing the energy in the discs themselves, and then gradually decay into $q\bar{q}$ pairs and gluons. These processes can be labelled as multi-parton interactions, as well as both initial and final state radiation, but the term underlying event also includes measured beam fragments. Essentially, the underlying event is made up of all the particles not directly associated with the initial hard scattering of the collision.

Here we describe the method used to estimate the underlying event for the purposes of correcting the isolation requirement (not to be confused with the later section 3.4.7, where the contribution from the underlying event to the azimuthal correlation measurement is described).

We use the jet area/median method¹ which estimates the underlying event energy density, ρ , from the median of the distribution of the transverse momentum densities of the jets in the event [48]. Jets are reconstructed by running the k_T reconstruction algorithm over all charged particles in the event, using a resolution parameter of $R = 0.3$. The k_T algorithm is used here in place of the more standard anti- k_T as it groups particles with the lowest momentum first to construct the jet. This makes the k_T algorithm more sensitive to the softer objects in the event, and therefore more suitable for studying the underlying event. The transverse momentum density of each jet is simply the momentum of the jet divided by its area, determined by the sum of the voronoi cells of each particle within the jet². This median

¹From the FASTJET software package::VoronoiAreaSpec http://www.fastjet.fr/repo/doxygen-2.4.5/classfastjet_1_1VoronoiAreaSpec.html

²The voronoi cell is the region for each "seed", or particle, that consists of all points in the same plane that are closer to that seed than to any other.

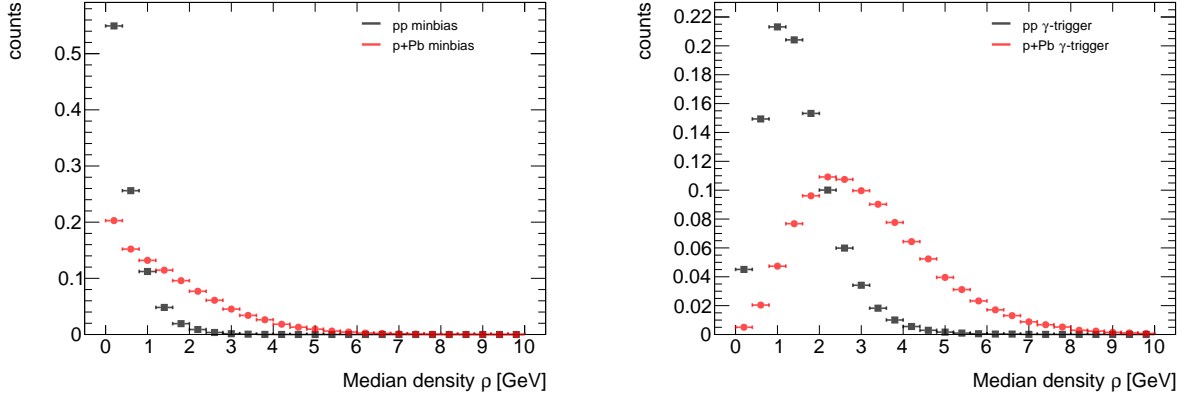


Figure 3.2: Distribution of the median charged-particle transverse momentum density, ρ , in pp and p–Pb data, for a minimum-bias selection (left panel) and in photon-triggered events (right panel).

calculation is described in Equation 3.4:

$$\rho = \text{med} \left\{ \frac{\sum_{i \in J'_k} p_{T,i}}{\sum_{i \in J'_k} A_i} \right\} \quad (3.4)$$

where $p_{T,i}$ is the transverse momentum, and A_i the Voronoi area of the particle i within the jet, J'_k , reconstructed for UE estimation purpose. The median is determined from all jets in the event with the important exception of the two leading (highest moment) jets in the event, as those are most often associated with the hard scattering of the collision. This therefore assumes that most of the charged particles in the event is made up of soft particles, and that the charged particles originating from the hard scattering of the collisions are reasonably contained within the leading jets of the event [48].

The charged-particle density, ρ , is calculated for each event. Figure 3.1.3 shows the distribution of ρ for minimum bias and gamma-triggered events in pp and p–Pb. Average values are 3.2 GeV/c in photon-triggered events in p–Pb and 1.6 GeV/c in pp collisions, demonstrating the a larger underlying event activity in p–Pb compared to pp.

The mean and standard deviation for each distribution is shown in Table 3.1. The difference in UE-density in p–Pb is expected due to the increased number of nucleon-nucleon collisions. The UE-densities shown here are still about a factor of 50 lower than in central Pb-Pb collisions.

Table 3.1: Median transverse momentum density mean and standard deviation in minimum-bias and photon-triggered events in pp and p–Pb data, calculated with negligible statistical uncertainties.

	pp minbias	pp γ -trigger	p–Pb minbias	p–Pb γ -trigger
$\langle \rho \rangle$	0.49 GeV/c	1.51 GeV/c	1.56 GeV/c	3.19 GeV/c
σ_ρ	0.47 GeV/c	0.85 GeV/c	1.32 GeV/c	1.60 GeV/c

3.1.4 UE Correction to Isolation Variable

For each cluster in the event, the underlying event is subtracted using the measured charged-particle density ρ that is calculated event-by-event as described in Section 3.1.3:

The result is an average subtraction for the isolation cone of $R = 0.4$ is about 1.6 GeV/c and 0.8 GeV/c for p–Pb and pp collisions, with a standard deviation of 0.9 GeV/c and 0.4 GeV/c, respectively.

For photons near the edge of the detector, the isolation energy requirement is scaled to account for any missing area in the isolation cone³. A check on this scaling procedure was also done in Section 5.2.4.

$$p_T^{\text{iso}} = p_T^{\text{iso,raw}} - \rho \times \pi(0.4)^2. \quad (3.5)$$

Figure 3.3 shows the isolation distribution before and after underlying event subtraction for p–Pb and pp collisions. The distributions have a positive tail that decreases exponentially. This is likely due to the sensitivity of the isolation variable on multi-jet production cross section. The difference between the p–Pb and pp distribution at low p_T^{iso} values can be attributed to the effect of enhanced soft-particle production in p–Pb collisions, i.e. a larger underlying event due to the presence of the pPb nucleus. The underlying event subtraction modifies the isolation distribution only slightly at high p_T . At low and negative p_T , however, the distributions show a negative tail after subtraction, which arises from an over-subtraction of the underlying event. This occurs due to region-to-region fluctuations in the underlying event, where a cluster contains an energy density that is smaller than the median calculated according to Section 3.1.3. In both cases, this tail falls by more than three orders of magnitude by $p_T^{\text{iso}} = -3$ GeV/c, indicating that over-subtraction is a small effect.

The left panel of Figure 3.4 shows the distribution of cluster isolation after UE subtraction for photon-jet and dijet simulations of p–Pb data (see Table ??). The distributions exhibit different behavior: whereas the dijet simulation shows a prominent exponential tail at large p_T^{iso} values, the photon-jet simulation shows a more Gaussian-like shape that is mostly symmetric with the exception of a very small fraction of events that have large p_T^{iso} values. In both cases, however, the negative tail falls rather sharply, as it arises from region-to-region fluctuations of the UE that are independent of the hard-process involved.

³The final isolated photon-hadron correlations are normalized to the number of reconstructed photons. As a result, the γ^{iso} efficiency was not studied in detail.

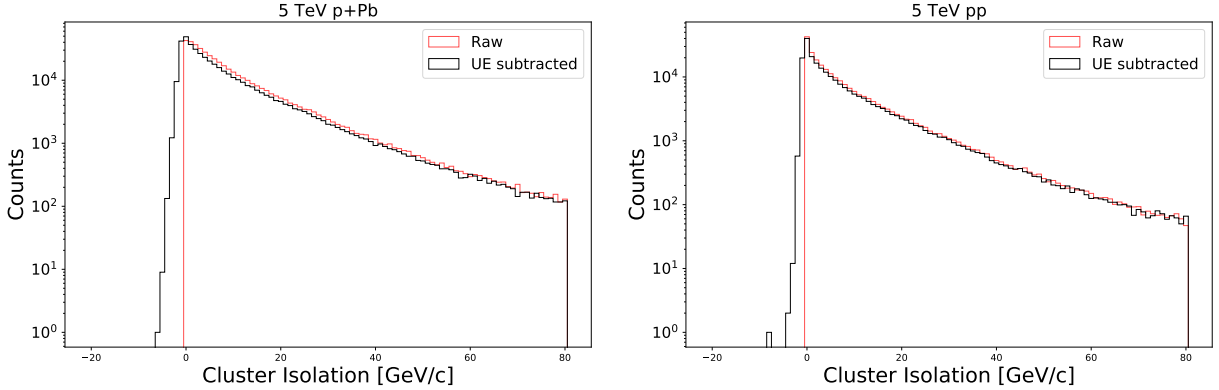


Figure 3.3: Cluster isolation before and after underlying event subtraction in p–Pb (left panel) and pp (right panel) collisions.

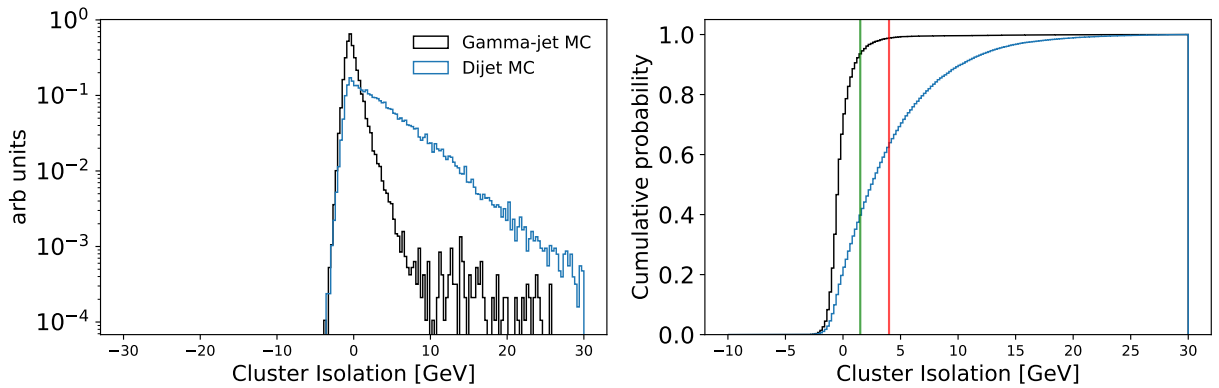
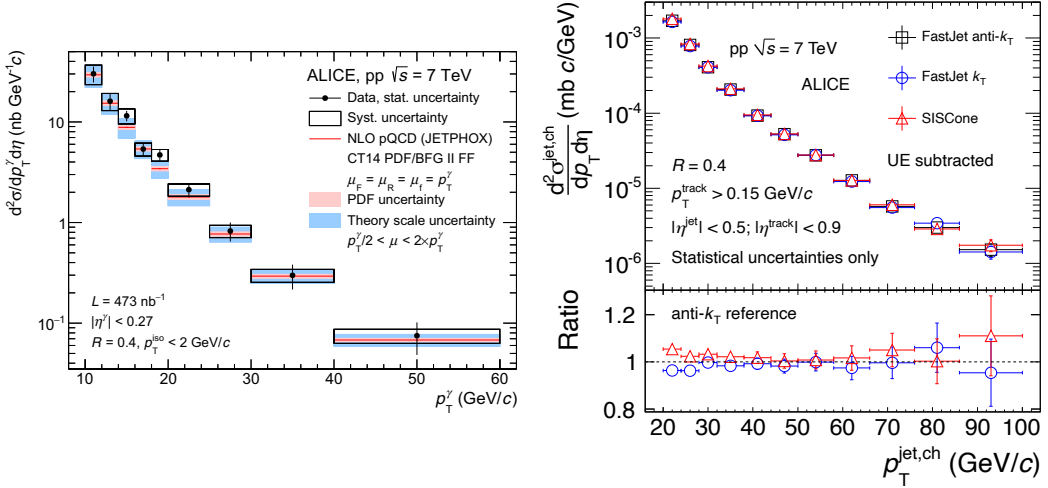


Figure 3.4: Isolation distribution of clusters that pass our selection in p–Pb photon-jet and dijet simulations, and corresponding cumulative distribution. Two vertical lines at $p_T^{\text{iso}} = 1.5$ GeV/ c (green) and $p_T^{\text{iso}} = 5.0$ GeV/ c are shown in the right panel for reference.

The cumulative distributions (Figure 3.4, right panel) show that a $p_T^{\text{iso}} < 1.5$ GeV/ c selection keeps about 90% of the signal and rejects about 60% of the background. We use this relatively loose photon isolation criteria to reduce the dependence of the results on the details of the simulation of the detector noise, tracking resolution, and the underlying event.

3.1.5 Remaining Background after Photon Selection

This isolation cut of $p_T^{\text{iso}} < 1.5$ GeV/ c is used in conjunction with the shower-shape cut to complete the isolated-photon selection or “ γ^{iso} selection”. The population of clusters



that pass this selection are labelled “ γ^{iso} -candidates” (rather than simply ”prompt photons”) because there is still a significant fraction of remaining background. Some other sources of background not yet mentioned arise from charged-to-neutral fluctuations of jet fragmentation that leads to low observable p_T^{iso} (that considers only charged-particles). However, the main background present in the γ^{iso} selection arise from multi-jet events where one jet typically contains a π^0 or η which carries most of the jet energy, and is therefore surrounded by relatively less energy within the jet. The pair is also frequently misidentified as a single photon because it decays into a pair of photons that are collinear with respect to the EMCal cell granularity. The first indication of this is shown in Figure 3.4, where approximately 40% of the dijet cross section (expressed as a cumulative probability as a function of cluster isolation, shown in blue) is within $p_T^{\text{iso}} < 1.5 \text{ GeV}/c$.

Distributions of background and signal as function of σ_{long}^2 are shown later in 3.2

Figure 3.1.5 expands on this. The left panel shows the isolated photon differential cross section as a function of $p_T^{\gamma^{\text{iso}}}$ in proton-proton collisions at $\sqrt{s} = 5.02 \text{ TeV}$ measured by the ALICE detector. The right panel of Figure shows the differential cross section of charged jets as a function of p_T^{jet} . The cross section for an isolated photon at $p_T = 20 \text{ GeV}/c$ is roughly $2 \text{ nb GeV}/c^{-1}$. In contrast, the cross section for charged jets at $p_T = 20 \text{ GeV}/c$ is roughly $2 \times 10^{-3} \text{ mb GeV}/c^{-1}$, approximately three orders of magnitude larger.

Of course, jets containing a neutral meson with a large fraction of its total momentum make up only a fraction of the total jet cross section, and recoil partons produced from the same hard scattering as prompt photons will contribute to the total charged jet cross section. But the stark difference between the isolated photon and charged jet cross sections speaks to the rarity of isolated photons in these collisions and the abundance of background and illustrates the need to measure the purity of our γ^{iso} -candidate selection.

3.2 Purity

The isolation and shower shape selections remove the bulk of the neutral meson decay background, but a substantial fraction of the γ^{iso} candidates are still background photons. It is therefore necessary to quantify the ratio of true signal photons in our candidate sample in order properly subtract it. The estimate of the ratio of true signal photons in our γ^{iso} sample is called the *purity*.⁴

3.2.1 The Template Fit Method

The purity of the isolated photon sample is determined with a two-component template fit, a method used by the CMS collaboration in Ref. [49]. The distribution of the shower shape variable for the isolated cluster sample is fit to a linear combination of a signal distribution and the background distribution. The shape of the signal distribution is determined by a photon-jet simulation (see Table ??) and the shape of the background distribution is determined from data using an anti-isolated sideband⁵ with an additional correction computed from a dijet simulation. This is described in more detail in the following sections.

3.2.2 Signal Template and Background Templates

The shape of the background distribution of the shower-shape for isolated clusters is estimated with a *sideband* technique: the shower shape distribution of clusters from isolated decay photons is estimated with clusters that are anti-isolated but pass all other selection criteria. This method assumes that the correlation between the isolation variable and shower shape variable can be corrected for; the procedure for doing so is described below. The signal and sideband regions defined using the isolation variable are illustrated in Figure 3.5.

For simplicity, the same definitions are used for pp and p–Pb data. The lower bound of the sideband region is defined as $\text{ISO} = 5 \text{ GeV}/c$; according to photon-jet simulations, less than 1% of prompt photons are beyond this range. The upper bound is chosen such that the sideband is as narrow as possible, to minimize a possible bias to the shower-shape distribution due to a positive correlation with ISO, while still containing a number of clusters comparable to the signal region. A more rigorous study on the sensitivity of our purity estimate on the choice of sideband region is shown in Section ??.

Figure 3.6 summarizes the signal and background templates used in the template fit. The distributions are quite different, which is key for the stability of the template fit. The background shape in the σ_{long}^2 variable shows a peak in the single-shower region but a “bump” that reflects a π^0 peak. In both cases, the peaks in the single-shower region that are observed in the background templates come mostly from collinear $\pi^0 \rightarrow \gamma\gamma$ decays.

⁴For a more rigorous discussion of the Purity calculation, please see Alwina Liu’s UC Berkeley Thesis.

⁵The inversion of an isolation cut to estimate QCD background is a standard technique in several measurements at the LHC and previous hadron colliders.

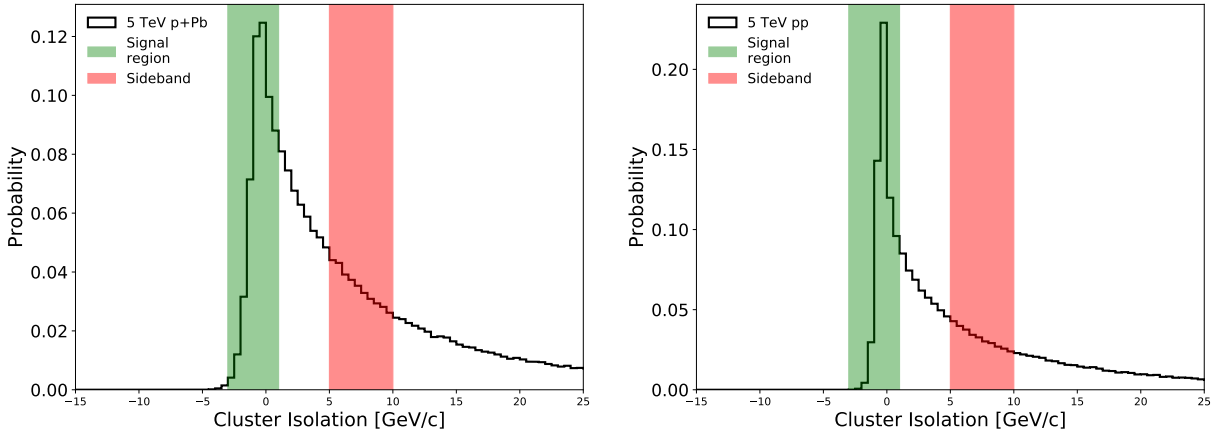


Figure 3.5: Isolation variable distribution of clusters with p_T between 12 and 16 GeV/ c in p–Pb data (left panel) and pp data (right panel). The green shaded area represents the signal region ($\text{ISO} < 1.5 \text{ GeV}/c$); the red represent the sideband ($5 < \text{ISO} < 10 \text{ GeV}/c$) used to estimate the background template.

The background template is corrected for the correlation between the shower shape variable and the isolation energy of the cluster. A dijet simulation is used to construct the ratio of the shower shape distribution for isolated clusters to the shower shape distribution for anti-isolated clusters. This ratio, calculated as a function of the shower shape variable, is then applied as a weight to the anti-isolated clusters in the data, giving a corrected background template that is then used in the template fit. From Equ. 3.6), it is clear that if the monte-carlo exactly replicates the data, the Weights function will exactly correct the anti-isolated decay photon σ_{long}^2 distribution back to the isolated decay photon σ_{long}^2 distribution, which is the true background.

$$\text{Weights}(\sigma_{\text{long}}^2) = \frac{\text{Iso}_{\text{MC}}(\sigma_{\text{long}}^2)}{\text{Anti-iso}_{\text{MC}}(\sigma_{\text{long}}^2)}$$

$$\text{Bkg}^{\text{corrected}}(\sigma_{\text{long}}^2) = \text{Non-iso}_{\text{data}}(\sigma_{\text{long}}^2) \times \text{Weights}(\sigma_{\text{long}}^2) \quad (3.6)$$

The purity computed with the corrected background template is 8–13% (absolute) lower in compared to the purity computed with the uncorrected background template; an example of a fit with and without the correction is shown in Figure 3.7. The correction greatly improves the fit. The $\text{Weights}(\sigma_{\text{long}}^2)$ function for different p_T ranges is shown in Appendix ?? and the evaluation of the systematic uncertainty associated with this correction is described in Section ??.

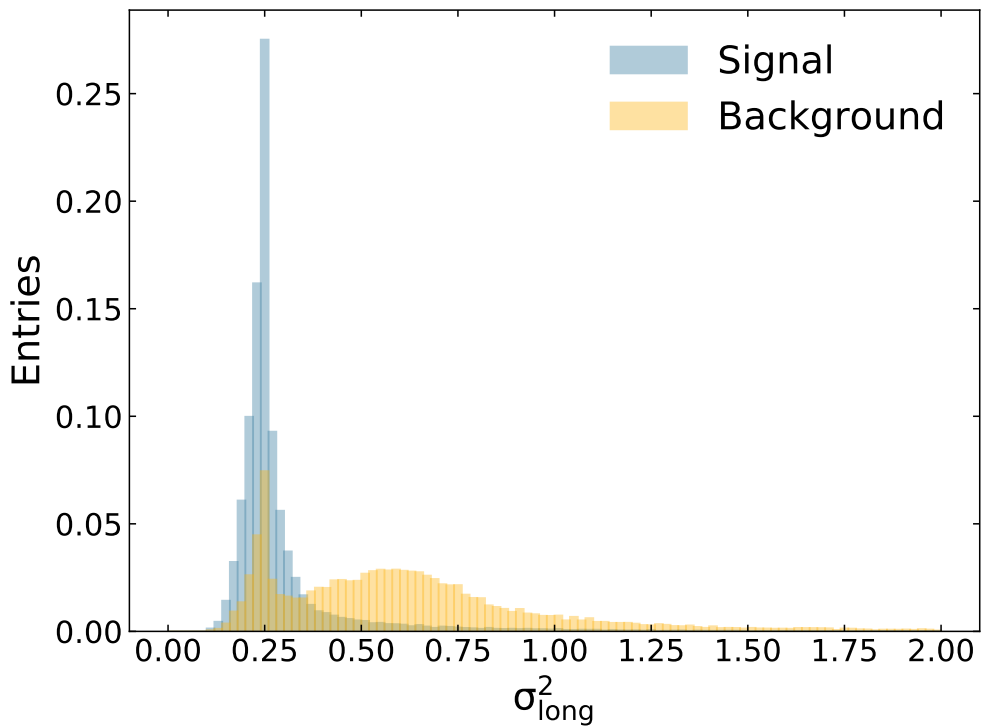


Figure 3.6: Normalized signal (blue) and background (yellow) distributions used as input for the template fit. These distributions correspond to clusters with p_T in the 15–20 GeV/ c range.

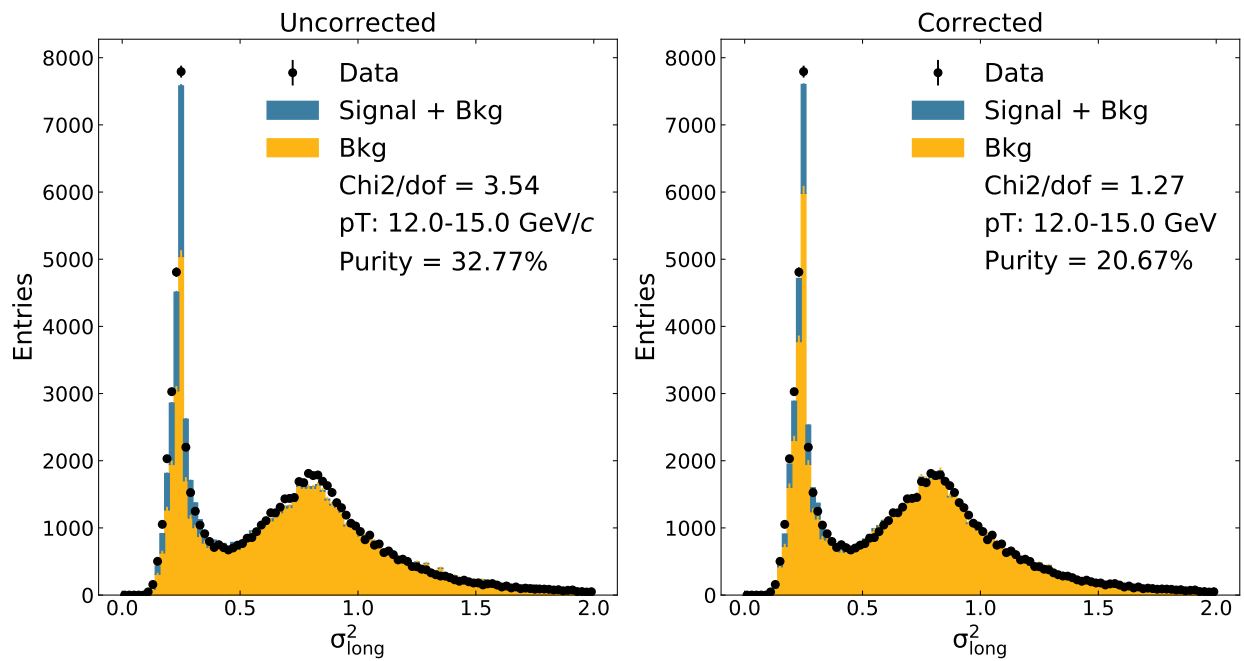


Figure 3.7: An example of the template fit with and without the background template correction in p–Pb for clusters with $12 < p_{\text{T}} < 15 \text{ GeV}/c$. The goodness of fit is better after the correction and the purity is significantly lower.

3.2.2.1 Fit results

The distribution of isolated clusters is fit with a linear combination of the signal and background templates. We use the MINUIT [50] package for χ^2 minimization and the MIGRAD package for error estimation. The only free parameter in the fit is the number of signal clusters, N_{sig} , because the overall normalization, N , is fixed to the total number of isolated clusters:

$$N^{\text{observed}} = N_{\text{sig}} \times S + (N - N_{\text{sig}}) \times B, \quad (3.7)$$

where S and B are the normalized signal template and background template.

Figures 3.8 show template fit results for p–Pb and pp data. In all cases a good fit with no obvious systematic pattern in the residuals is achieved over most of the distribution, and the reduced χ^2 ranges are within acceptable values. The purity measurements are presented in graphical form in Figure 3.9.

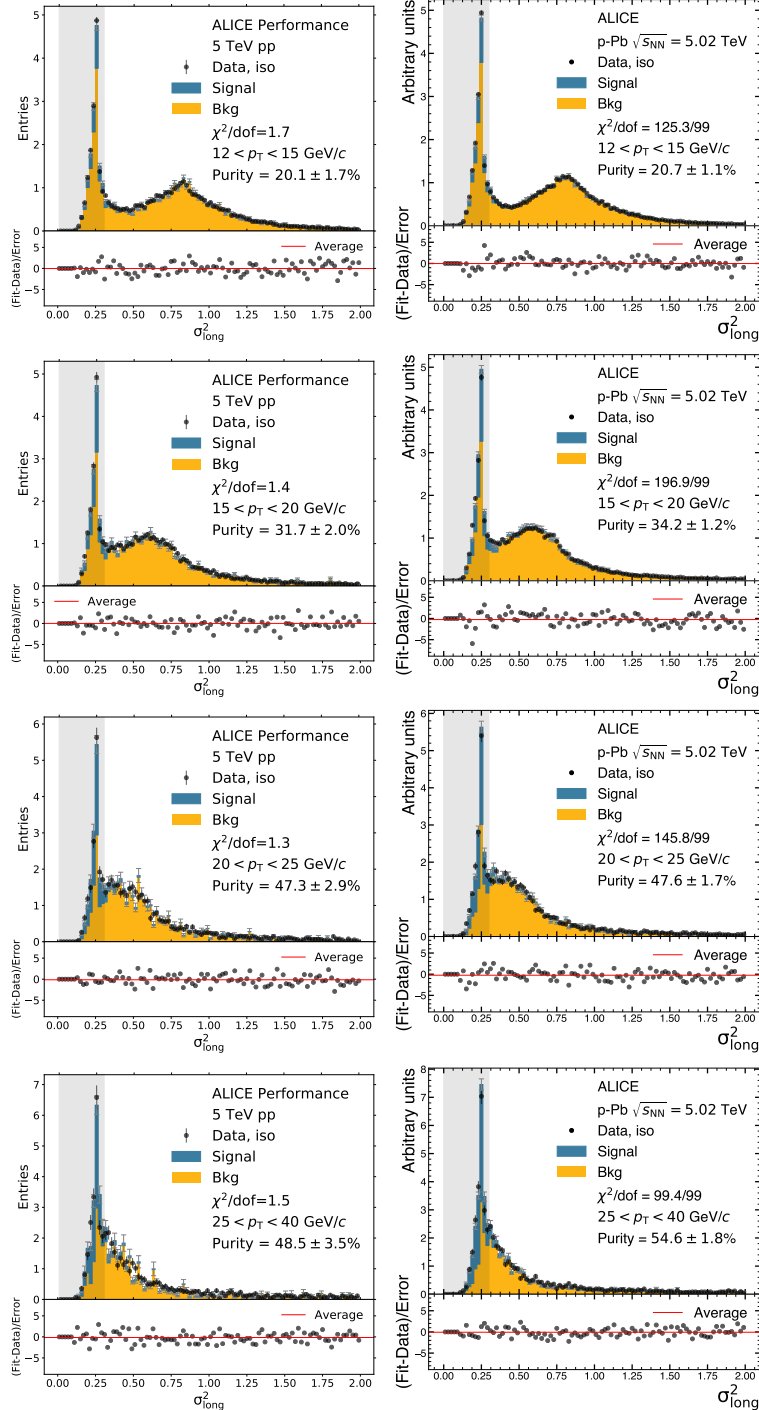


Figure 3.8: Template fit results in pp and p–Pb data. The stacked histograms (yellow for background, blue for signal) are the predicted counts given the best-fit value of the number of signal photons, N_{sig} . The hatched gray area represents the interval considered for the purity estimate. The bottom panels show the normalized residuals of the fit, considering the statistical uncertainty on the isolated cluster data and the background template added in quadrature.

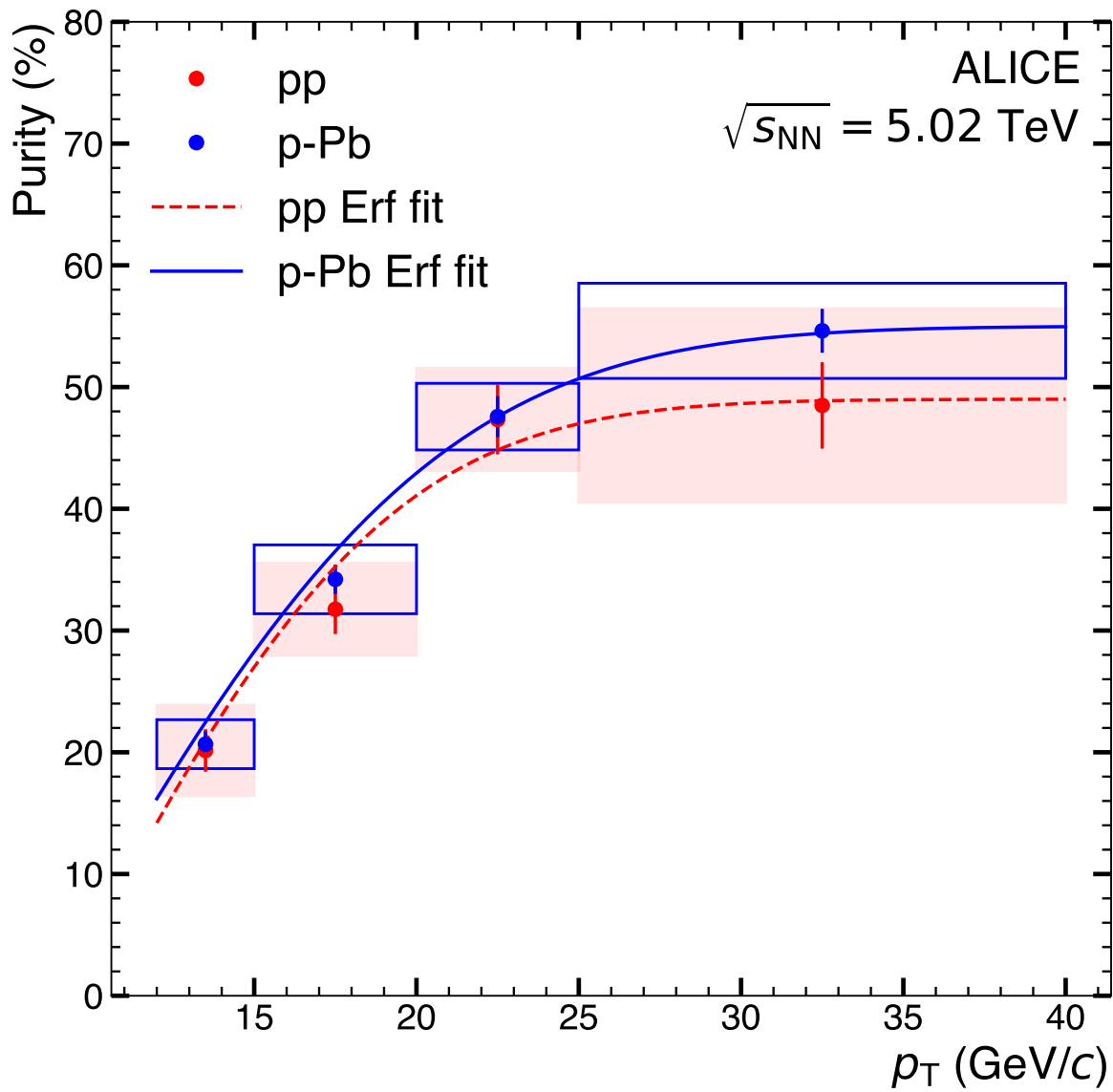


Figure 3.9: Purity of isolated-photon selection as a function of cluster p_T . The error bar represents statistical uncertainty while the error band represents the systematic uncertainty.

3.3 Charged Particle Tracking

The detectors usually responsible for measuring the charged hadrons in this analysis are the ALICE Inner Tracking System (ITS) and Time Projecton Chamber (TPC). During the 13def and 17q periods, however, the TPC was either not read out or compromised due to space-charge distortions. As a result, this analysis relies on only the ITS for track reconstruction.

ITS-only tracking in ALICE is new for this flavor of analysis. As a result, the charged-particle p_T -spectrum using ITS-only tracking is compared to the normal TPC+ITS tracking in the data-taking period when the TPC was active and free of space-charge distortions (the low-luminosity 13b data-taking period at 5 TeV p–Pb minimum-bias data) as well as with published ALICE measurements [51] that use the same dataset (a more thorough comparison to published ALICE data is done in Sec. 5.3.1).

The combined effect of tracking efficiency, fake rate, and track momentum smearing corrections are calculated using MC simulations, and validated by the comparison to the established hybrid-tracking method in ALICE. The comparison to hybrid tracking also serves as an estimate of the systematic uncertainties due to mis-modeling of the tracking performance.

To study the performance of ITS-only tracking, minimum bias p–Pb events for both data and Monte Carlo. The Monte Carlo simulations used for this section are LHC13b2_efix_p1, a DPMJET simulation anchored to LHC13b,c and LHC17l3b, a pp PYTHIA8 simulation anchored to LHC17p. The events are sampled from the LHC13b period and the datasets from [51], as mentioned previously. Only events with the minimum bias trigger (CINT7) that also the vertex and pileup selections described in Section ???. The tracks reconstructed from the ITS (“ITS-only tracks”), are compared with tracks reconstructed from information obtained from both the TPC and ITS (“TPC+ITS tracks”, or “hybrid” tracking). Here, ITS-only tracks are reconstructed in a *stand-alone* way and are not simply the ITS-segment of a ITS+TPC track.

In order to select good-quality tracks emerging from the primary vertex while maintaining a high efficiency, each track is required to satisfy the cuts summarized in Table 3.2. A set of standard PWG-JE cuts are applied to all tracks, and additional track cuts are applied depending on whether the track is a TPC+ITS track or an ITS-only track.

Table 3.2: Summary of the cuts used in Track Selection.

Common Cuts	
track η	$ \eta < 0.8$
track p_T	$p_T \geq 0.150 \text{ GeV}/c$
SetMaxDCAToVertexXY	2.4 cm
SetMaxDCAToVertexZ	3.2 cm
SetDCAToVertex2D	TRUE
TPC+ITS Cuts	
SetMinNClustersTPCPtDep	70.+30./20.*x, 20.0
SetMinNClustersTPC	70
SetMaxChi2PerClusterTPC	4
SetMaxChi2PerClusterITS	36
SetMaxFractionSharedTPCCClusters	0.4
SetMaxChi2TPCCConstrainedGlobal	36
SetRequireTPCStandAlone	TRUE
SetRequireTPCRefit	TRUE
SetRequireITSRefit	TRUE
SetRequireSigmaToVertex	FALSE
SetAcceptKinkDaughters	FALSE
ITS-Only Cuts	
SetRequireITSPureStandAlone	TRUE
SetMinNClustersITS	4
SetMaxChi2PerClusterITS	36

3.3.1 Efficiency and Fake Rate

The tracking efficiency is calculated as the ratio of the number of reconstructed primary particles⁶, $N_{\text{prim,rec}}(p_T)$, to the number of generated primary particles, $N_{\text{prim,gen}}$. The truth-to-reconstructed matching is done following the standard ALICE method.

$$\epsilon(p_T^{\text{true}}) = \frac{N_{\text{prim,rec}}(p_T^{\text{true}})}{N_{\text{prim,gen}}(p_T^{\text{true}})}. \quad (3.8)$$

Shown in Eq. 3.8, the simulated or "truth" transverse momentum, p_T^{true} , is used in both the numerator and denominator in order cancel effects of efficiency from bin-migration due to momentum smearing.

The numerator of Equation 3.8 is restricted for charged particles with generated pseudorapidity in the range $|\eta^{\text{true}}| < 0.8$ and azimuth $0 < \varphi^{\text{true}} < 2\pi$. Therefore, the correction factor accounts for both geometrical acceptance, detector inefficiencies, and dead channels.

⁶No special tuning of the particle type composition is performed. This typically only matters at low p_T and enforces a small (percent level) correction to the out-of-the-box results.

Fake tracks are defined as reconstructed tracks that do not match to a truth particle. The fake rate is calculated by taking the ratio of the number of fake tracks to the total number reconstructed tracks. It is parametrized as a function of the reconstructed transverse momentum of the track, p_T^{reco} :

$$\text{fakerate}(p_T^{\text{reco}}) = \frac{N_{\text{unmatched}}(p_T^{\text{reco}})}{N_{\text{allreco}}(p_T^{\text{reco}})}. \quad (3.9)$$

Figure 3.10 shows the efficiency and the fake rates for the TPC+ITS and ITS only tracks. In both cases the efficiency grows with p_T up to about 1 GeV/c where it dips and it reaches a plateau value with no significant p_T dependence. The efficiency starts at about 57% for the TPC+ITS tracks and at 70% for ITS-only tracks at 150 MeV and plateaus at 84% and 88% respectively.

The lower efficiency for the TPC+ITS tracks compared to ITS-only tracks is expected since the former requires a matching between ITS and TPC track segments, which has some inefficiency. This study shows that the matching efficiency is high at large p_T but leads to substantial differences at low p_T .

The fake rate for the TPC+ITS tracks is less than a percent over the entire range shown. In comparison, the fake rate is larger in the ITS-only tracks. It is below 5% up to 5 GeV/c, and it grows roughly linearly and reaches 15% at 10 GeV/c. The higher fake rate is due to the much lower number of clusters associated with ITS-only tracks (maximum of 6) than to TPC+ITS tracks (minimum of 70).

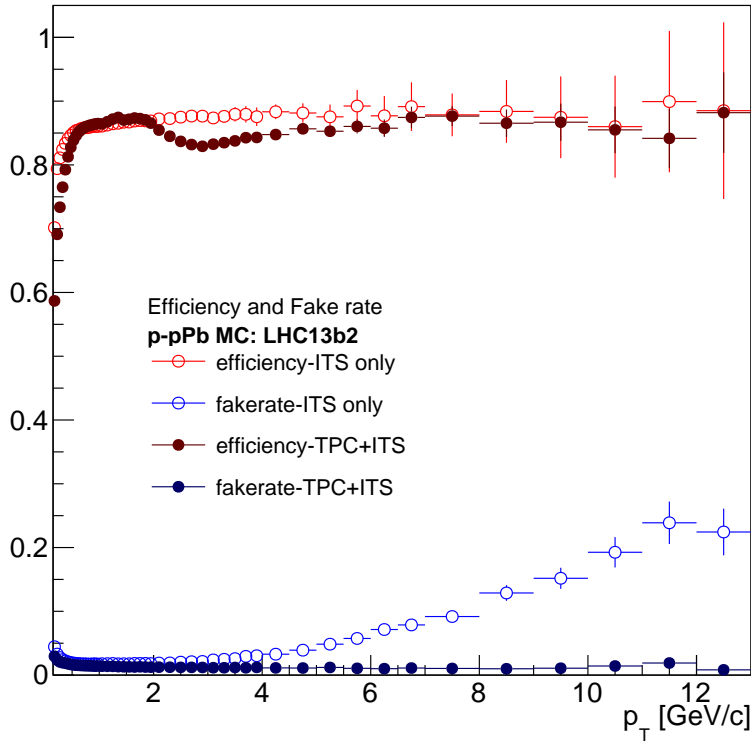


Figure 3.10: Efficiency and fake rate for combined TPC+ITS tracking (filled circles) and ITS-only tracking (open circles) obtained with p -Pb simulation. The error bars represent statistical uncertainty only.

3.3.2 Resolution, response matrix and bin migration

The main difference between TPC+ITS and ITS-only tracking lies in the much worse momentum resolution of the latter. This is driven by geometry and $\int B dl$ as the TPC covers up to $z = 258$ cm but the ITS only to $z = 48$ cm.

Figure 3.11 shows the momentum resolution as a function of p_T^{true} for TPC+ITS and ITS-only tracks. The momentum resolution of both increases with p_T ; however, the resolution for TPC+ITS never exceeds a relative 2% below 20 GeV/c, while the ITS-only tracking resolution is about a factor of 7 worse and reaches $\sim 15\%$ by 10 GeV/c. In both cases the resolution curves have the expected shape: the growth at low momentum is due to multiple-scattering and the linear growth at higher p_T arises from the number and depth of position measurements, and the track bend at the measurement planes.

The tracking response matrix is defined as the correlation between the reconstructed and generated transverse momentum. This matrix is filled only for reconstructed tracks with a

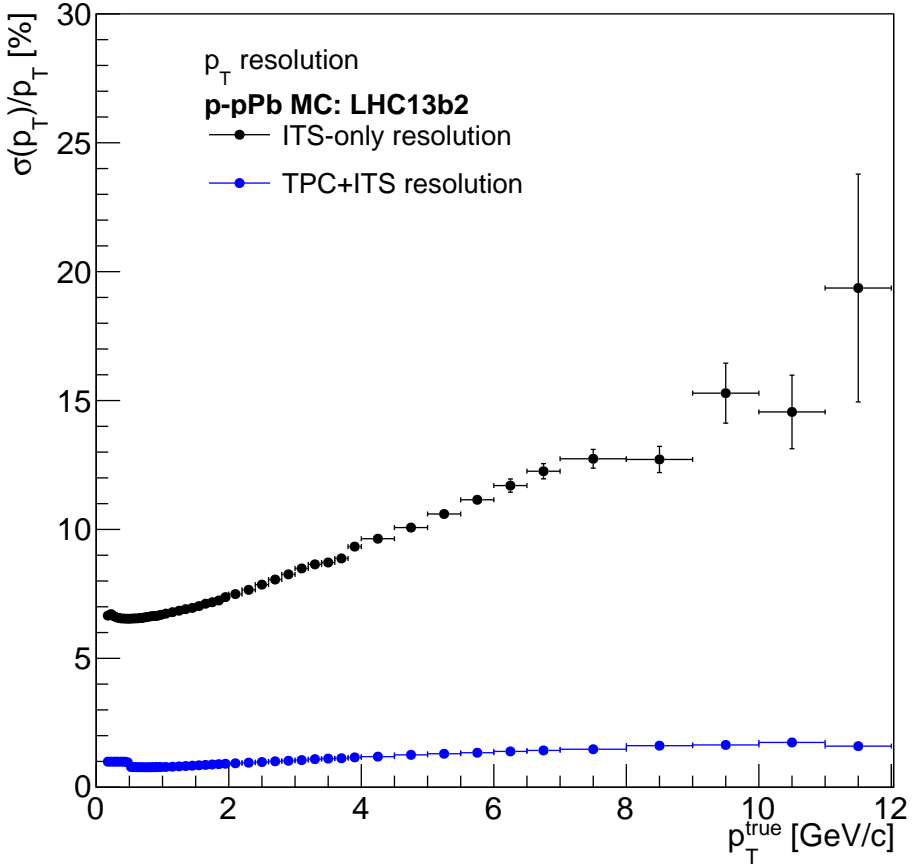


Figure 3.11: The relative p_T resolution for TPC+ITS tracking and ITS only tracking. The error bar represents statistical uncertainty only.

true match; fake tracks are explicitly excluded. Figure 3.12 shows the response matrix, its one-dimensional projections, and the ratio of true to reconstructed spectra. The ratio of the true to reconstructed spectra is used to correct for bin migration effects, where a track is placed in the wrong p_T bin due to the finite momentum resolution of the detector:

$$\text{bin migration}(p_T^{\text{reco}}) = \frac{N_{\text{prim},\text{reco}}(p_T^{\text{true}})}{N_{\text{prim},\text{reco}}(p_T^{\text{reco}})}. \quad (3.10)$$

The effect of momentum smearing on tracks is clearly visible in the projection plots, where the reconstructed spectrum is significantly harder at high p_T . The ratio of truth to reconstructed p_T is very close to unity in the TPC+ITS case, as expected. On the other hand, the ratio deviates significantly from unity in the ITS-only case; it reaches 0.9 at 6

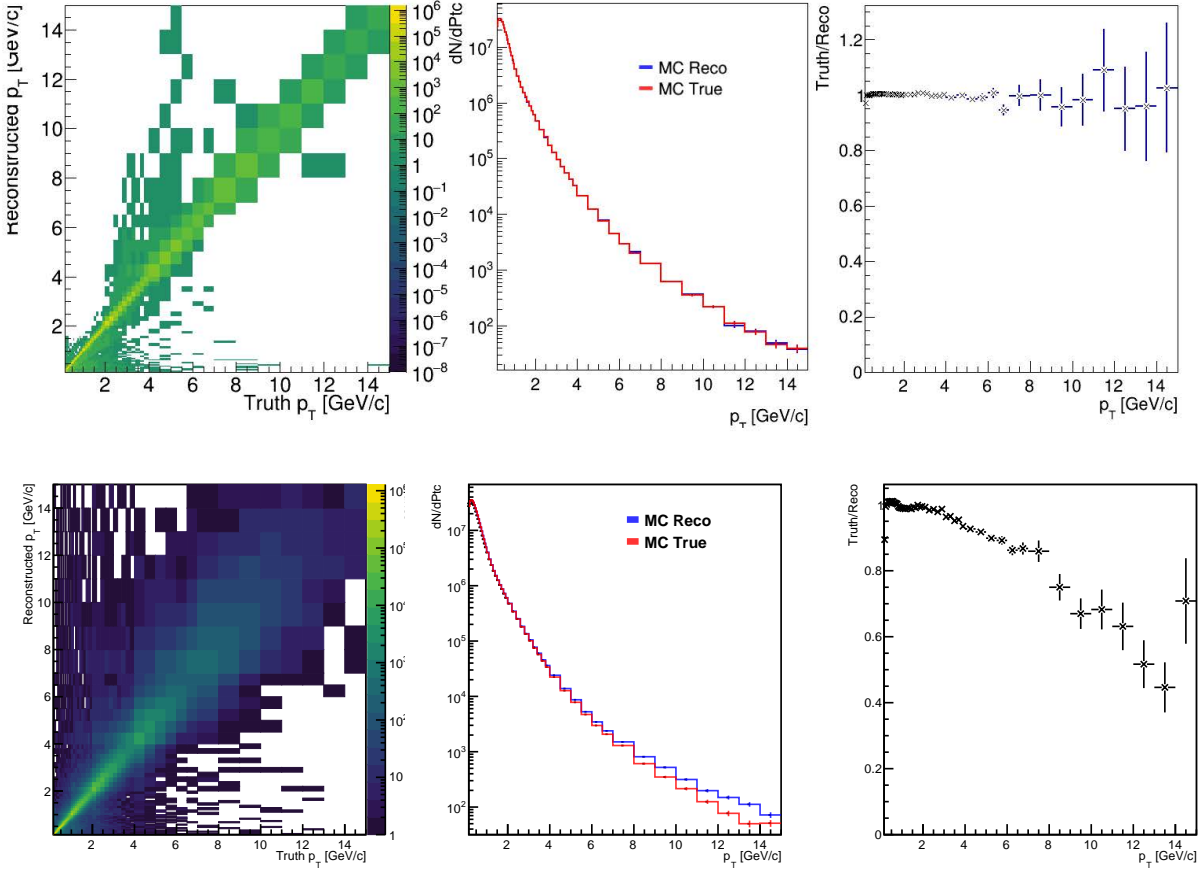


Figure 3.12: Left panel: correlation matrix between true p_T and reconstructed p_T of tracks reconstructed with TPC+ITS (upper row) and ITS-only (bottom row). Middle panel: projections of the response matrix into the true and reconstructed p_T . Right panel: ratio of true to reconstructed spectra. This ratio used as part of the bin-by-bin correction factors.

GeV/ c and drops quickly, reaching 0.5 at about 13 GeV/ c . The quick drop at high p_T comes mainly from the linear degradation of the relative momentum resolution combined with the fast drop of the true spectrum to produce large effects in the tails.

The bin migration (b), along with the tracking efficiency (ϵ) and the fake rate (f) are used as the correction factor equation 3.11 for the charged hadron tracks; all of them are shown together in Figure 3.13. Based on overlapping plot of pp and p–Pb, we can see that correction factors are similar for tracks from a pp collision or a p–Pb collision. We conclude that the multiplicity in p–Pb is low enough such that it does not affect tracking performance.

$$w = \frac{1}{\epsilon}(1 - f)b \quad (3.11)$$

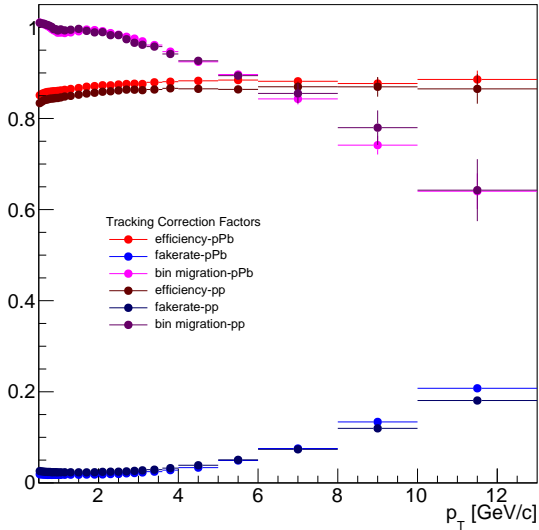


Figure 3.13: The efficiency, fake rate, and momentum smearing correction factors for pp and p–Pb data.

3.3.2.1 Angular dependence of tracking efficiency

The 2D φ - η efficiency is calculated in a similar way to the p_T efficiency described in Equation 3.8, but instead of being functions of p_T^{true} , the efficiency is a function of the true azimuthal angle and pseudorapidity, φ^{true} and η^{true} respectively. Only tracks with $p_T^{\text{true}} > 1$ GeV/ c are considered to avoid tracks with sharp bends in the magnetic field that would obscure the impact of dead regions.

Figure 3.14 shows the resulting efficiency for TPC+ITS and ITS-only tracks. While the TPC+ITS 2D φ - η distribution looks uniform, this is not the case for the ITS-only distribution, which has visible dips in the efficiency at various φ . The efficiency is close to unity for most of the phase space covered. There are no big η variations, but there are large φ variations. The efficiency holes at $\varphi = -0.8$ and -0.2 are very visible and reach values close to zero. These are attributed to ITS-staves that are completely dead. Any variations in φ in the γ^{iso} -hadron analysis are corrected for using the event mixing technique described in Section 3.4.5

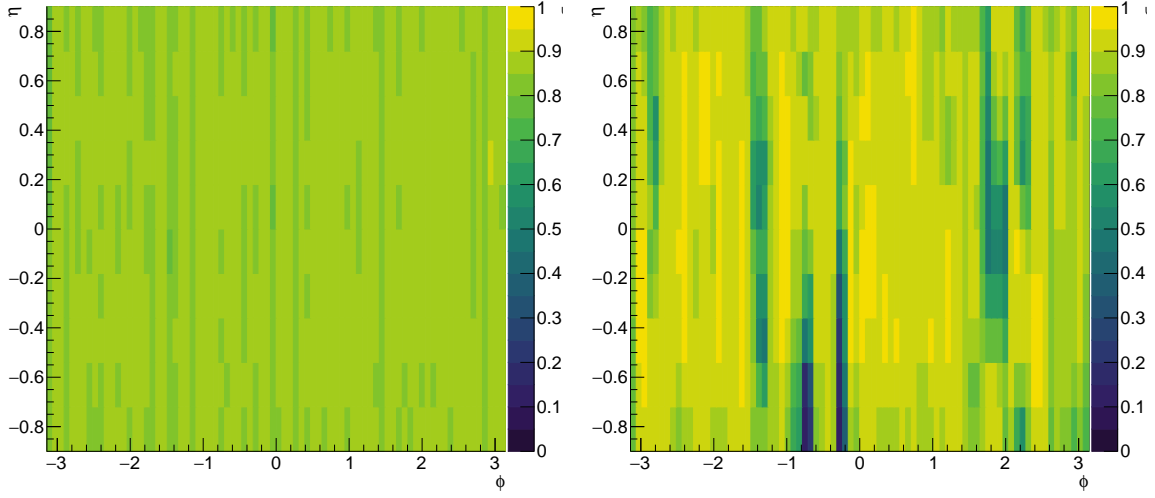


Figure 3.14: Tracking efficiency as a function of φ^{true} and η^{true} for TPC+ITS (left) and ITS-only (right) tracks.

3.4 Photon Hadron Correlations

In this study, the exact cross section of isolated photons is not the observable, nor is the cross section of charged hadron production in a given event. The quantity of interest is the number partner particles associated with those trigger photons, relating to the leading order picture of back-to-back prompt photon and parton. Therefore, instead of quoting the absolute yield of pairs, it is useful to divide by the number of triggers to obtain the conditional yield (also called per-trigger yield) of associated hadrons. This quantity is typically plotted as a function of the azimuthal angle between the trigger and partner particle, $\Delta\phi$:

$$\Delta\phi \equiv \phi^{\text{cluster}} - \phi^{\text{track}} \quad (3.12)$$

The $\Delta\phi$ distribution of cluster-track pairs, divided by the number of triggers is defined as the trigger normalized correlation function, C :

$$C \equiv \frac{P}{T} \quad (3.13)$$

Where T is simply the number of triggers, and P is the $\Delta\phi$ distribution of cluster-track pairs. Such distributions often highlight the structure of jets. They typically contain a large, very narrow peak at $\Delta\phi = 0$, arising from the autocorrelation of the particles within an jet, and a broader peak centered at $\Delta\phi = \pi$ arising from the correlation between two jets in the event.

Enforcing an isolation requirement will heavily suppress the near side peak, however. The near side peak is further removed after the decay photon hadron correlation is subtracted, likely removing the remaining contribution of background jets to the isolated photon triggers ???. This becomes particularly important for the underlying event estimate detailed in ??.

At lowest order in QCD, prompt photons exactly balance the hard scattered parton in the event. For this reason, studies of photon-tagged jets and jet fragments have been dubbed the "golden channel" for studying parton.

3.4.1 Signal Correlation Function

Section 3.1 introduced isolated prompt photons as the primary photon signal for this measurement. However, as detailed in 3.2, there is a substantial amount of background contributing to γ^{iso} candidates and a subsequent contribution to the γ^{iso} -hadron correlations. In this section, we disentangle the signal of this measurement from what is initially measured.

We directly measure the trigger-normalized correlation of shower signal region isolated clusters and associated hadrons, C_{SR} . This quantity will be made up of the true signal correlation function, C_S – the correlation of isolated prompt photons and associated hadrons from the recoiling parton– as well as the true background correlation, C_B , predominantly arising from the correlation between decay photons that pass the cluster selection and hadrons. We call this background the correlated background, as it arises from the correlation of background photons and the hadrons in the event. To separate what is initially measured, C_{SR} , and the true signal, C_S , we begin by taking a look at the ingredients of C_{SR} . First, we denote the number of trigger clusters in the shower signal region, also called the number of γ^{iso} candidates, T_{SR} . We can write T_{SR} as:

$$T_{\text{SR}} = T_S + T_B. \quad (3.14)$$

Here we define T_S as the number of "true" signal triggers (i.e. the number isolated prompt photon triggers) and T_B as the background, most prominently decay photons that pass our γ^{iso} selection. Similarly, the $\Delta\phi$ distribution of signal region cluster-track pairs, P_{SR} can be written as:

$$P_{\text{SR}} = P_S + P_B. \quad (3.15)$$

Now, following the notation of Equation 3.13, we can write the trigger-normalized correlation functions for shower signal region clusters as:

$$C_{\text{SR}} = \frac{1}{T_{\text{SR}}} P_{\text{SR}}. \quad (3.16)$$

These quantities are directly measured. Similarly, we can write the true signal and true background correlation functions:

$$C_S = \frac{1}{T_S} P_S \quad (3.17)$$

$$C_B = \frac{1}{T_B} P_B \quad (3.18)$$

The goal of this formalism is to write the true signal correlation function (C_S) in terms of quantities that are measured – C_{SR} and the measured purity, p . To this end, the next step is to write the measured quantity, C_{SR} , in terms of true signal and true background correlation functions:

$$C_{SR} = \frac{1}{T_{SR}} P_{SR} = \frac{1}{T_{SR}} (P_S + P_B) \quad (3.19)$$

$$C_{SR} = \frac{1}{T_{SR}} (T_S C_S + T_B C_B) \quad (3.20)$$

Where we have substituted equation 3.15 into Equation 3.16, followed by using Equations 3.18 and 3.18 to substitute out P_S and P_B , respectively. T_S and T_B are not directly measured, however they can be expressed in terms of measurable quantities. The purity is defined as the fraction of true signal in our γ^{iso} clusters, or in other words, $p \equiv T_S/T_{SR}$ (see Section 3.2). Substituting this into equation 3.14 and solving for T_B/T_{SR} , one obtains: $T_B/T_{SR} = 1 - p$. This a natural result of the definition of purity: If p is the fraction of the true signal making up the γ^{iso} candidates, $1 - p$ must be everything else, i.e. background. To summarize:

$$p \equiv T_S/T_{SR} \quad (3.21)$$

$$1 - p = T_B/T_{SR} \quad (3.22)$$

Substituting p into Equation 3.20:

$$C_{SR} = p C_S + (1 - p) C_B \quad (3.23)$$

Finally, we can solve for C_S in terms of C_{SR} and p :

$$C_S = \frac{C_{SR} - (1 - p) C_B}{p} \quad (3.24)$$

Equation 3.24 shows C_S in terms of the measured quantities, C_{SR} and the purity. It also includes, however, a term for the background correlation function C_B , that cannot be determined from C_{SR} and the purity alone. The correlation function C_B is described in more detail in section 3.4.2.

3.4.2 Decay Photon Hadron Correlations

There is a large fraction of γ^{decay} background within the isolated photon sample, and a subsequent γ^{decay} -hadron correlation present in the measured correlation function. The correlation between hadrons and background photons within the γ^{iso} sample, most prominently photons from neutral meson decays, correspond to the C_B term in Equation 3.24. While the equation gives us the scale of this background, $1 - p$, it does not offer information on the shape of this $\Delta\phi$ distribution. To understand the shape, we take advantage of the fact that the most prominent source background photons within the γ^{iso} population are photons from neutral meson decays. Outside of the γ^{iso} selection, these photons tend to have more assymmetric shower profiles, and thus larger values of σ_{long}^2 . Therefore, in order to select on clusters arising from decay photons, an inverse shower shape selection is applied which we define as the shower background region, BR:

$$\sigma_{\text{long}}^2(\text{BR}) > 0.4 \quad (3.25)$$

Thus, in order to approximate C_B , a γ^{decay} hadron correlation function is measured by taking the correlation of clusters in the shower background regions with associated hadrons in the event. This shower background region correlation function, much like Eq. 3.16 is defined as C_{BR} :

$$C_{\text{BR}} = \frac{1}{T_{\text{BR}}} P_{\text{BR}}. \quad (3.26)$$

With T_{BR} as the number of clusters in the shower background region, and P_{BR} as the $\Delta\phi$ distribution of shower background region clusters and hadrons.

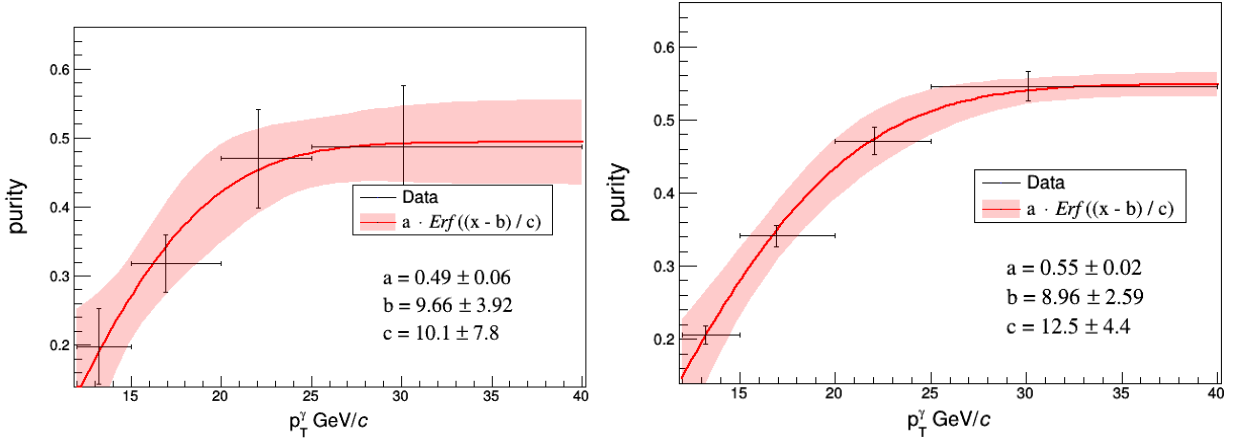
Notably, because the underlying physics process that dictates the number and distribution of correlated pairs is independent of the opening angle of the neutral-meson decay, which is what drives the shower-shape, the approximation $C_{\text{BR}} \approx C_B$ can be made.⁷ In other words, the shower background region correlation function is a good approximation of the correlated background that contributes to the shower signal region correlation function, C_{SR} . Therefore, Eq. 3.24 can be re-written:

$$C_S = \frac{C_{\text{SR}} - (1 - p)C_{\text{BR}}}{p} \quad (3.27)$$

As a result, the true signal correlation function, C_S , is finally written in terms of measurable quantities: The shower signal region correlation function, C_{SR} , the purity, p , and the newly defined shower background region correlation function (or γ^{decay} correlation), C_{BR} .

Thus, hadrons are correlated with clusters in the shower background region to directly measure the γ^{decay} -hadron correlation functions. This γ^{decay} -hadron correlation function is

⁷Here again we take advantage of trigger normalized quantities. The number of isolated photons in the shower background region vastly outnumber the number of isolated photons within the shower signal region. By focusing on the associated yield of hadrons per each photon, which is not correlated with σ_{long}^2 , this very useful approximation can be made.



then subtracted from the the shower signal region correlation function to obtain the signal correlation. This scaling, however, must be done carefully due to the p_T dependance of the purity

3.4.3 Photon Purity Weighting

Equation 3.27 shows the background correlation function, C_B , approximated by the γ^{decay} correlation function, and scaled by $1 - p$ according to its relative contribution measured correlation function. The purity is a p_T -dependent quantity, rising quickly with p_T , correlations using a low- p_T cluster have a higher fraction of background than high- p_T clusters (see Figure ??). As a result, measuring the γ^{decay} -hadron correlation function for all clusters and scaling by the mean of the purity would lead to an underestimation of the background at low p_T^{cluster} , and an overestimation at high p_T^{cluster} . This will have a non-trivial effect on the corresponding z_T bins, which include clusters with a wide range of p_T^{cluster} . Additionally, Equation 3.27 includes an overall scale of $1/p$ in order to obtain the correct conditional yield of hadrons after the subtraction in the numerator, and will yield similar complications if applied correlations using clusters over the full p_T^{cluster} range.

In order to avoid these complications, clusters are weighted by the purity corresponding to their exact p_T^{cluster} when constructing the correlation functions. In order to capture the quickly rising behavior of the purity at low p_T^{cluster} , the purity is fit to a 3-parameter error function. This fit to the purity is shown in Figure 3.4.3. The p_T^{cluster} becomes an input to this function, and precise purity weighting is applied precisely to each cluster.

According to Equation 3.27, the overall purity weights will be $1/p$ and $(1 - p)/p$ for shower signal and shower background region clusters, respectively.

3.4.4 Shower Signal and Background Region Correlations

3.4.5 Pair-Acceptance Correction with Event Mixing

Initially, two particle correlations consist of a combination of true physical correlations and detector effects. The detector effects result from inefficiencies and limited acceptance in the detectors. The study of trigger normalized yields of associated hadrons eliminates the need to correct for isolated cluster efficiency, and Section ?? outlines the charged tracking efficiency correction.

The remaining detector effect on the correlations are pair-acceptance effects: correlations are constructed through pairs of clusters and charged tracks. This results in a convolution of acceptance effects from the limited acceptance of EMCAL and ITS, which we call pair acceptance effects. These effects are corrected for by using the event mixing technique. Event mixing is a data driven approach to correcting for detector acceptance effects⁸. By constructing observables with particles from different events, we remove true physics correlations from the correlation functions, isolating detector effects from limited acceptance in η and detector inhomogeneity in η and φ .

Cluster-track pairs in same event correlation functions obviously share the properties of the event, and such properties often effect detector response. In order to make the mixed-event correlations as analogous as possible to the same-event correlation functions, events that are as similar as possible with respect to these event properties are used for event mixing. The two most important event properties for this measurement are multiplicity and the z-coordinate of the reconstructed primary vertex (i.e. the position of the primary interaction vertex along the beam direction)⁹.

The goal of event mixing is to isolate detector effects by completely removing true physics correlations. To this end, γ -triggered events are not mixed with other γ -triggered events. Triggering on a high p_T photon will result in an enhancement of away-side hadrons due to the recoiling jet. Due to the limited acceptance of the EMCAL, this enhancement will be concentrated in a small area of the ITS, approximately 180° opposite the EMCAL trigger. Mixing only with triggered events will result in a "pseudo" recoiling jet signal that would suppress the true signal in the same-event correlation function when the event mixing correction is applied. Instead, γ -triggered events are mixed with minimum bias events to avoid this bias, and to sample the full acceptance of the ITS properly.

For this analysis, depending on the z_T bin, each γ -triggered event was mixed with up to 300 minimum-bias events.

Traditionally, events are often placed into bins of multiplicity (V0 amplitude, sum of V0A and V0C) and primary vertex z -position, and then mixed within these bins. This has the advantage of conceptual simplicity, but is not very efficient and requires a large amount

⁸Event mixing is also used for estimating combinatorial background.

⁹In Lead-Lead collisions, the event-plane angle which determines the anisotropic distribution of final state particles, or v_2 , is also one of the most important event properties to match in Event mixing. However, because this measurement focuses on smaller systems, pp and p-Pb, this effect can be neglected

of cpu time. Instead of bins, the mixing in this analysis is carried out by using a stable matching algorithm [52]. Generally, this algorithm is used to pair two sets of populations, where members from both populations have a well defined and ordered preference list. Here, the two populations are γ -triggered and minimum bias events. The use of this algorithm avoids the need for binning in multiplicity and primary vertex, and is much faster than the standard binning method.

The stable matching algorithm first creates a preference list made up of all other events based on how close events are in multiplicity and z -vertex. After each event has a preference list, the algorithm loops over all events, with a nested loop that iterates over each event's preference list. The algorithm then pairs the current event to the first unpaired event on that list. As the loop iterates, if an event towards the end of the main loop has an already-paired event high on its preference list, the algorithm loops through the already-paired event's preference list and decides if the paired event should stay paired to its current match, or switch to the new event. If the latter is chosen, the previously matched event is “unpaired” and added back into the loop. A stable state is met when all paired events have a match that is higher on their preference list than any remaining unpaired events in the loop. Such a stable state is guaranteed to eventually be met according to Ref. [52].

The pseudo code below follows this description, using γ to denote a γ -triggered event, and M_B to denote a minimum-bias event. The *unrequested* state refers to a M_B event on a γ -event's preference list that has not yet been requested for pairing.

```

procedure GALESHAPLEYPAIRING
  while  $\exists$  free  $\gamma$  with an unrequested  $M_B$  on  $\gamma$ 's list do
     $M_B$  = first unrequested MinBias Event on  $\gamma$ 's list.
    if  $M_B$  is free then
       $(\gamma, M_B)$  become paired
    else some pair  $(\gamma', M_B)$  exists
      if  $M_B$  prefers  $\gamma$  to  $\gamma'$  then
         $\gamma'$  becomes free
         $(\gamma, M_B)$  become paired
      else
         $(\gamma', M_B)$  remain paired
      end if
    end if
  end while
end procedure
```

The difference distributions for Z-vertex and multiplicity between a γ -triggered and minimum bias events in p–Pb data are shown in Figure 3.15. The resulting distributions show a sharp peak that is below $\Delta z < 0.5$ cm and also a long tail. Less than 6 % of the distribution lies beyond $\Delta z > 2$ cm. The multiplicity difference, however, does not have as sharp a peak

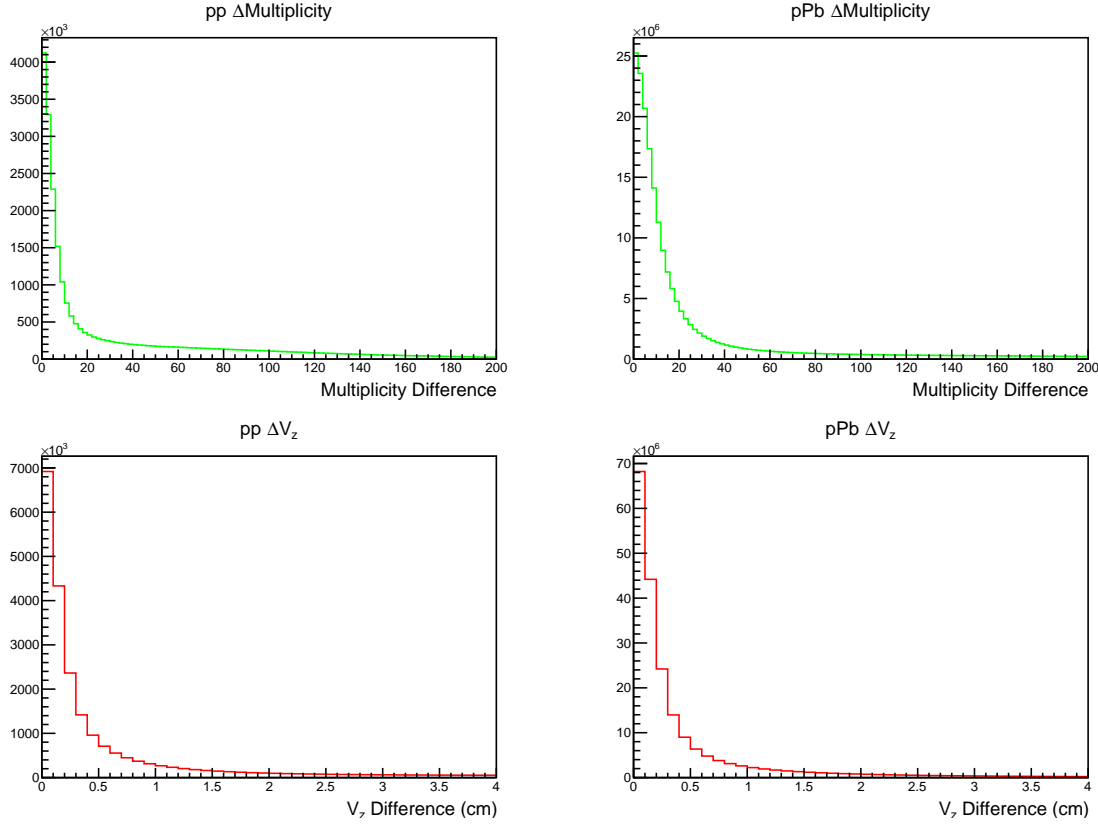


Figure 3.15: Difference in V0 multiplicity (upper row) and longitudinal vertex position (bottom row) between paired events in pp (left column) and p–Pb right. The pairing algorithm results in sharp peak near zero for these difference distributions, particularly in the longitudinal vertex difference. As described in the text, in the correlation analysis we apply a further selection to cut the large tails observed in these distributions.

near Δ Multiplicity = 0. About 20% of pairs have a multiplicity difference above 40, and cuts at $\Delta V_z > 2\text{cm}$ and Δ Multiplicity > 40 were applied to pairs before calculating correlation functions as a precaution. Skimming p–Pb events with particularly high multiplicities before pairing had a similar effect on the tail of the distribution. However, both skimming events before pairing and applying the previously mentioned cuts after the pairing process had no observable effect on the mixed-event correlation.

Figure 3.16 shows the V0 multiplicity distributions for pp and p–Pb data in γ -triggered events. This shows that a multiplicity matching requirement of Δ Multiplicity < 40 is indeed very tight.

Ideally, the mixed event distribution should be flat in $\Delta\varphi$ and have a trapezoidal shape in $\Delta\eta$, because the limited acceptance in η increases the likelihood to reconstruct pairs with

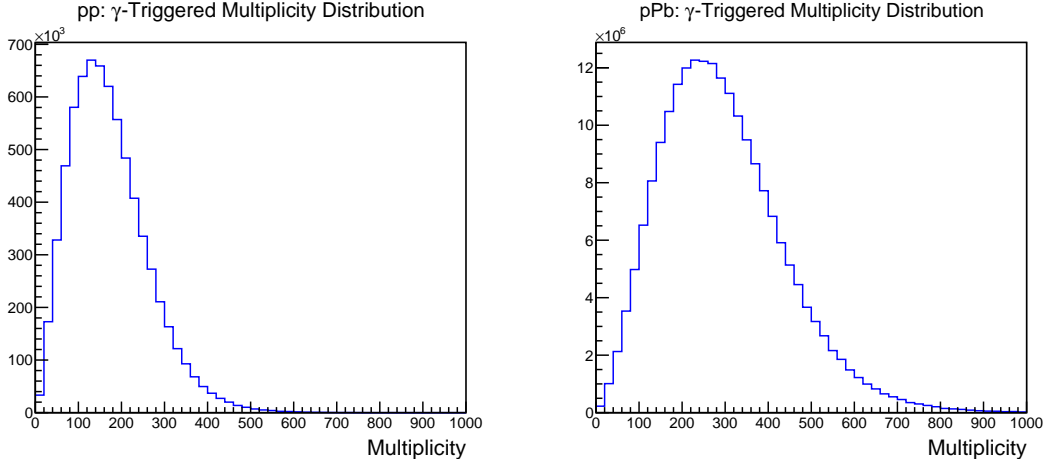


Figure 3.16: V0 multiplicity distribution, i.e. the sum of V0A and V0C amplitudes , in pp (left) and p–Pb (right) gamma-triggered data.

a small $\Delta\eta$ (i.e, due to the convolution of two uniformly distributed functions). However, the use of ITS-only tracks and holes in the ITS acceptance result in deviations from a flat distribution in $\Delta\varphi$.

The correlation function corrected by pair-acceptance effects is then given by:

$$C(\Delta\varphi, \Delta\eta) = \frac{S(\Delta\varphi, \Delta\eta)}{M(\Delta\varphi, \Delta\eta)}, \quad (3.28)$$

where $S(\Delta\varphi, \Delta\eta)$ is the same-event correlation, and $M(\Delta\varphi, \Delta\eta)$ is the mixed-event correlation. $S(\Delta\varphi, \Delta\eta)$ is given by:

$$S(\Delta\varphi, \Delta\eta) = \frac{1}{N_{\text{trig}}} \frac{d^2 N_{\text{same}}}{d\Delta\varphi d\Delta\eta} \quad (3.29)$$

With N_{trig} as the number of trigger particles and N_{same} as the number of same event cluster-track pairs and $d^2 N_{\text{same}}/d\Delta\varphi d\Delta\eta$ is found by pairing trigger particles with tracks from the same event. The mixed-event distribution, $M(\Delta\varphi, \Delta\eta)$, is given by

$$M(\Delta\varphi, \Delta\eta) = \alpha \frac{d^2 N_{\text{mixed}}}{d\Delta\varphi d\Delta\eta}. \quad (3.30)$$

Where α is the normalization constant that sets the maximum value of the mixed event correlation to 1, and N_{mixed} is the number of mixed event cluster-track pairs. The term $d^2 N_{\text{mixed}}/d\Delta\varphi d\Delta\eta$ is obtained by pairing trigger particles from γ -triggered events with tracks from minimum bias events matched in z-vertex and multiplicity.

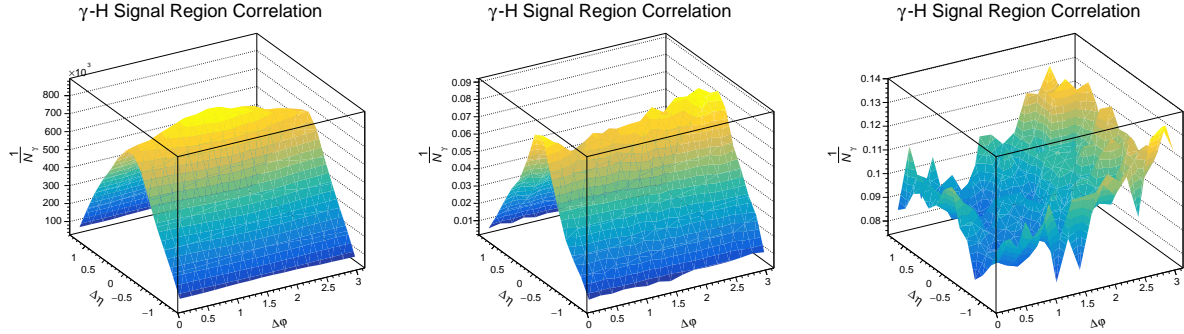


Figure 3.17: **Left** Mixed Event correlation for a single z_T bin for gamma-triggered, signal region clusters and hadrons from minimum bias events. **Middle** 2D Correlation for signal region clusters and hadrons from the same events. **Right** Signal region correlation function corrected for detector acceptance effects.

Same event correlation functions are divided by the mixed event correlation function within the same z_T bins, shown for a single z_T bin in Figure 3.17. This procedure is carried out identically for clusters in the signal and background shower-shape regions.

The triangular shape in $\Delta\eta$ is due to the limited acceptance of the ITS and EMCal in pseudorapidity. A useful analogy is the integration of two intersecting square waves that result in a clear triangular signal. The round shape in $\Delta\phi$ is more subtle, however. It is due to the inefficiencies and holes in the ITS, i.e. due to imperfections in the tracking system. This is further discussed in section 3.4.6.

After the same-event correlation functions

3.4.6 Toy Monte Carlo for Validating Event Mixing

While the ALICE EMCal has a limited acceptance in φ , the ITS has full azimuthal coverage.

Given a perfect detector with limited acceptance, the mixed-event correlations functions is expected to be flat in $\Delta\eta$. This is because the minimum bias tracks in detected by an idealized version of the ITS will have a flat distribution in φ . While the EMCal has a limited acceptance in φ , the $\Delta\phi$ distribution will be flat, as any trigger cluster will be correlated with tracks that are homogeneously spaced in φ ; minimum bias tracks are just as likely to be near a trigger photon as they are to be opposite the trigger photon. This is shown in Figure ?? (A), where trigger photons are constrained in φ and η according to the EMCal acceptance, while track are limited only in eta to correspond to a perfect ITS with full azimuthal coverage.

However, this flat distribution cannot be assumed, as previously seen in Figure 3.17 and now in Figure ?? (A). Dead areas or spots with a lower overall tracking efficiency accumulate over years of use at the LHC, and if large enough effect the mixed event correlations. This is shown in Figure ???. Both track and trigger photon $\Delta\eta$ and $\Delta\phi$ are constrained according

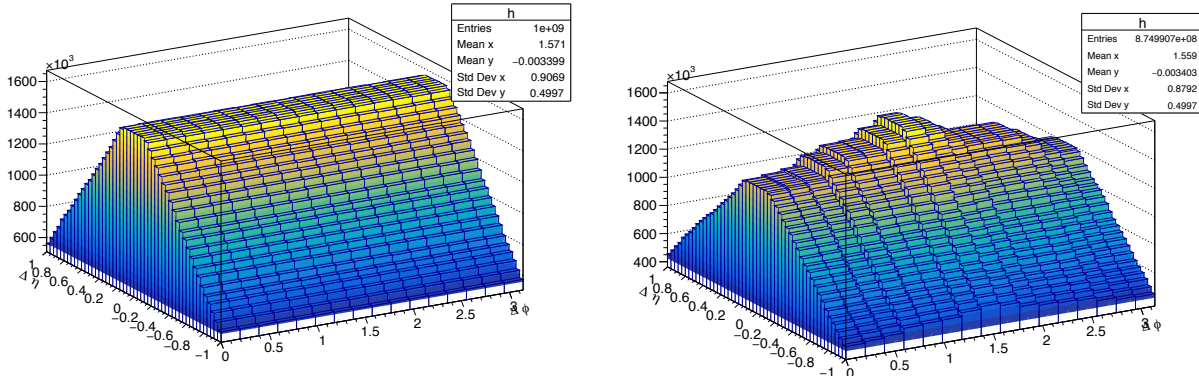


Figure 3.18: Toy MonteCarlo mixed-event correlation function. (A) Photons are produced randomly within X and X in φ , and X and X in η to roughly match the ALICE EMCAL acceptance. Tracks are produced randomly for all values of φ , and X and X in eta to match the acceptance of an ideal ITS. (B) Photons are generate in the same range as (A), however tracks have the additional constrain of excluding the range $X < \varphi < X$ and $X < \varphi < X$.

to their respective detector acceptances, however additional holes in the φ distribution of tracks are placed according to 2D tracking efficiency plot, Figure ?? Section ??.

3.4.7 Underlying Event Estimation

Following gamma-decay correlation subtraction, the final subtraction accounts for the contribution from underlying event. As mentioned in Section 3.1.3, the underlying event corresponds to all the activity in the event that does not directly relate to the hard scattering in the initial collision. In particular, low p_{T} hadrons that are not physically correlated with hadronization of the the scattered parton make up a large portion of the underlying event. For this reason, this background is also called the *the uncorrelated background*. The first step in this measurement, however, is to take the correlation between the trigger photon and all charged hadrons in the event. There is therefore a large contribution to the measured correlation functions from hadrons in underlying event that must be subtracted.

To subtract this underlying event contribution, we use the zero-yield at minimum method. As the name suggests, this method assumes zero true signal at the minimum of the correlation function [include reference that the referee recently asked for]. The distribution of hadrons arising from the underlying event in pp and in p-Pb collisions is conveniently isotropic in φ . Therefore, the distribution of $\Delta\phi$, the angle between the trigger photon and the charged hadrons from the underlying event, will be flat in $\Delta\phi$. As result, the contribution from the underlying event can be estimated as a flat pedestal in $\Delta\phi$.

In dihadron and dijet measurements, the minimum occurs most often around $\Delta\phi = \pi/2$. This is because a struck parton is kinematically unlikely to scatter at roughly 90° from another

Figure 3.19: The bands at low $\Delta\phi$ indicate the region used in the underlying event estimation.

parton in the initial collision. An illustration of this method for *dihadron* measurements is shown in Figure ??.

The isotropic nature of hadrons in the underlying event tells us the shape of the background is a pedestal, while the ZYAM assumption indicates the overall height of the pedestal. Once the shape and magnitude of the underlying event contribution is understood, this background can be subtracted from the correlation functions.

In this analysis, however, we use a modified version of the ZYAM assumption. One of the most prominent features of Figure ?? is a near side peak made up of the autocorrelation of charged hadrons within a jet. The trigger in this analysis, however, are isolated prompt photons that have little to no surrounding hadronic activity. Therefore, the near side jet peak shown in Figure ?? is completely absent in isolated prompt photon-hadron correlations. While some surrounding hadronic activity can still be present, either due to fragmentation photons from a jet that are surrounded by the jet constituents, or by decay photons within a jet, the latter is subtracted away by subtracting the decay-photon hadron correlation.

As a result, the minimum of the γ^{iso} -hadron correlation function spans a much larger region in $\Delta\phi$ than in the dihadron case. We modify the standard ZYAM method by take the average value of the correlation function in the region of $0.4 < \Delta\phi < \pi/2$ to estimate the underlying event pedestal, rather than a much narrower region centered at $\Delta\phi \approx \pi/2$. A minimum $\Delta\phi$ of 0.4 used in order to avoid the region of the isolation cone used in the photon isolation requirement and avoid an artificially low pedestal estimate. The maximum of $\pi/2$ is used to avoid the tail of the away side jet peak.

This larger region in $\Delta\phi$ has the advantage of higher statistical precision in the underlying event estimate. Figure ?? shows the effect of the underlying event subtraction.

After the pedestal subtraction, one can begin to see the similarities between the correlation functions in pp and p-Pb.

3.4.8 Check on UE Estimation

The ZYAM assumption is incredibly useful, as it indicates the overall magnitude of the background arising from the underlying event. It is, however, an assumption that must be checked. To check that the pedestal we estimate using the ZYAM assumption truly corresponds to the amount of uncorrelated background, we cross check it with another background estimation method.

kT smearing is responsible for the away side jet peak being broader than the near side jet peak. This is because in the simple 2-2 scattering picture in which the initial total pT is 0, the two scattered partons should be back-to-back in $\Delta\phi$ to conserve momentum. However, the partons in the initial system do not *necessarily* have 0 pT . Both partons can have an initial transverse momentum, kT , that makes up a component of their overall momentum fraction of the nucleon, Bjorken-x.

This assymetry in the kT of the incomming partons results in a broader gausian in $\Delta\phi$ than the nearside peak. This is because the nearside jet peak arises from the autocorrelation of the particles within a jet, i.e. it is sensitive only to the individual characteristics of a single parent parton and it's fragmentation process. The away side jet peak however, is the result of correlating particles between jets, and is therefore sensitive to the kT asymmetry of the two colliding partons.

The difference in overall momentum fraction in the two partons is responsible for the away-side ridge spanning a very large region in $\Delta\eta$

3.4.9 η Assymetry in p–Pb

3.5 Parton Fragmentation Function

3.5.1 Insensitivty to parton distribution function

1.4 detailed the factorization of the hadronic cross section into the product of the parton distribution function (PDF) and the fragmentation function (FF). A very important question to answer for the study modifications to the fragmentation function in pPb collisions compared to pp collisions is: How do we know if the modifications to the observed γ -tagged associated yields are due to the PDF, and not in fact modifications to the fragmentation function?

To answer this question, the cross prompt photon and hadronic cross sections need to be understood, and the importance of measureng *per-trigger* yields.

[prompt photon cross section]

[hadronic cross section in PbPb] (reference the FF section in the introduction 1.4).

The per trigger yields can thus be interpreted as the ratio of these two cross sections, where the PDF in each formula is the same, and thus cancels. Thus, the answer to the question is: The observable per-trigger hadrons yields is by construction insensitive to the differences between the PDF and nPDF.

3.5.2 p–Pbto pp ratio

3.5.3 Integration Window

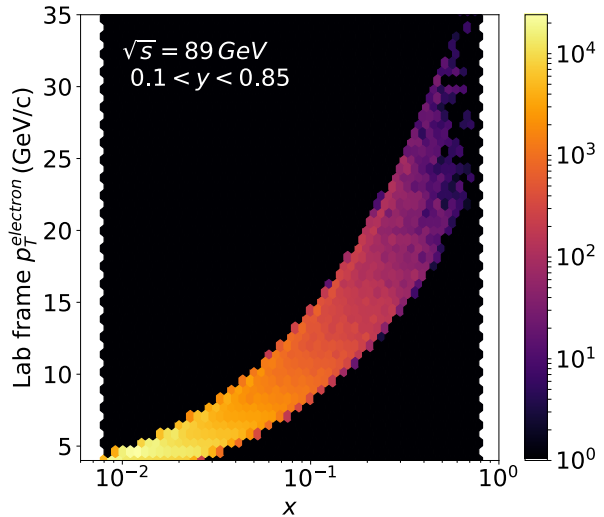
Chapter 4

Cold Nuclear Matter Effects, EIC and LHC

Among the LHC experiments, ALICE is uniquely configured to measure low- p_{T} charged particles. In the context of jet constituents and total jet p_{T} , ALICE is capable of measuring hard scatterings with a lower Q^2 than other LHC experiments. This is of particular interest for studying cold nuclear matter effects, as they are expected to be largest at lower Q^2 . In this work, azimuthal correlations of charged hadrons with isolated photons, γ^{iso} , are presented in p–Pb and pp collisions with a center-of-mass energy of $\sqrt{s_{\text{NN}}} = 5.02 \text{ TeV}$. Isolated photons are measured at midrapidity, $|\eta| < 0.67$, and with transverse momenta in the range $12 < p_{\text{T}} < 40 \text{ GeV}/c$, which yields the scaling variable $x_{\text{T}} = 2p_{\text{T}}/\sqrt{s_{\text{NN}}} = 0.005\text{--}0.016$. This x_{T} range is similar to RHIC measurements at forward rapidity [36].

While lower than other LHC experiments in $v x_{\text{T}}$ and Q^2 , future electron-ion collider experiments are expected to reach Q^2 and Bjorken scaling variable of 0.01 according to Figure ??.

The kinematic range probed in this analysis offers access to a lower Q^2 than other LHC experiments, which is where the largest nuclear effects can be expected, and to a similar x_{T} range as RHIC measurements at forward rapidity [36].



- 4.0.1 Cold nuclear matter measurements at future EIC
- 4.0.2 Transverse Momentum Dependent Distributions
- 4.0.3 Probing \hat{q} at the EIC
- 4.0.4 An All-Silicon Tracker for Jet Measurements at the EIC
- 4.0.5 Charged Jet Fragmentation Function
- 4.0.6 Electron-Jet Correlations

[53]

Chapter 5

Checks and Systematics

A toy montecarlo simulation used to check the shape of the pair acceptance of the EM-Cal+ITS.

5.1 Event Mixing

5.1.1 Binned Event Mixing

5.1.2 Toy Monte Carlo Acceptance Check

5.1.3 Hybrid Tracking Comparison

5.2 Purity

5.2.1 Isolation and Shower shape correlation

5.2.2 EMCAL Acceptance Variation

5.2.3 Purity variation (Last minute IRC check)

5.2.4 Check on Isolation Criterium within EMCAL Acceptance

5.3 Tracking

5.3.1 Comparison to published data

In this section we show the result of the closure test, which is described in Section ??, that aims to validate the MC simulation description of track efficiency, fake rate and momentum smearing corrections using the published data.

Figure 5.1 shows the correction procedure on published data at various stages: the pink line is the published charged-particle spectrum in p–Pb collisions at $\sqrt{s_{\text{NN}}} = 5$ TeV from Ref. [51]; the red line is the published data spectra after multiplying by the efficiency; the orange line is the red spectrum multiplied by the response matrix according to Equation 5.1:

$$R_j = \sum M_{ij} \cdot P_i \quad (5.1)$$

where M is the response matrix, P is the published data times the efficiency, R is smeared p_T spectrum. The smeared p_T spectrum should be consistent with the measured spectrum after removal of the fake-track contribution.

We perform a “folding” of the published spectra instead of an “unfolding” of the measured spectra because the former is a unique transformation and avoids the need for systematic studies on the stability of the unfolding procedure. This allows us to focus on unambiguously testing the response matrix.

The published data has a total uncertainty (quadrature sum of statistical and systematic uncertainties) that ranges from 1.8% at 1 GeV/c, reaches 4.8% by 10 GeV/c and grows quickly to about 20% at 15 GeV/c, where it is dominated by the statistical uncertainty.

Figure 5.2 shows the ratio of the measured fake-subtracted spectrum and the smeared published spectra. The ratio of the published data to the smeared published data is shown to illustrate the impact of the momentum smearing, which is less than a 2% effect for TPC+ITS tracks but it reaches up to a factor of two in the ITS-only case. The closure-test ratios from TPC+ITS tracking are consistent with unity within uncertainties, which is expected. The more interesting result is that the ratios due to ITS-only tracking are within $\pm 5\%$ of unity in the range between 0.85–10 GeV/c and within $\pm 8\%$ of unity in the range between 0.5–0.85 GeV/c, shown by the dashed lines in the bottom plot of Figure 5.2, which is the range we use for our γ^{iso} -hadron analysis. We will be using this difference from unity as our systematic uncertainty on the tracking.

The statistically-significant deviation from the published data with ITS-only tracking at high p_T (blue curve in lower panel of Figure 5.2), could be due to several reasons including improper modeling of a rapid deterioration of the momentum resolution and underestimation of fake rate. Further work would be needed to understand and correct these and other effects at high p_T , but that lies beyond the scope of this work.

We note that these spectra are normalized per-minimum bias event and not by integral, so the fact that the ratios are close to unity reflect the fact that the efficiency calculations shown in Figure 3.10 are an accurate description of the detector response. Based on the results shown in this section, we restrict p_T range to no more than 10 GeV/c, which is beyond the limit of the statistical power of our γ^{iso} -hadron analysis.

5.3.2 Validation of φ -dependence of efficiency

In order to validate the description of the ITS-only tracking holes, we do a test with minimum-bias data. For this, we rely on the fact that apart from the effect of φ -dependent

holes, the track azimuthal angle distribution is expected to be uniform in minimum-bias data. So we measure the track φ spectrum, then correct for the efficiency and check whether the distribution is flat. The level of flatness gives us a sense of the systematic uncertainties associated with mis-modeling of the φ -dependent efficiency.

Figure 5.3 shows the φ -dependence of the tracking efficiency for TPC+ITS and ITS-only tracks. The efficiency is calculated using Equation 3.8, but as a function of φ^{true} instead of p_T^{true} . The TPC+ITS tracking efficiency is flat in φ as expected, but there are dips in the efficiency for the ITS-only tracking due to dead staves in the ITS. These have little impact on the TPC+ITS tracks because the selection does not have the strict requirement on the number of ITS hits, $N_{\text{ITS}} \geq 4$, that is applied for ITS-only tracks.

Figure 5.4 shows the φ distribution of TPC+ITS and ITS-only tracks in minimum-bias p–Pb data and the effect of applying the efficiency correction to the φ distribution. Before applying the efficiency correction, there are visible holes at $\varphi = -1.04, -0.8, -0.2$ rad in ITS-only tracks which are not present in the TPC+ITS tracking. After applying the φ efficiency, the holes are corrected, and we obtain a distribution which is flat within $\pm 2.5\%$. The TPC+ITS remains flat after the efficiency correction, as expected. This shows that the description of dead channels in the ITS is well-described in the simulation.

5.3.3 Hybrid tracking on isolation check

5.4 Summary of Systematic Uncertainties

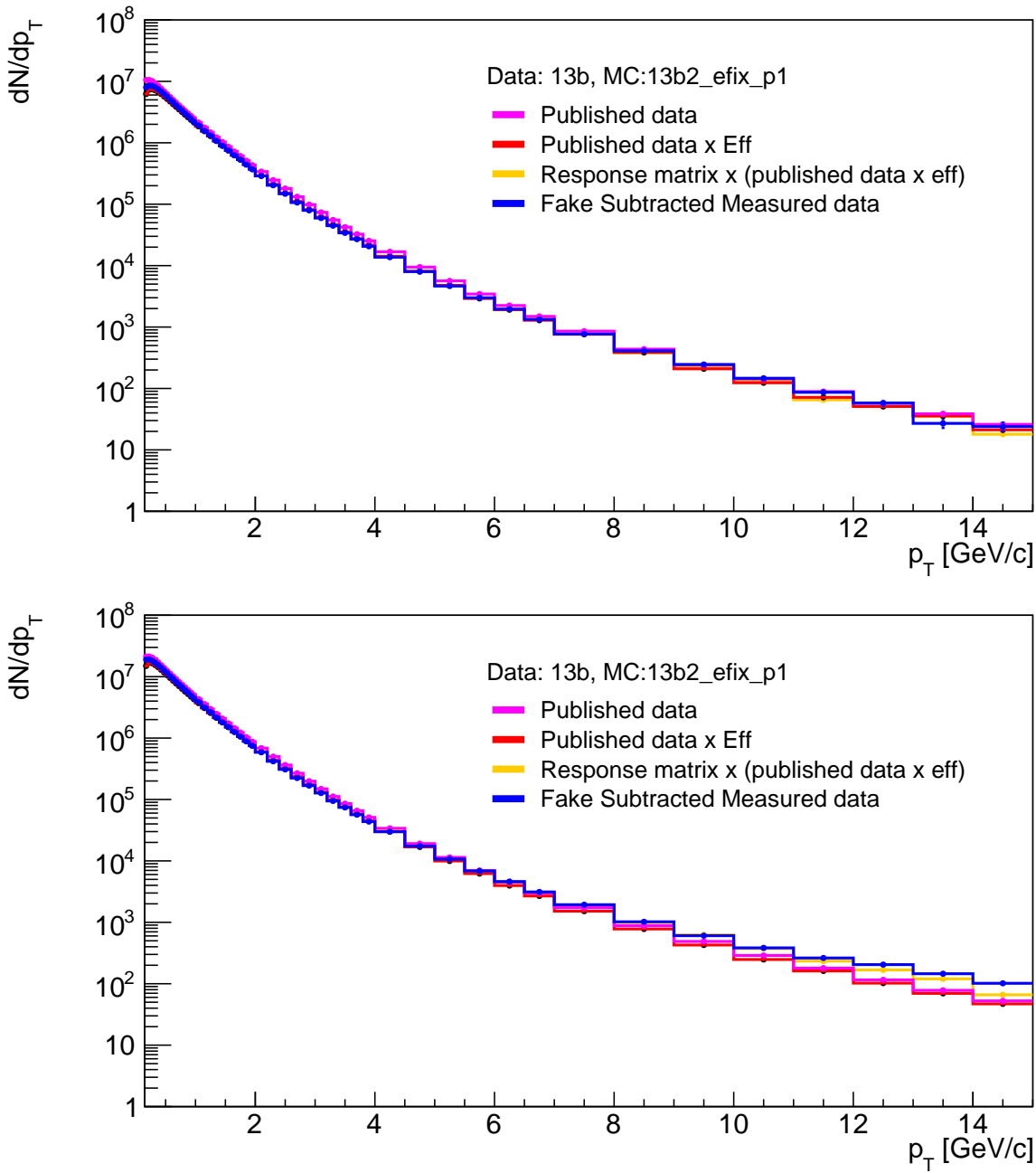


Figure 5.1: Smearing of published data at various stages, using TPC+ITS (top) and ITS only (bottom) response matrices. The pink is the published data p_T spectrum. The red is after the pink has been multiplied by the efficiency. The orange is the spectra after applying the response matrix in order to induce the smearing on the red. The blue is fake-rate-subtracted measured data.

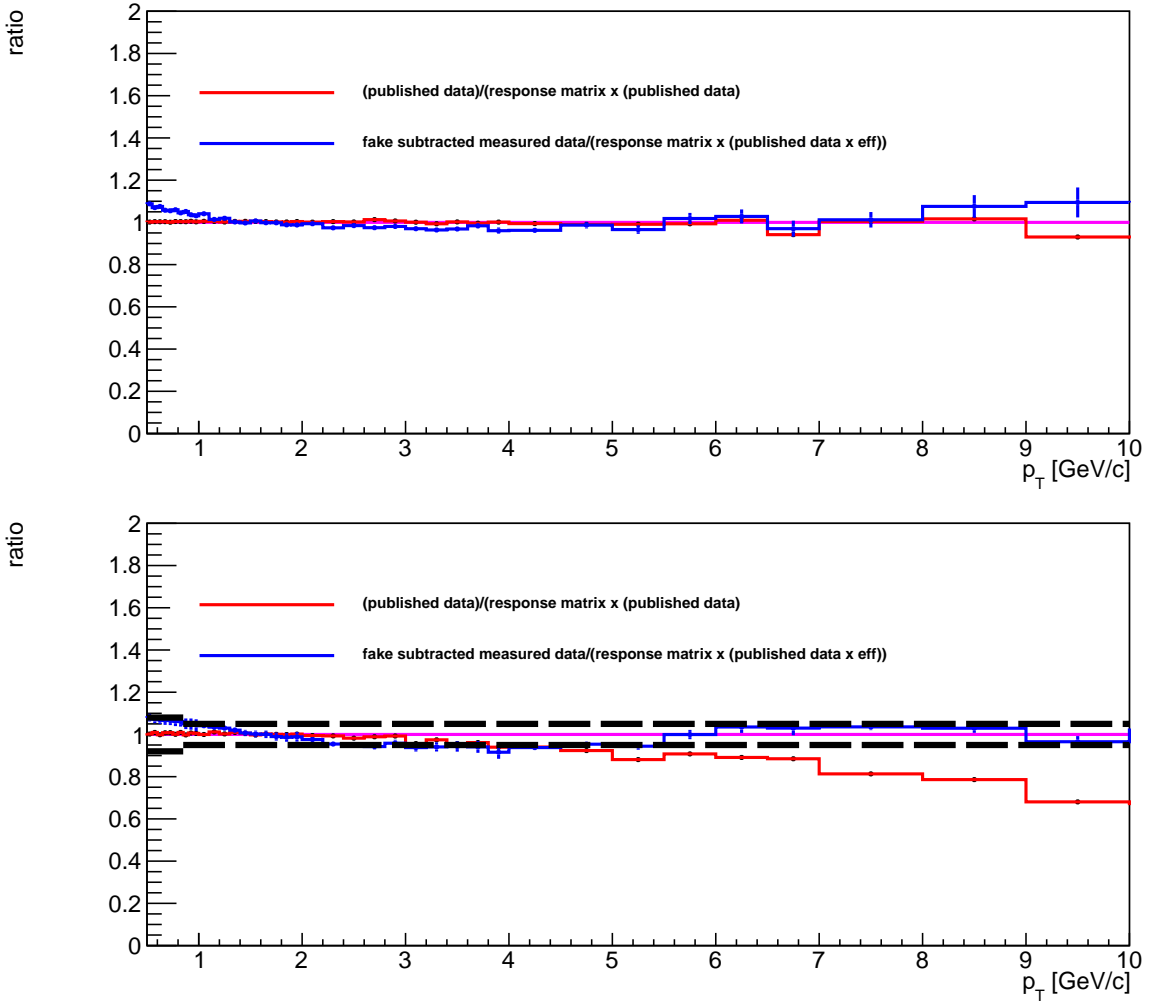


Figure 5.2: Result of closure test comparing measured data and published data, for TPC+ITS tracking (top) and ITS-only tracking (bottom). The red curves show the ratio of the reference spectra to the smeared reference spectra. The blue curves show the ratio of the fake-subtracted measured data and the smeared reference spectra. Ideally the blue curve would be flat at unity. The error bar represents statistical uncertainty only for the blue curve, and the quadrature sum of statistical and systematic uncertainties for the red curve. Additionally, the dashed lines from 0.5 to 0.85 GeV/c represent an 8% band around 1, while the dashed lines from 0.85 to 10.0 GeV/c represent a 5% band around 1.

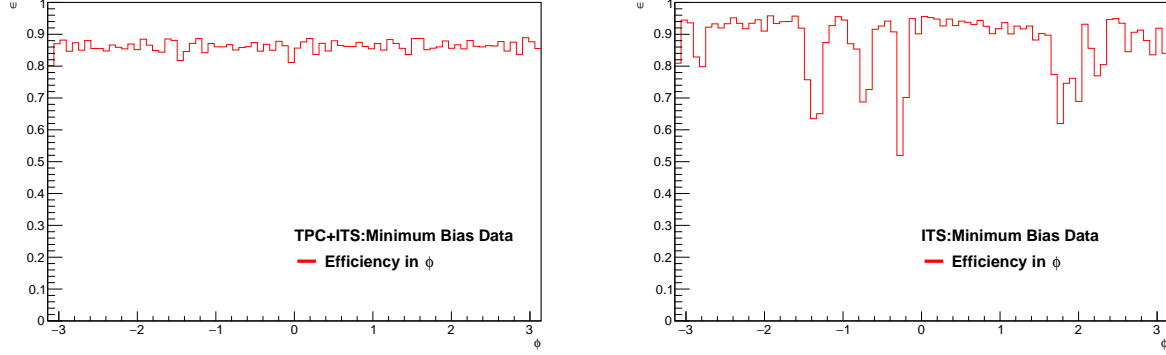


Figure 5.3: Tracking efficiency as a function of ϕ^{true} for TPC+ITS tracks (left) and ITS-only tracks (right). In both cases, the efficiency is calculated for tracks with $p_T^{\text{true}} > 1 \text{ GeV}/c$ using the LHC13b2_efix_p1 Monte Carlo simulation.

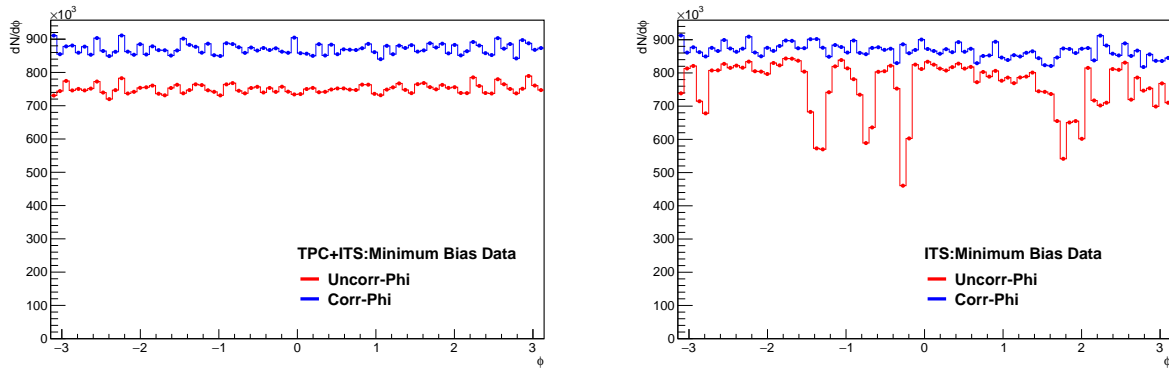


Figure 5.4: Left panel: track ϕ distribution measured in data for tracks with $|\eta| < 0.8$ before (red) and after (blue) applying the efficiency correction for TPC+ITS tracks. Right panel: track ϕ distribution measured in data for tracks with $|\eta| < 0.8$ before (red) and after (blue) applying the efficiency correction for ITS-only tracks.

Appendix A

High Performance Computing for Event Mixing

A.1 Block Implementation and Parallelization

A.2 Hiearchical Data Format 5

Bibliography

- [1] K. Nakamura and. “Review of Particle Physics”. In: *J. Phys. G: Nucl. Part. Phys.* 37 (7A July 2010), p. 075021. ISSN: 0954-3899. DOI: 10.1088/0954-3899/37/7A/075021. URL: <https://doi.org/10.1088/0954-3899/37/7a/075021> (visited on 10/12/2021).
- [2] Alessandro Bettini. *Introduction to Elementary Particle Physics*. Cambridge: Cambridge University Press, 2008. DOI: 10.1017/CBO9780511809019. URL: <https://www.cambridge.org/core/books/introduction-to-elementary-particle-physics/FB7841E74DFEE051D81AD953E81E10DE> (visited on 10/13/2021).
- [3] AIP. *The Interior of the HILAC (Heavy Ion Linear Accelerator), Used in the University of California’s Lawrence Radiation Laboratory Lawrence Berkeley National Laboratory F41*. Feb. 24, 2014. URL: <https://www.aip.org/history-programs/niels-bohr-library/photos/lawrence-berkeley-national-laboratory-f41> (visited on 10/13/2021).
- [4] Kenneth G. Wilson. “Confinement of Quarks”. In: *Phys. Rev. D* 10.8 (Oct. 15, 1974), pp. 2445–2459. DOI: 10.1103/PhysRevD.10.2445. URL: <https://link.aps.org/doi/10.1103/PhysRevD.10.2445> (visited on 10/14/2021).
- [5] Szabolcs Borsányi et al. “Full Result for the QCD Equation of State with 2+1 Flavors”. In: *Physics Letters B* 730 (Mar. 7, 2014), pp. 99–104. ISSN: 0370-2693. DOI: 10.1016/j.physletb.2014.01.007. URL: <https://www.sciencedirect.com/science/article/pii/S0370269314000197> (visited on 10/14/2021).
- [6] HotQCD Collaboration et al. “Equation of State in (\$2+1\$)-Flavor QCD”. In: *Phys. Rev. D* 90.9 (Nov. 4, 2014), p. 094503. DOI: 10.1103/PhysRevD.90.094503. URL: <https://link.aps.org/doi/10.1103/PhysRevD.90.094503> (visited on 10/14/2021).
- [7] C. Aidala et al. “Creation of Quark–Gluon Plasma Droplets with Three Distinct Geometries”. In: *Nat. Phys.* 15.3 (3 Mar. 2019), pp. 214–220. ISSN: 1745-2481. DOI: 10.1038/s41567-018-0360-0. URL: <https://www.nature.com/articles/s41567-018-0360-0> (visited on 10/14/2021).
- [8] K. Aamodt et al. “Higher Harmonic Anisotropic Flow Measurements of Charged Particles in Pb-Pb Collisions at $s_N = 2.76 \text{ TeV}$ ”. In: *Phys. Rev. Lett.* 107.3 (July 11, 2011), p. 032301. ISSN: 0031-9007, 1079-7114. DOI: 10.1103/PhysRevLett.107.032301. URL:

- <https://link.aps.org/doi/10.1103/PhysRevLett.107.032301> (visited on 10/15/2021).
- [9] Paul Romatschke and Ulrike Romatschke. “Viscosity Information from Relativistic Nuclear Collisions: How Perfect Is the Fluid Observed at RHIC?” In: *Phys. Rev. Lett.* 99.17 (Oct. 24, 2007), p. 172301. DOI: 10.1103/PhysRevLett.99.172301. URL: <https://link.aps.org/doi/10.1103/PhysRevLett.99.172301> (visited on 10/14/2021).
 - [10] V. Khachatryan et al. “Observation of Long-Range, near-Side Angular Correlations in Proton-Proton Collisions at the LHC”. In: *J. High Energ. Phys.* 2010.9 (Sept. 27, 2010), p. 91. ISSN: 1029-8479. DOI: 10.1007/JHEP09(2010)091. URL: [https://doi.org/10.1007/JHEP09\(2010\)091](https://doi.org/10.1007/JHEP09(2010)091) (visited on 10/15/2021).
 - [11] Betty Abelev et al. “Long-Range Angular Correlations on the near and Away Side in p-Pb Collisions at sNN=5.02 TeV”. In: *Physics Letters B* 719.1 (Feb. 12, 2013), pp. 29–41. ISSN: 0370-2693. DOI: 10.1016/j.physletb.2013.01.012. URL: <https://www.sciencedirect.com/science/article/pii/S037026931300035X> (visited on 10/15/2021).
 - [12] R. Aaij et al. “Measurements of Long-Range near-Side Angular Correlations in sNN=5 TeV Proton-Lead Collisions in the Forward Region”. In: *Physics Letters B* 762 (Nov. 10, 2016), pp. 473–483. ISSN: 0370-2693. DOI: 10.1016/j.physletb.2016.09.064. URL: <https://www.sciencedirect.com/science/article/pii/S037026931630572X> (visited on 10/15/2021).
 - [13] V. Khachatryan et al. “Evidence for Collectivity in Pp Collisions at the LHC”. In: *Physics Letters B* 765 (Feb. 10, 2017), pp. 193–220. ISSN: 0370-2693. DOI: 10.1016/j.physletb.2016.12.009. URL: <https://www.sciencedirect.com/science/article/pii/S037026931630747X> (visited on 10/15/2021).
 - [14] V. Khachatryan et al. “Long-Range Two-Particle Correlations of Strange Hadrons with Charged Particles in pPb and PbPb Collisions at LHC Energies”. In: *Physics Letters B* 742 (Mar. 6, 2015), pp. 200–224. ISSN: 0370-2693. DOI: 10.1016/j.physletb.2015.01.034. URL: <https://www.sciencedirect.com/science/article/pii/S0370269315000441> (visited on 10/15/2021).
 - [15] Paul Romatschke. “Relativistic Fluid Dynamics Far From Local Equilibrium”. In: *Phys. Rev. Lett.* 120.1 (Jan. 5, 2018), p. 012301. DOI: 10.1103/PhysRevLett.120.012301. URL: <https://link.aps.org/doi/10.1103/PhysRevLett.120.012301> (visited on 10/15/2021).
 - [16] Ryan Atkin. “Review of Jet Reconstruction Algorithms”. In: 645 (Oct. 2015), p. 012008. ISSN: 1742-6596. DOI: 10.1088/1742-6596/645/1/012008. URL: <https://doi.org/10.1088/1742-6596/645/1/012008> (visited on 10/16/2021).

- [17] Michael L. Miller et al. “Glauber Modeling in High-Energy Nuclear Collisions”. In: *Annual Review of Nuclear and Particle Science* 57.1 (2007), pp. 205–243. DOI: 10.1146/annurev.nucl.57.090506.123020. eprint: <https://doi.org/10.1146/annurev.nucl.57.090506.123020>. URL: <https://doi.org/10.1146/annurev.nucl.57.090506.123020>.
- [18] M. Aaboud et al. “Measurement of the Nuclear Modification Factor for Inclusive Jets in Pb+Pb Collisions at sNN=5.02 TeV with the ATLAS Detector”. In: *Physics Letters B* 790 (Mar. 10, 2019), pp. 108–128. ISSN: 0370-2693. DOI: 10.1016/j.physletb.2018.10.076. URL: <https://www.sciencedirect.com/science/article/pii/S037026931830995X> (visited on 10/16/2021).
- [19] Megan Connors et al. “Review of Jet Measurements in Heavy Ion Collisions”. In: *Rev. Mod. Phys.* 90.2 (June 12, 2018), p. 025005. ISSN: 0034-6861, 1539-0756. DOI: 10.1103/RevModPhys.90.025005. arXiv: 1705.01974. URL: <http://arxiv.org/abs/1705.01974> (visited on 10/17/2021).
- [20] Gyula Bencedi. *Nuclear Modification Factor of Charged Particles and Light-Flavour Hadrons in p-Pb Collisions Measured by ALICE*. Sept. 19, 2016. arXiv: 1609.05665 [nucl-ex]. URL: <http://arxiv.org/abs/1609.05665> (visited on 10/17/2021).
- [21] V. Khachatryan et al. “Decomposing Transverse Momentum Balance Contributions for Quenched Jets in PbPb Collisions at $\sqrt{s_{\text{NN}}} = 2.76 \text{ TeV}$ ”. In: *J. High Energ. Phys.* 2016.11 (Nov. 9, 2016), p. 55. ISSN: 1029-8479. DOI: 10.1007/JHEP11(2016)055. URL: [https://doi.org/10.1007/JHEP11\(2016\)055](https://doi.org/10.1007/JHEP11(2016)055) (visited on 10/17/2021).
- [22] D de Florian, San Martin, and D Milstead. “19. Fragmentation Functions in E+e-, Ep and Pp Collisions”. In: (2018), p. 31.
- [23] Jonathan Pumplin et al. “New Generation of Parton Distributions with Uncertainties from Global QCD Analysis”. In: 2002.07 (July 2002), pp. 012–012. ISSN: 1126-6708. DOI: 10.1088/1126-6708/2002/07/012. URL: <https://doi.org/10.1088/1126-6708/2002/07/012> (visited on 10/18/2021).
- [24] J. Adams et al. “Experimental and Theoretical Challenges in the Search for the Quark–Gluon Plasma: The STAR Collaboration’s Critical Assessment of the Evidence from RHIC Collisions”. In: *Nuclear Physics A*. First Three Years of Operation of RHIC 757.1 (Aug. 8, 2005), pp. 102–183. ISSN: 0375-9474. DOI: 10.1016/j.nuclphysa.2005.03.085. URL: <https://www.sciencedirect.com/science/article/pii/S0375947405005294> (visited on 10/19/2021).
- [25] P. Aurenche et al. “Next to Leading Order Bremsstrahlung Contribution to Prompt-Photon Production”. In: *Nuclear Physics B* 399.1 (June 28, 1993), pp. 34–62. ISSN: 0550-3213. DOI: 10.1016/0550-3213(93)90615-V. URL: <https://www.sciencedirect.com/science/article/pii/055032139390615V> (visited on 10/07/2021).

- [26] Gabor David. “Direct Real Photons in Relativistic Heavy Ion Collisions”. In: 83.4 (Mar. 2020), p. 046301. ISSN: 0034-4885. DOI: 10.1088/1361-6633/ab6f57. URL: <https://doi.org/10.1088/1361-6633/ab6f57> (visited on 10/19/2021).
- [27] A. M. Sirunyan et al. “Study of Jet Quenching with Isolated-Photon+jet Correlations in PbPb and Pp Collisions at $s_{\text{NN}}=5.02$ TeV”. In: *Physics Letters B* 785 (Oct. 10, 2018), pp. 14–39. ISSN: 0370-2693. DOI: 10.1016/j.physletb.2018.07.061. URL: <https://www.sciencedirect.com/science/article/pii/S0370269318306245> (visited on 10/20/2021).
- [28] STAR Collaboration et al. “Measurements of Jet Quenching with Semi-Inclusive Hadron+jet Distributions in $\text{Au}+\text{Au}$ Collisions at $\sqrt{s_{\text{NN}}}=200$ GeV”. In: *Phys. Rev. C* 96.2 (Aug. 14, 2017), p. 024905. DOI: 10.1103/PhysRevC.96.024905. URL: <https://link.aps.org/doi/10.1103/PhysRevC.96.024905> (visited on 10/20/2021).
- [29] Hanzhong Zhang et al. “Dihadron Tomography of High-Energy Nuclear Collisions in Next-to-Leading Order Perturbative QCD”. In: *Phys. Rev. Lett.* 98.21 (May 25, 2007), p. 212301. DOI: 10.1103/PhysRevLett.98.212301. URL: <https://link.aps.org/doi/10.1103/PhysRevLett.98.212301> (visited on 10/20/2021).
- [30] PHENIX Collaboration et al. “Measurement of Jet-Medium Interactions via Direct Photon-Hadron Correlations in $\text{Au}+\text{Au}$ and $d+\text{Au}$ Collisions at $\sqrt{s_{\text{NN}}}=200$ GeV”. In: *Phys. Rev. C* 102.5 (Nov. 19, 2020), p. 054910. DOI: 10.1103/PhysRevC.102.054910. URL: <https://link.aps.org/doi/10.1103/PhysRevC.102.054910> (visited on 10/20/2021).
- [31] J. Pumplin et al. “Uncertainties of Predictions from Parton Distribution Functions. II. The Hessian Method”. In: *Phys. Rev. D* 65.1 (Dec. 12, 2001), p. 014013. DOI: 10.1103/PhysRevD.65.014013. URL: <https://link.aps.org/doi/10.1103/PhysRevD.65.014013> (visited on 10/21/2021).
- [32] J. W. Cronin et al. “Production of Hadrons at Large Transverse Momentum at 200, 300, and 400 GeV”. In: *Phys. Rev. D* 11.11 (June 1, 1975), pp. 3105–3123. DOI: 10.1103/PhysRevD.11.3105. URL: <https://link.aps.org/doi/10.1103/PhysRevD.11.3105> (visited on 10/21/2021).
- [33] “Jet Structure from Dihadron Correlations in D+Au Collisions at S_{NN} 200-GeV”. In: *Phys. Rev. C* 73 (2006), p. 054903. DOI: 10.1103/PhysRevC.73.054903. arXiv: nucl-ex/0510021.
- [34] Shreyasi Acharya et al. “Jet Fragmentation Transverse Momentum Measurements from Di-Hadron Correlations in $s = 7$ TeV Pp and $S_{\text{NN}} = 5.02$ TeV p-Pb Collisions”. In: *JHEP* 03.CERN-EP-2018-303 (2019), p. 169. DOI: 10.1007/JHEP03(2019)169. arXiv: 1811.09742 [nucl-ex].

- [35] Jaroslav Adam et al. “Measurement of Dijet K_T in p–Pb Collisions at $S_{NN}=5.02$ TeV”. In: *Phys. Lett.* B746.CERN-PH-EP-2015-041 (2015), pp. 385–395. DOI: 10.1016/j.physletb.2015.05.033. arXiv: 1503.03050 [nucl-ex].
- [36] A. Adare et al. “Suppression of Back-to-Back Hadron Pairs at Forward Rapidity in d+Au Collisions at $S_{NN}=200$ GeV”. In: *Phys. Rev. Lett.* 107 (2011), p. 172301. DOI: 10.1103/PhysRevLett.107.172301. arXiv: 1105.5112 [nucl-ex].
- [37] C. Aidala et al. “Nonperturbative Transverse Momentum Broadening in Dihadron Angular Correlations in $S_{NN}=200$ GeV Proton-Nucleus Collisions”. In: *Phys. Rev.* C99.4 (2019), p. 044912. DOI: 10.1103/PhysRevC.99.044912. arXiv: 1809.09045 [hep-ex].
- [38] Morad Aaboud et al. “Measurement of Jet Fragmentation in 5.02 TeV Proton-Lead and Proton-Proton Collisions with the ATLAS Detector”. In: *Nucl. Phys.* A978.CERN-EP-2017-065 (2018), p. 65. DOI: 10.1016/j.nuclphysa.2018.07.006. arXiv: 1706.02859 [hep-ex].
- [39] Daniel de Florian et al. “Global Analysis of Nuclear Parton Distributions”. In: *Phys. Rev.* D85 (2012), p. 074028. DOI: 10.1103/PhysRevD.85.074028. arXiv: 1112.6324 [hep-ph].
- [40] A. Accardi et al. “Parton Propagation and Fragmentation in QCD Matter”. In: *Riv. Nuovo Cim.* 32.JLAB-THY-09-1038 (2010), pp. 439–553. DOI: 10.1393/ncr/i2009-10048-0. arXiv: 0907.3534 [nucl-th].
- [41] A. Accardi et al. “Electron Ion Collider: The next QCD Frontier”. In: *Eur. Phys. J.* A52.BNL-98815-2012-JA, JLAB-PHY-12-1652 (9 2016). Ed. by A. Deshpande, Z. E. Meziani, and J. W. Qiu, p. 268. DOI: 10.1140/epja/i2016-16268-9. arXiv: 1212.1701 [nucl-ex].
- [42] Hongxi Xing et al. “Transverse Momentum Imbalance of Back-to-Back Particle Production in P+A and E+A Collisions”. In: *Phys. Rev. D* 86 (2012), p. 094010. DOI: 10.1103/PhysRevD.86.094010. arXiv: 1206.1826 [hep-ph].
- [43] Megan Connors et al. “Jet Measurements in Heavy Ion Physics”. In: *Rev. Mod. Phys.* 90 (2018), p. 025005. DOI: 10.1103/RevModPhys.90.025005. arXiv: 1705.01974 [nucl-ex].
- [44] C. A. Salgado et al. “Proton-Nucleus Collisions at the LHC: Scientific Opportunities and Requirements”. In: *J. Phys.* G39.CERN-PH-TH-2011-119, LHC-PROJECT-REPORT-1181, FERMILAB-PUB-11-841-T (2012), p. 015010. DOI: 10.1088/0954-3899/39/1/015010. arXiv: 1105.3919 [hep-ph].
- [45] Bezverkhny Abelev et al. “Performance of the ALICE Experiment at the CERN LHC”. In: *Int. J. Mod. Phys.* A29.CERN-PH-EP-2014-031 (2014), p. 1430044. DOI: 10.1142/S0217751X14300440. arXiv: 1402.4476 [nucl-ex].

- [46] Shreyasi Acharya et al. “Direct Photon Production at Low Transverse Momentum in Proton-Proton Collisions at s=2.76 and 8 TeV”. In: *Phys. Rev.* C99.CERN-EP-2018-045 (2 2019), p. 024912. DOI: 10.1103/PhysRevC.99.024912. arXiv: 1803.09857 [nucl-ex].
- [47] Raphaëlle Ichou and David d’Enterria. “Sensitivity of Isolated Photon Production at TeV Hadron Colliders to the Gluon Distribution in the Proton”. In: *Phys. Rev. D* 82.1 (July 2010), p. 014015. DOI: 10.1103/PhysRevD.82.014015. URL: <https://link.aps.org/doi/10.1103/PhysRevD.82.014015>.
- [48] Matteo Cacciari, Gavin P. Salam, and Sebastian Sapeta. “On the Characterisation of the Underlying Event”. In: *JHEP* 04 (2010), p. 065. DOI: 10.1007/JHEP04(2010)065. arXiv: 0912.4926 [hep-ph].
- [49] CMS Collaboration. “Study of jet quenching with isolated-photon+jet correlations in PbPb and pp collisions at $\sqrt{s_{\text{NN}}} = 5.02$ TeV”. In: *arXiv:1711.09738* (2017). arXiv: 1711.09738 [nucl-ex].
- [50] F. James and M. Roos. “Minuit: A System for Function Minimization and Analysis of the Parameter Errors and Correlations”. In: *Comput. Phys. Commun.* 10 (1975), pp. 343–367. DOI: 10.1016/0010-4655(75)90039-9.
- [51] S. Acharya et al. “Transverse Momentum Spectra and Nuclear Modification Factors of Charged Particles in Pp, p-Pb and Pb-Pb Collisions at the LHC”. In: *JHEP* 11.CERN-EP-2018-025 (2018), p. 013. DOI: 10.1007/JHEP11(2018)013. arXiv: 1802.09145 [nucl-ex].
- [52] D. Gale and L. S. Shapley. “College Admissions and the Stability of Marriage”. In: *The American Mathematical Monthly* 69.1 (1962;), pp. 9–15.
- [53] A. Fantoni et al. “The ALICE Electromagnetic Calorimeter: EMCAL”. In: *Journal of Physics: Conference Series* 293 (Apr. 2011), p. 012043. DOI: 10.1088/1742-6596/293/1/012043. URL: <https://doi.org/10.1088%5C2F1742-6596%5C2F293%5C2F1%5C2F012043>.